POLARIZED ^{3}He$(e, e'n)$ ASYMMETRIES IN THREE ORTHOGONAL MEASUREMENTS

A dissertation submitted

to Kent State University in partial

fulfillment of the requirements for the

degree of Doctor of Philosophy

by

Elena Amanda Long

August, 2012

Abstract

Elena Amanda Long, Ph.D., August, 2012 Physics

POLARIZED ^{3}He$(e, e'n)$ ASYMMETRIES IN THREE ORTHOGONAL MEASUREMENTS

Directors of Dissertation: Bryon D. Anderson and Douglas W. Higinbotham

Asymmetry measurements have been conducted in Jefferson Lab's Hall A through electron scattering from a vertically polarized ^{3}He target in the quasi-elastic $^3\mathrm{He}^{\uparrow}(e, e'n)$ reaction. Measurements were made with the target polarized in the longitudinal direction with respect to the incoming electrons, in a transverse direction that was orthogonal to the beam-line and parallel to the q-vector, and in a vertical direction that was orthogonal to both the beam-line and the q-vector. The experiment measured these asymmetries at four-momentum transfer (Q^2) of 0.1 (GeV/c)^2, 0.5 (GeV/c)^2 and 1.0 (GeV/c)^2. This is the first time that three orthogonal asymmetries have been measured in the same experiment. Results from this experiment will be useful in testing models used to extract neutron form factors from polarized ^{3}He. In the transversely polarized target case, an extraction of the electric form factor of the neutron can be made.

Dissertation written by

Elena Amanda Long

B.S., Juniata College, 2006

M.A., Kent State University, 2008

Ph.D., Kent State University, 2012

Approved (hopefully) by

Dr. Bryon D. Anderson,	Co-chair, Doctoral Dissertation Committee
Dr. Douglas W. Higinbotham,	Co-chair, Doctoral Dissertation Committee
Dr. D. Mark Manley,	Member, Doctoral Dissertation Committee
Dr. Peter C. Tandy,	Member, Doctoral Dissertation Committee
Dr. Diane Stroup,	Member, Doctoral Dissertation Committee

Accepted by

Dr. James T. Gleeson,	Chair, Department of Physics
Dr. Timothy Moerland,	Dean, College of Arts and Sciences

Table of Contents

List of Figures

List of Tables

Acknowledgement

Need to add acknowledgements here...

Date Completed.

Chapter 1

Introduction

Atoms, which constitute most of normal matter, are made of electrons (e) and a nucleus. Particles that make up the nucleus are called nucleons (N) which can be of two types: protons (p) and neutrons (n). The nucleons themselves are made of smaller particles called quarks that are held together by the exchange of particles of the strong nuclear force, called gluons. Nucleons are primarily comprised of two different flavors of quarks called up and down. In the simplified constituent quark model the proton is made of two up quarks and one down quark and the neutron is composed of one up and two down quarks.

Interactions between these particles are used to study the internal structure of nucleons. For example, consider that ^{3}He nuclei, which are comprised of two protons and one neutron, are struck by a beam of electrons. If the incoming electron interacts with the ^{3}He nucleus with low energy and momentum transferred (usually by the exchange of single virtual photon, γ) such that the nucleus remains intact and in its ground state (lowest energy state) after the interaction, this is called elastic scattering. In another case, the electron may interact with the ^{3}He nucleus with higher energy and momentum transferred and a single nucleon is knocked free from the nucleus, but the nucleon remains intact and in its ground state. This is called quasi-elastic scattering. At even higher energy and momentum transferred, the electron can interact directly with a single quark which can either break the nucleon apart or leave it in an excited state. This is called deep inelastic scattering.

A shorthand notation is often used to describe the interaction channel that is measured. For example, assume that an electron beam is incident upon a ^{3}He nucleus and knocks out a neutron that is detected. The notation for this would be $^3\mathrm{He}(e, e'n)$ where ^{3}He represents the target, e represents the incoming electron, e' represents the scattered electron and n represents the scattered neutron.

One of the observables that is well suited to extracting structure information of nucleons is spin asymmetry. Each of the particles mentioned carry a quantum property called spin, which is mathematically similar to classical rotational angular momentum but with quantized properties and can be in one of two states called spin up and spin down. The direction of the spin can be controlled and measured through the use of magnetic fields. An asymmetry measurement is useful in determining if a single spin state dominates another one. A simplified example would be

$$A = \frac{N_\uparrow - N_\downarrow}{N_\uparrow + N_\downarrow}, \tag{1.1}$$

where $N_\uparrow$ is the number of detected particles with spin up, $N_\downarrow$ is the number of detected particles with spin down, and A is the asymmetry. A similar asymmetry can be made with helicity, which is simply the projection of the spin ($\vec{S}$) onto the direction of momentum ($\vec{p}$) and is written as

$$h = \vec{S} \cdot \vec{p}. \tag{1.2}$$

Electron scattering is a well understood process that is useful for probing the internal structure of nucleons. Thomas Jefferson National Accelerator Facility (Jefferson Lab) is a prime location to conduct these experiments due to its ability to produce a highly polarized continuous-wave electron beam. Experimental Hall A

at Jefferson Lab is particularly suited to perform asymmetry measurements due to its polarized ^{3}He target and high resolution spectrometers.

This dissertation is organized into six chapters. Chapter 1 discusses the theoretical motivation for the measurements taken as well as placing them within an historical context. Chapter 2 provides an overview of the theoretical calculations used that are being tested. Chapter 3 describes the equipment used throughout the experiment. This includes both information about the electron beam and the equipment within Jefferson Lab's Experiment Hall A. The methods used for particle identification are described in Chapter 4. Factors adjusting the asymmetry measurement, such as dilutions, as well as the error analysis methods used are discussed in Chapter 5. Finally, results from the measurements are presented in Chapter 6.

1.1 Motivation

Measures of nucleon form factors are not direct observables and thus must be extracted from observables through the use of theoretical models. Assumptions made in producing the models can have a large effect on the extraction. For example, there was a discrepancy between extractions of the electric form factor of neutron, G_E^n, obtained from deuterium scattering and those from ^{3}He as seen in Figure 1.1.

The original models were based on the plane wave impulse approximation (PWIA) to extract the form factors from cross section asymmetries. At low momentum transfer, the simple PWIA is known not to accurately describe experimental results due to the effects of meson exchange currents (MEC) and final-state interactions (FSI). Meson exchange currents are due to the fact that the nucleons in the ^{3}He nucleus are interacting by meson exchange. Thus, apart from the quasi-free scattering amplitude, there will be contributions from direct coupling to the electro-

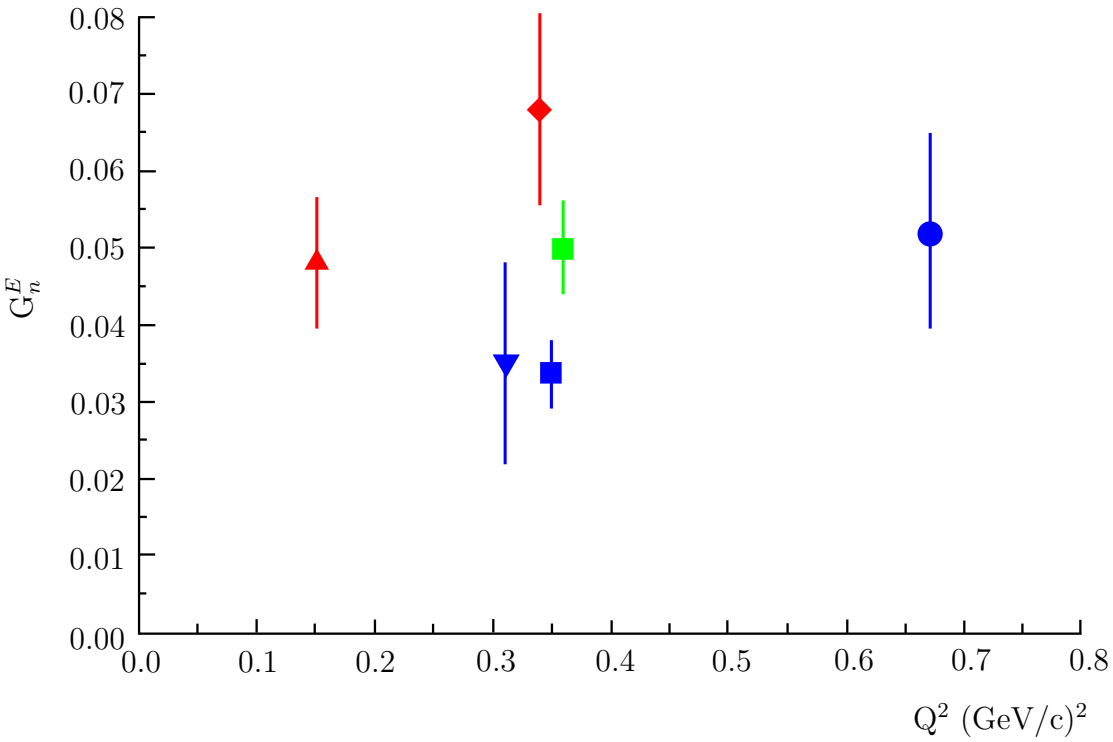

Fig. 1.1: Discrepancy between double-polarized ^{3}He and ^{2}H G_n^E Extractions using PWIA and small contributions from FSI and MEC. The red ▲[1] and ♦[2] correspond to extractions from deuterium where the blue ▼[3], ■[4], and •[5] correspond to extractions from ^{3}He using PWIA models with small contributions from FSI and MEC. The green ■[6] corresponds to ^{3}He data using models that account for large FSI.

magnetic currents of exchanged mesons. Final-state interactions may be important since the final state is a system of three interacting nucleons rather than just two plane waves. To the leading order, FSI can be considered as rescattering of the struck nucleon (the neutron here) by the residual nucleus.

In the PWIA, a single spin asymmetry transverse to the scattering plane is calculated to be exactly zero. Early predictions expected contributions from final state interactions (FSI) and mesonic exchange currents (MEC) to be small above a momentum transfer squared (Q^2) of 0.2 $(GeV/c)^2$, as can be seen by Laget's original calculation[7] in Figure 1.2. In the same figure, there is a data point from an experiment that was done at the Nationaal Instituut voor Kernfysica en Hoge-Energiefysica (NIKHEF) which showed this asymmetry to be larger than expected. The Bochum theoretical group, which correctly predicted the observed asymmetry used full Fadeev calculations that correctly estimated the significant effects of FSI and MEC. Extractions of the electric form factor of the neutron now had to take these into account, which led to a re-analysis of the data in Figure 1.1 and largely removed the discrepancy between ^{2}H and ^{3}He data as can be seen by the green ■.

A target single-spin asymmetry has not previously been measured at higher Q^2, leaving contributions from FSI and MEC in this region largely unknown. The current experiment measured this spin asymmetry (A_y) at Q^2=0.1, 0.5, and 1.0 $(GeV/c)^2$.

Extractions of the electric form factor of the neutron can be made from a double-spin asymmetry where the beam is polarized transverse to the target and the target is polarized in the direction of the q-vector. The current experiment also measured this transverse asymmetry (A_z) at Q^2=0.1, 0.5, and 1.0 $(GeV/c)^2$.

^{3}He$(e, e'n)$ asymmetry measurements in three orthogonal directions have never been done before in all three directions. The current experiment is the first to also

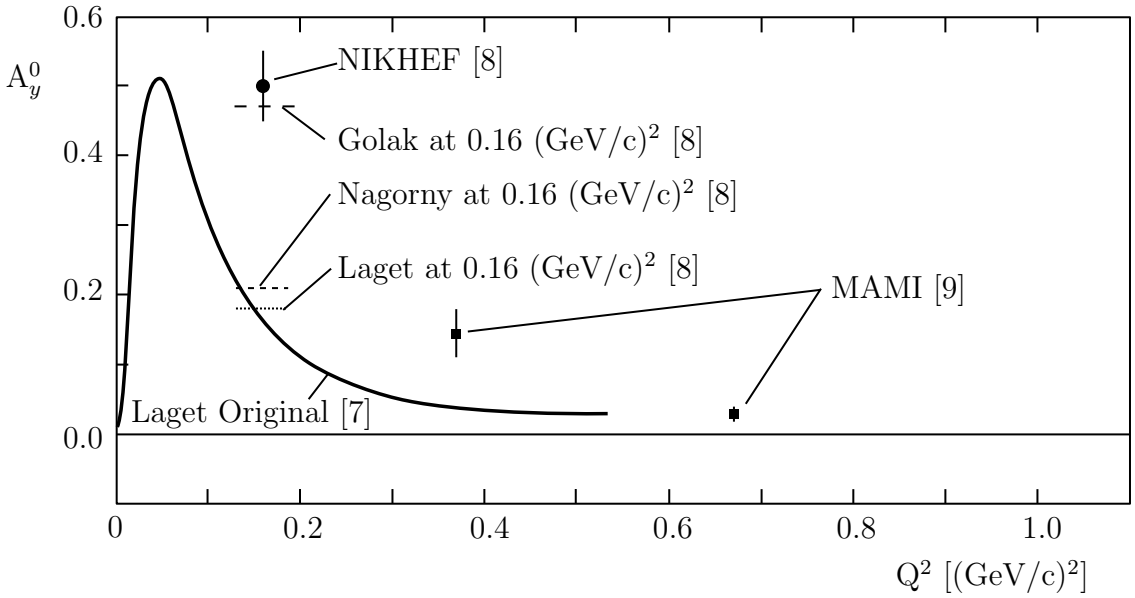

Fig. 1.2: Previous A_y^0 Asymmetry Measurements. Vertical single-spin asymmetry measurements from NIKHEF at Q^2=0.16^2 (GeV/c), MAMI at Q^2=0.37 and 0.67 (GeV/c)^2, and various theoretical models are plotted. The Bochum group used Fadeev calculations to calculate the FSI whereas the others are modified PWIA. PWIA predicts this asymmetry to be exactly zero.

measure the longitudinal helicity asymmetry (A_x) at Q^2=0.1, 0.5, and 1.0 (GeV/c)^2. These measurements provide significantly improved tests of the various theoretical predictions.

1.2 Experiment Overview

The present experiments were performed at the Thomas Jefferson National Accelerator Facility in Newport News, Virginia in experimental Hall A. The experiments, E05-015, E05-102, and E08-005, were conducted to learn about the polarized ^{3}He states as well as interactions that occur in electron scattering on ^{3}He. A ^{3}He target was used that could be polarized in three orthogonal directions. The first, defined as longitudinal, was parallel to the incident electron beam. The second, defined as vertical, was orthogonal to both the incident electron beam as well as the

neutron q-vector. The third, defined as transverse, was orthogonal to the incident electron beam and parallel to the neutron q-vector. Each of these is indicated in Figure 1.3

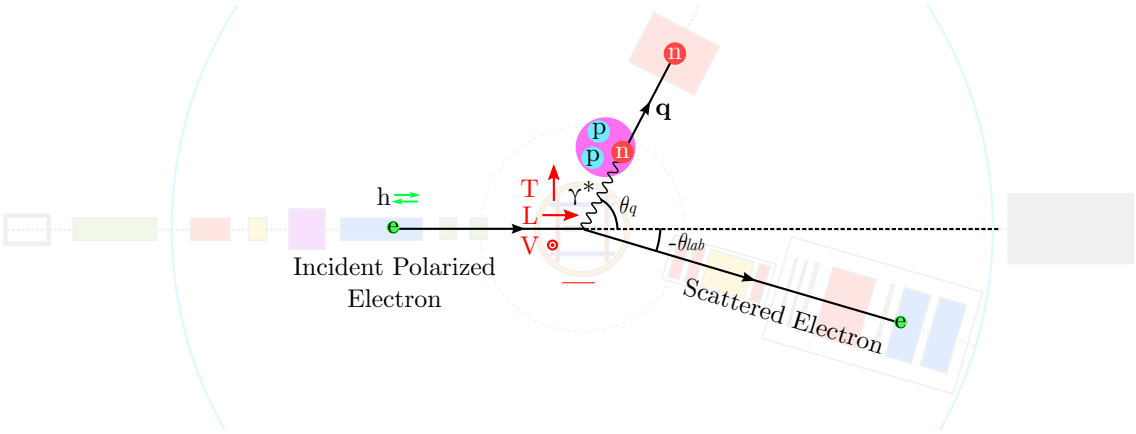

Fig. 1.3: Definition of Polarization Directions. Vertical target polarization (V) was used to measure A_y, transverse target polarization (T) was used to measure A_z, and longitudinal target polarization (L) was used to measure A_x.

The incoming electron beam had a polarization of approximately 80%. This beam, at energies of 1.2, 2.4, and 3.6 GeV, was incident on a 40 cm long ^{3}He cell that is capable of being polarized up to 60% in the vertical, longitudinal, or transverse directions. The scattered electrons were detected in a high resolution spectrometer (HRS) that consists of three focusing quadrupole magnets, one bending dipole magnet, and a series of scintillators, wire chambers, and gas Cerenkov detectors used for particle identification. The knocked out neutrons were detected by the Hall A neutron detector (HAND) which consists of a matrix of 88 plastic scintillator bars that are each 10 cm thick arranged in four layers with a veto layer in front that consists of 64 2-cm thick scintillator bars. HAND has a total thickness of 40 cm.

A coincidence measurement between the HRS and HAND that correlates the scattered electrons with the knocked-out neutrons was performed. The target had repeated spin-flips throughout the experiment where the polarization of the ^{3}He

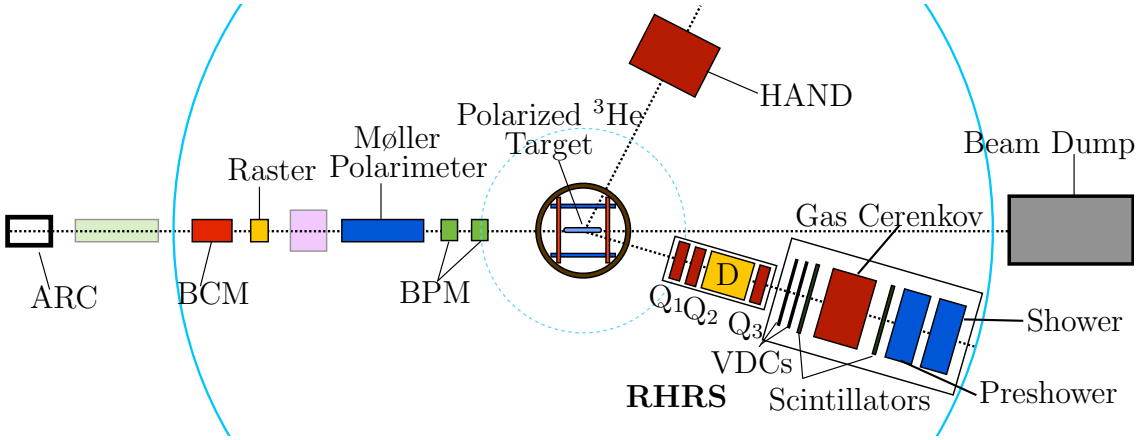

Fig. 1.4: Hall A Equipment used for ^{3}He$(e, e'n)$ Measurements

is rotated by 180°, giving 'up' and 'down' states in the vertical, longitudinal, and transverse directions. The scattering asymmetry was measured with the target polarized in each of these three directions. Of particular importance is the vertical and transverse asymmetries. The measurement of the vertical single-spin asymmetry provides new constraints on models of G_n^E, as discussed in Section 1.1, while a measurement of the transverse double-spin asymmetry allows an extraction of G_n^E to be made.

Chapter 2

Theory

2.1 ^{3}He Ground State

The experimental study of proton structure is relatively straight-forward due to readily available free proton targets. This is not the case for studying the internal structure of the neutron since no free neutron target is available. As such, low-A targets where the nucleons are weakly bound are often used to approximate a free neutron target. This is most often done using ^{2}D or ^{3}He. Deuterons are advantageous in that it is the closest target to a free neutron target and is extremely useful for cross section measurements. ^{3}He is uniquely suited for measurements that involve the spin of the neutron since the dominate state is the ground state where the two protons have anti-parallel spin with respect to each other. This causes the spin of the entire nucleus to be approximately the spin of the neutron. There are complications, as illustrated in Figure 2.1, but the S ground state makes up ~90% of the ^{3}He target wave function.

The simplest method of describing the $^3\mathrm{He}(e, e'n)$ reaction is with the plane wave impulse approximation (PWIA), which is discussed in detail in Section 2.3. Due to using multi-nucleon targets, extra effects from final-state interactions (FSI) and meson-exchange currents (MEC) must be taken into account. These reactions are discussed in detail in Section 2.4. Full three-body calculations, known as Faddeev calculations, are very well suited to describing the ^{3}He states at low energy-transfer. These calculations are discussed in detail in Section 2.6. As energy-transfer

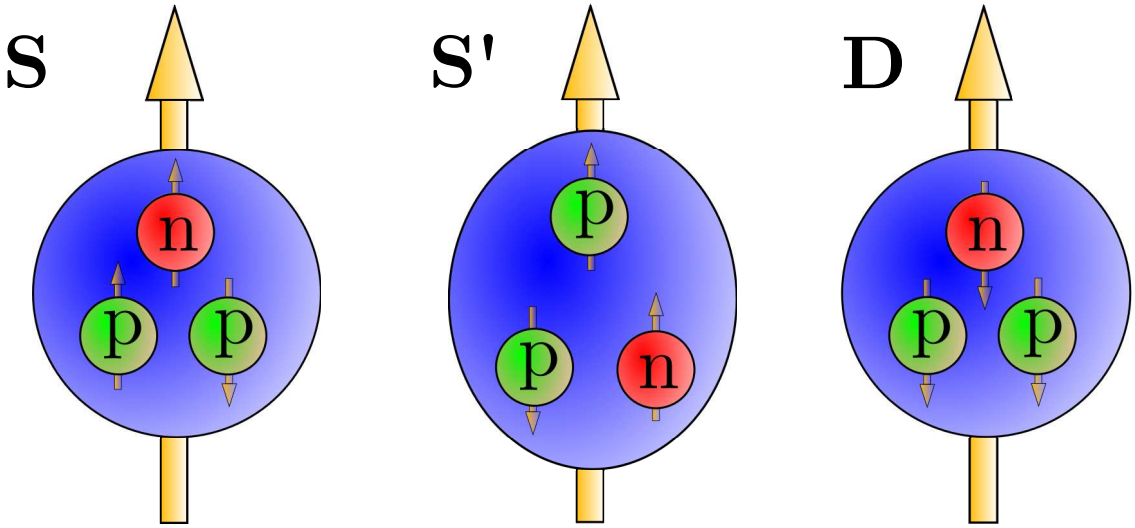

Fig. 2.1: ^{3}He States. This cartoon is a representation of the three most common states of the ^{3}He target. The S ground state makes up approximately 90% of the ^{3}He which makes this nucleus and ideal candidate for studying neutron spin physics.

is increased, relativistic effects must be taken into account. These are much more difficult to calculate, so full calculations are not available.

2.2 Formalism

In order to discuss the ideas presented in this dissertation, a number of definitions must be made. Figure 2.2 demonstrates the reaction channel where an incident electron, e, with energy E, momentum $\vec{k}$, and helicity h interacts with a ^{3}He nucleon at rest through a virtual photon, γ. The scattered electron, e', is deflected at angle $\theta_{e'}$, has energy E', and momentum $\vec{k'}$.

The electron losses some energy through the interaction of the exchanged photon which has energy $\nu = E - E'$ and momentum transfer vector $\vec{q} = \vec{k} - \vec{k'}$. For each of the asymmetries presented in this dissertation, ν is a useful quantity for showing how the asymmetry changes against this energy transfer. The square of the four-vector momentum transfer is defined as $Q^2 = \nu^2 - \vec{q}^{\,2}$ and is a useful quantity

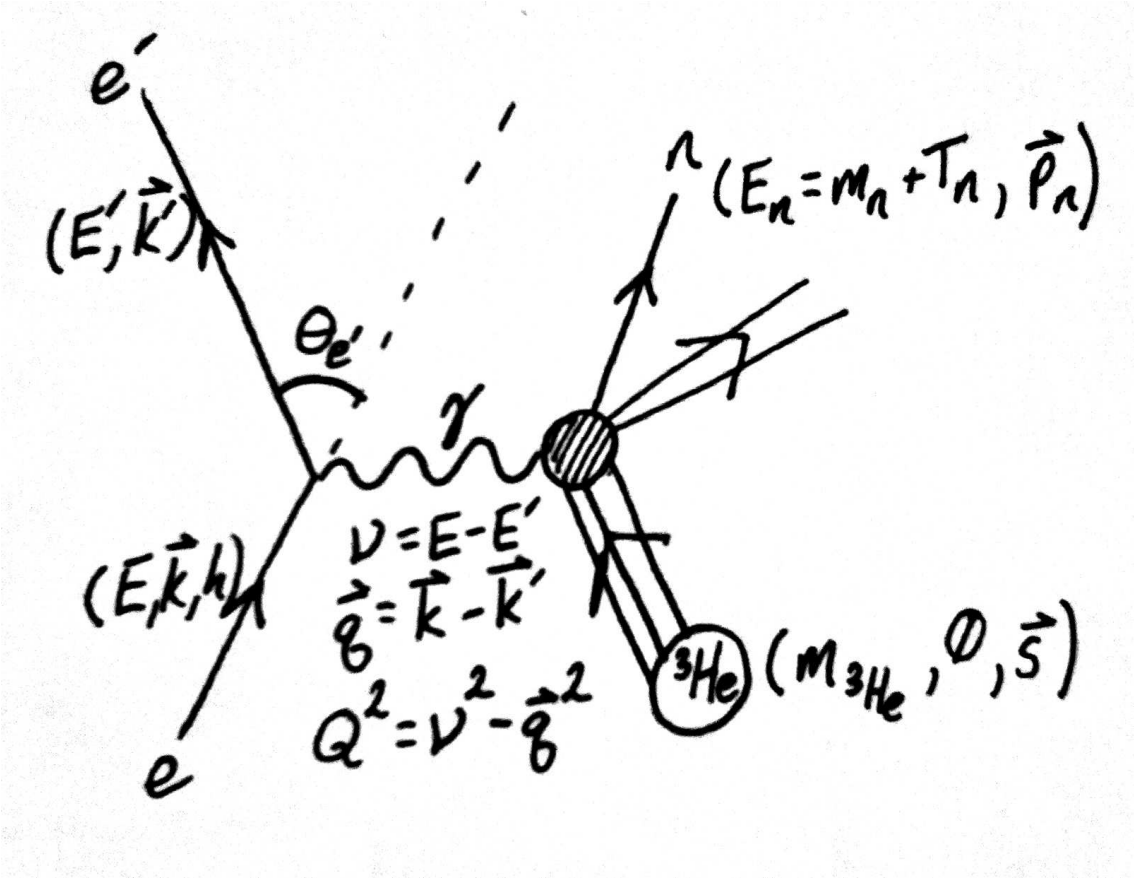

Fig. 2.2: Scattering Definitions. This diagram represents the ^{3}He$(e, e'n)$ reaction.

for showing differences of A_y^0 values. Another useful quantity is the Bjorken scaling variable x_{Bj} which is defined as

$$x_{Bj} = \frac{\mathrm{Q}^2}{2m_N\nu} \tag{2.1}$$

where m_N is the average mass of a nucleon. Quasi-elastic scattering occurs in the energy range where $\nu \approx \mathrm{Q}^2/2m_n$ or, equivalently, where $x_{Bj} \approx 1$.

In addition, the polar (θ^*) and azimuthal (ϕ^*) angles of the target spin direction with respect to q-vector are imperative to translate experimental asymmetries to theoretical calculations. Figure 2.3 represents these angles. The asymmetries

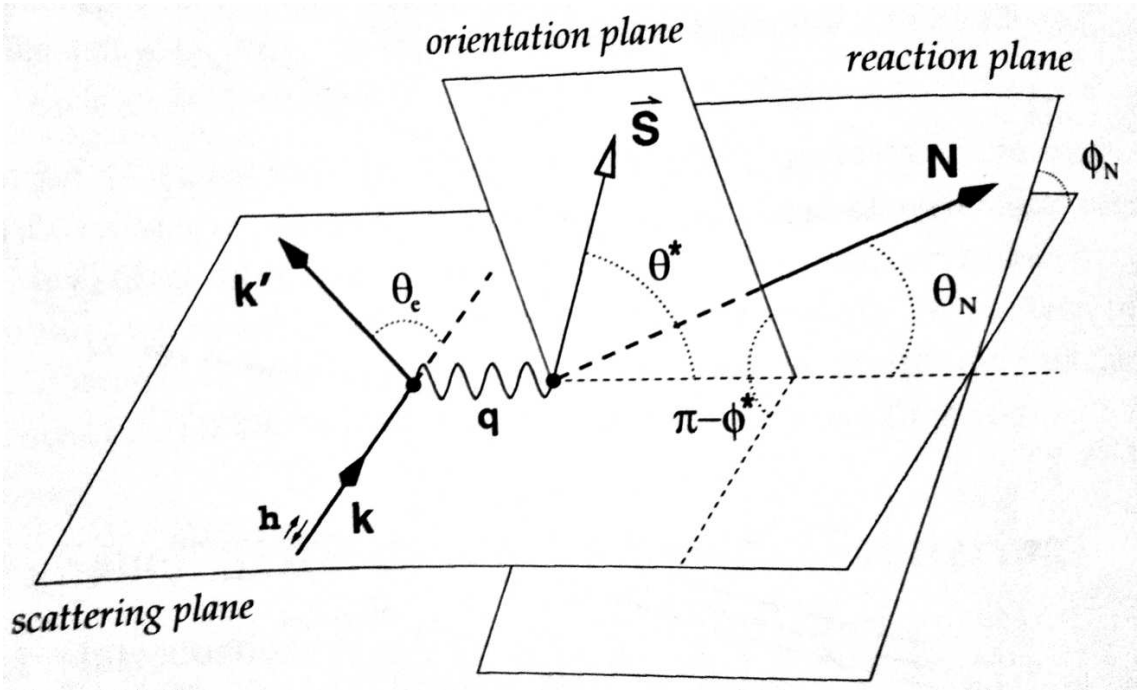

Fig. 2.3: Angle Definitions. This diagram demonstrates how θ^* and ϕ^* are related to the q-vector and the polarization axis.

measured in this experiment are of the form

$$A(\theta^*, \phi^*) = \frac{1}{P} \cdot \frac{Y_\uparrow - Y_\downarrow}{Y_\uparrow + Y_\downarrow} \tag{2.2}$$

where P is the polarization of the target (P_t) for single-spin asymmetries or the polarization of the target times the polarization of the beam ($P_t \cdot P_b$) for double-spin asymmetries, and $Y_{\uparrow(\downarrow)}$ are the yields of spin-up (spin-down) events.

Double-spin asymmetries are commonly used in the extraction of the neutron form factors. In particular, the asymmetries $A_\parallel = A(0°, 0°)$ and $A_\perp = A(90°, 0°)$ can be used to extract the electric form factor of the neutron (G_E^n). In the PWIA this takes the form of

$$G_E^n = \frac{b}{a} \cdot G_M^n \frac{(P_b P_t V)_\parallel}{(P_b P_t V)_\perp} \frac{A_\perp}{A_\parallel} \tag{2.3}$$

where a and b are kinematic factors and $V_{\parallel(\perp)}$ are dilution factors. [9]

It is important to note that due to experimental constraints, the asymmetries measured and discussed in this dissertation, A_T and A_L deviate from $A_\parallel$ and $A_\perp$ (respectively) by a small rotation. However, the vertical target-spin asymmetry measured in this dissertation, A_y^0, is identical to the theoretical $A(90°, 90°)$.

2.3 Plane-Wave Impulse Approximation

The plane-wave impulse approximation (PWIA) is a model for describing electron-nucleon scattering. In the PWIA, it is assumed that a nucleon is cleanly knocked-out of a nucleus due to scattering from an incident electron without rescattering with the residual nucleus. This mechanism is presented as a Feynman diagram in Figure 2.4. In the case of ^{3}He, the residual nucleus is either a deuteron in the case of two-body break-up, or two unbound nucleons in the case of three-body break-up.

In order to understand PWIA, we start with the differential cross section of the electron-nucleon reaction which can be written as a product of two tensors: the

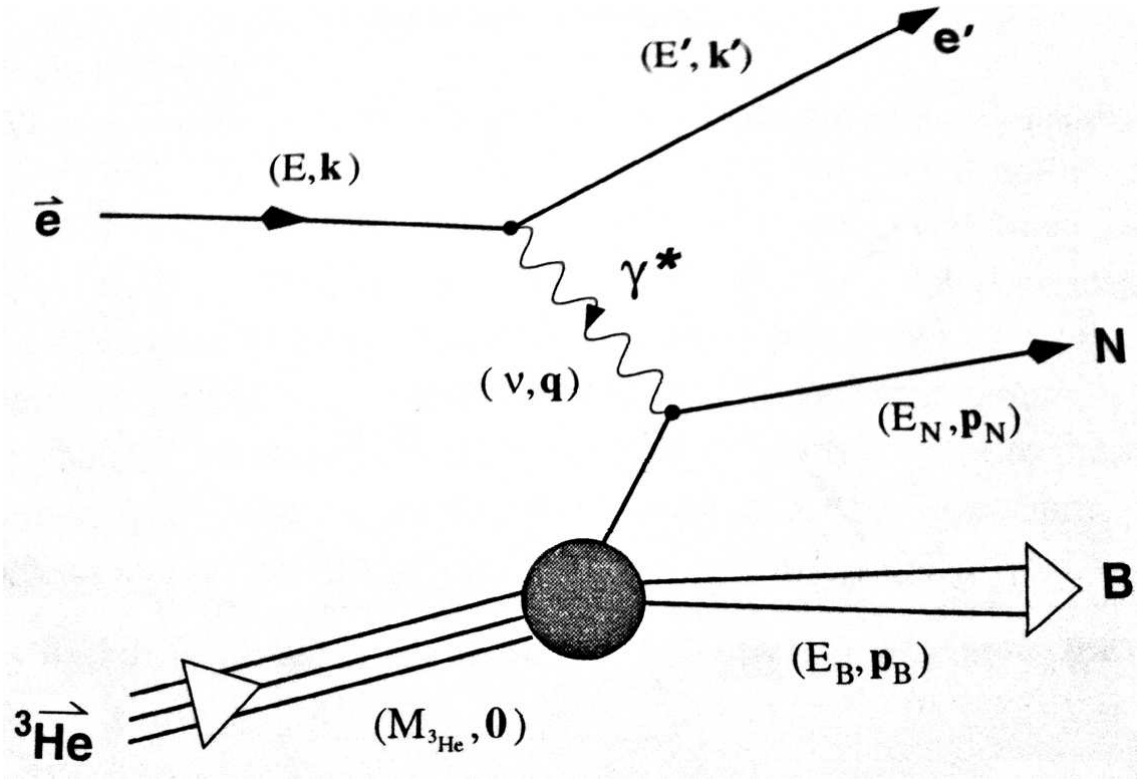

Fig. 2.4: PWIA Diagram. This is the Feynman diagram for plane-wave impulse approximation, adapted from [10].

leptonic tensor, $\eta_{\mu\nu}$, and the hadronic tensor, $W^{\mu\nu}$ such that

$$\frac{d\sigma}{dE'd\Omega_e d\Omega_N dE_N} = \frac{2\alpha^2}{Q^4}\frac{p_N M_n M_b}{(2\pi)^3 E_B}\eta_{\mu\nu}W^{\mu\nu}\delta(E_N + E_B - M_{^3\mathrm{He}} - \nu) \ . \tag{2.4}$$

The hadronic tensor describes all of the nuclear structure and dynamics which is the product of the nuclear electromagnetic transition currents $J^\mu(Q)^*_{fi}J^\nu(Q)_{fi}$. The leptonic tensor has been described in extensive detail in [11] and [12]. In the extreme relativistic case, where $\gamma >> 1$, the helicity of the electron only appears in the antisymmetric part of the tensor. When both tensors are contracted, the resulting expressing can be separated into a symmetric and antisymmetric part by interchanging the indices μ and ν,

$$2\eta_{\mu\nu}W^{\mu\nu} = v_0(R_{fi} + hR'_{fi}) \quad , \tag{2.5}$$

where

$$v_0 \equiv 4EE'\cos^2\frac{\theta_e}{2} \quad . \tag{2.6}$$

The lepton tensor can be projected onto the coordinate system described in Figure 2.3 such that $\hat{z} \parallel \mathbf{q}$, $\hat{y} \parallel (\mathbf{k} \times \mathbf{k}')$, and $\hat{z} \parallel (\hat{y} \times \hat{z})$. This projection yields the kinematic factors v_k and $v_{k'}$ where $k = L, T, TL, TT$ and $k' = T', TL'$ such that the energy transfer ν, the four-momentum square Q^2, and the electron-scattering angle θ_e are within these factors. From this, the six-fold differential cross section can be described as

$$\begin{aligned}\frac{d\sigma^h}{dE'd\Omega_e d\Omega_N dE_N} &= \frac{p_N M_n M_b}{(2\pi)^3 M_{^3\mathrm{He}}}\sigma_{Mott}(R_{fi} + hR'_{fi}) \\ &\equiv \Sigma_{fi} + h\Delta_{fi}\end{aligned} \tag{2.7}$$

which is the sum of a helicity-independent part (Σ_{fi}) and a helicity-dependent part (Δ_{fi}). The polarized and unpolarized cross-sections can be parametrized by two helicity-dependent (primed) and four helicity-independent (unprimed) response functions defined as

$$R_{fi} = v_L R^L_{fi} + v_T R^T_{fi} + v_{TL} R^{TL}_{fi} + v_{TT} R^{TT}_{fi} \quad , \tag{2.8}$$

$$R'_{fi} = v_{T'} R^{T'}_{fi} + v_{TL'} R^{TL'}_{fi} \quad . \tag{2.9}$$

The response functions $R^{T'}_{fi}$ and $R^{TL'}_{fi}$ can be separated out by measuring different kinematic factors v. In the case where only the initial state of the electrons and target are polarized, and where the final state does not have polarization determined, it is possible to describe the components of the cross section in Equation 2.7 in terms of nine structure functions such that

$$\begin{aligned} \Sigma_{fi} \sim \; & v_L W^L_{fi}(\Delta\phi) + v_T W^T_{fi}(\Delta\phi) \\ & + v_{TL}\left[\cos\phi_N W^{TL}_{fi}(\Delta\phi) + \sin\phi_N \widetilde{W}^{TL}_{fi}(\Delta\phi)\right] \\ & + v_{TT}\left[\cos 2\phi_N W^{TT}_{fi}(\Delta\phi) + \sin 2\phi_N \widetilde{W}^{TT}_{fi}(\Delta\phi)\right] \quad , \end{aligned} \tag{2.10}$$

$$\Delta_{fi} \sim v_{T'} \widetilde{W}^{T'}_{fi}(\Delta\phi) + v_{TL'}\left[\sin\phi_N W^{TL'}_{fi}(\Delta\phi) + \sin 2\phi_N \widetilde{W}^{TL'}_{fi}(\Delta\phi)\right] \quad , \tag{2.11}$$

where the structure functions are dependent on the kinematic variables q, ν, θ_N, p_N, E_N, and the target spin orientations θ^* and $\Delta\phi \equiv \phi^* - \phi_N$. In the PWIA, the terms $\widetilde{W}^L_{fi}$, $\widetilde{W}^{TT}_{fi}$, and $W^{TL'}_{fi}$ are equal to zero [13]. If the target is unpolarized, then all terms with a $\widetilde{\ }$ are also equal to zero. Measuring these response functions provides a test for the PWIA as well as any perturbations to the approximation which could be caused by FSI or MEC.

In the PWIA, the electromagnetic current of the nucleus is the sum of currents of A free nucleons. These nucleons are bound inside the nucleus which causes them to be off-shell which causes current conservation to be broken. Because of this, the PWIA is am ambiguous formalism and arbitrary choices need to be made for an off-shell extrapolation of the PWIA on-shell vertex[14]. The half-off-shell γNN vertex generally involves the four form factors[15] which can be extrapolated to the Pauli and Dirac form factors, or the two Sachs form factors, of the nucleon [16].

Various extrapolations [13][16] have been presented in order to find an expression for the spin-dependent off-shell electron-nucleon cross section, $\sigma_{\hat{\sigma}}^{eN}$, which results from the fact that the electromagnetic current is a one-body operator in the PWIA[17]. From these descriptions, $\sigma_{\hat{\sigma}}^{eN}$ is reduced to the single-nucleon cross section where the kinematics are on-shell. In the pPWIA, this cross section connects the leptonic tensor to part of the hardronic tensor (from Equation 2.4) that depends on the γNN vertex presented in Figure 2.4 and the beginning of this section. The general cross section can now be described in terms of the product of $\sigma_{\hat{\sigma}}^{eN}$ and the spin-dependent spectral function $S_{\hat{\sigma}}^{N}(\mathbf{p}, E_s, \Omega^*)$ [13][18] by

$$\frac{d\sigma^h}{dE' d\Omega_e d\Omega_N dE_N} = \frac{p_N M_N M_{rec}}{E_{rec}} \sum_{\hat{\sigma}} \sigma_{\hat{\sigma}}^{eN} S_{\hat{\sigma}}^{N}(\mathbf{p}, E_s, \Omega^*) \tag{2.12}$$

where $S_{\hat{\sigma}}^{N}(\mathbf{p}, E_s, \Omega^*)$ is the probability density of finding a nucleon N with separation energy E_s, three-momentum $\mathbf{p}$, and spin projection, $\hat{\sigma} = +(-)$, parallel (antiparallel) to the spin of the ^{3}He nucleus. The general form of the spectral function

is

$$S^N_{\hat{\sigma}}(\mathbf{p}, E_s, \Omega^*) = \frac{1}{2}\Big\{ f^N_0(p, E_s) + f^N_q(p, E_s)\sigma_N \cdot \sigma_{^3\mathrm{He}} + f^N_2(p, E_s)\left[(\sigma_N \cdot \hat{\mathbf{p}})(\sigma_{^3\mathrm{He}} \cdot \hat{\mathbf{p}}) - \frac{1}{3}\sigma_N \cdot \sigma_{^3\mathrm{He}}\right]\Big\} \tag{2.13}$$

where $f^N_0(p, E_s)$ is a spin-averaged function and $f^N_1(p, E_s)$ and $f^N_1(p, E_s)$ are two spin-dependent functions. Each of these is described in detail in [18] in terms of the momentum-space partial wave of the ^{3}He ground state wave function. The spectral function is directly related to the tri-nucleon bound state and can be described by

$$S^N_{\hat{\sigma}}(\mathbf{p}, E_s, \Omega^*) = \frac{1}{(2\pi)^3}\sum_A \mathcal{P}(A)\sum_B \left\{\left\langle \psi_{^3\mathrm{He}}\right| a^+_{p\hat{\sigma}'}\left|\psi_B\right\rangle \left\langle \psi_B\right| a_{p\hat{\sigma}}\left|\psi_{^3\mathrm{He}}\right\rangle\right\}\delta(E_s - E_{^3\mathrm{He}} - E_B) \tag{2.14}$$

where $\left|\psi_{^3\mathrm{He}}\right\rangle$ is the ^{3}He bound state solution with binding energy $E_{^3\mathrm{He}}$ and $|\psi_B\rangle$ is the wave function of the remaining nucleons with internal excitation energy E_B, and $a^+_{p\hat{\sigma}'}$ ($a_{p\hat{\sigma}}$) is the creation (annihilation) operator. Summing over B takes all nucleon subsystems of the final state into account and summing over A weighted by $\mathcal{P}(A)$ yields the distribution of the ground state angular momentum, J_A, over the nuclear substrates M_{J_A}. The result of Equation 2.14 can be used to determine the six-fold differential cross section.

In order to relate the cross section of Equation 2.12 to measurable observables, this cross section can be written as

$$\frac{d\sigma(h, S)}{d\Omega_e dE_e d\Omega_n dp_n} = \frac{d\sigma^0}{d\Omega_e dE_e d\Omega_n dp_n} \times [1 + \mathbf{S}\cdot\mathbf{A^0} + h(A_e + \mathbf{S}\cdot\mathbf{A}')] \tag{2.15}$$

where h is the helicity of the electron, $\mathbf{S}$ is the spin of the ^{3}He target, σ^0 is the

spin-averaged cross section, $\mathbf{A^0} \equiv (\mathbf{A^0_x}, \mathbf{A^0_y}, \mathbf{A^0_z})$ are the target analyzing powers, A_e is the electron analyzing power, and $\mathbf{A'} \equiv (\mathbf{A'_x}, \mathbf{A'_y}, \mathbf{A'_z})$ are the spin-correlation asymmetries. In this calculation, $A'_y = A^0_x = A^0_z = 0$. In the PWIA, due to a combination of time reversal invariance and hermiticity of the transition matrix, A^0_y is exactly zero. As such, any measurement of A^0_y that is non-zero is indicative of higher-order effects such as FSI and MEC.

2.4 Final-State Interactions and Meson-Exchange Currents

Because there is no free neutron target, the reaction mechanism of neutron scattering from nuclei must take into account effects from the nuclear medium. In particular, final-state interactions (FSI) and meson-exchange currents (MEC) must be accounted for.

Final-state interactions occur when the knocked-out nucleon interacts again with the remaining nucleons. An example diagram of this type of interaction is presented in Figure 2.5. Naively, as the momentum-transfer is increased, the amount of time that such interactions can occur in is decreased and so it would be expected to see effects of FSI drop off at higher Q^2. The PWIA does not include such effects, although Laget has perturbed the approximation to include them as discussed in Section 2.5. They are calculated exactly in full Faddeev calculations which are discussed in detail in Section 2.6.

Meson-exchange currents occur when the incident electron produces mesons, such as π- and ρ-mesons, which are exchanged with the nucleons in ^{3}He. The contribution of these effects is expected to be much smaller than FSI, especially at lower Q^2, although still important in understanding the interactions that occur in $^3\mathrm{He}(e, e'n)$ scattering. In the case of Laget's calculation, MEC are taken as a further

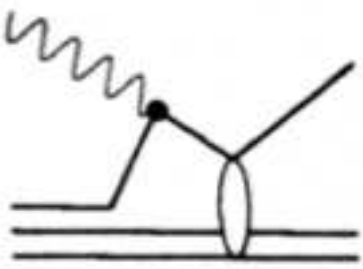

Fig. 2.5: FSI Example. The diagram presented here is an example of final-state interactions where the recoiling nucleon interacts with the rest of the nuclear system after the initial scattering from the incident electron.

perturbation of PWIA. In the full Faddeev calculations, MEC are included in the the nucleon-nucleon potential. Each of these cases only accounts for π- and ρ-meson exchange currents, ignoring heavier mesons. Diagrammatic examples of MEC are presented in Figure 2.6.

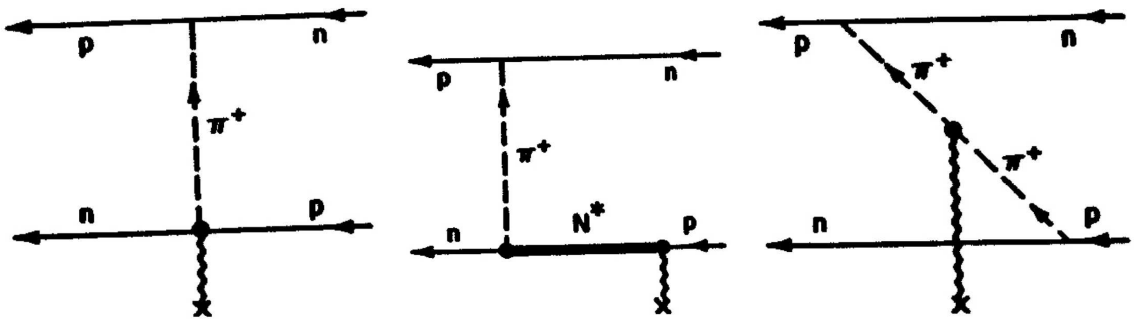

Fig. 2.6: MEC Examples. The diagrams presented here are examples meson-exchange currents where the incident electron excites the nuclear state in a manner that it produces mesons, such as π- and ρ-mesons, which interact with the nucleons.

2.5 Original Laget Calculations

In the early 1990s, Laget was working on calculations to estimate the effects of FSI and MEC in the ^{3}He(e,e'n) reaction. This work was based on the PWIA and included effects from FSI and MEC. Although his calculations at the time underestimated the effects from FSI and MEC, the qualitative understanding of

these calculations still holds.

The general expression of the cross section for (e,e'n) reactions is described as

$$\frac{d\sigma(h,S)}{d\Omega_e dE_e d\Omega_n dp_n} = \frac{d\sigma^0}{d\Omega_e dE_e d\Omega_n dp_n} \times [1 + \mathbf{S}\cdot\mathbf{A^0} + h(A_e + \mathbf{S}\cdot\mathbf{A'})] \tag{2.16}$$

where h is the helicity of the electron, $\mathbf{S}$ is the spin of the target, σ^0 is the unpolarized cross section, $\mathbf{A^0}$ is the target asymmetry when the target is unpolarized, A_e is the electron asymmetry when the target is unpolarized, and $\mathbf{A'}$ is the spin transfer asymmetry when both the beam and target are polarized.

The components of the spin transfer polarization of the outgoing nucleon are of the form

$$\sigma^0 P'_y = \left(\frac{-q^2\epsilon(1-\epsilon)}{2\nu^2}\right)^{1/2} \sin\phi\sigma'_{TL}(y) \tag{2.17}$$

$$\sigma^0 P'_{x,z} = -\left(\frac{-q^2\epsilon(1-\epsilon)}{2\nu^2}\right)^{1/2} \cos\phi\sigma'_{TL}(x,z) + (1-\epsilon^2)^{1/2}\sigma'_{TT}(x,z) \tag{2.18}$$

where ν, q^2, and ϵ are the energy, squared mass, and the polarization of the virtual photon respectively and $\sigma'_{TT(TL)}$ are the transverse-transverse (transverse-longitudinal) interference cross sections. In coplanar geometry, $P'_y = P^0_x = A'_y = A^0_x = A^0_z = 0$ due to the sin and cos terms.

In PWIA, due to a combination of time reversal invariance and hermiticity of the transition matrix, $P^0_y = A^0_y = 0$. Laget perturbs the PWIA by including FSI and MEC, diagrams of which are shown in Figure 2.8, which cause $P^0_y \neq 0$ and $A^0_y \neq 0$. Before A^0_y was experimentally measured, Laget estimated these effects from FSI and MEC to play an important role at low Q^2 and to drop off as the momentum-transfer increased as shown in Figure 2.7.[7]

Since this time, Laget has updated his calculations to meet with experimental constraints, however the full range has not been calculated as it is shown here.

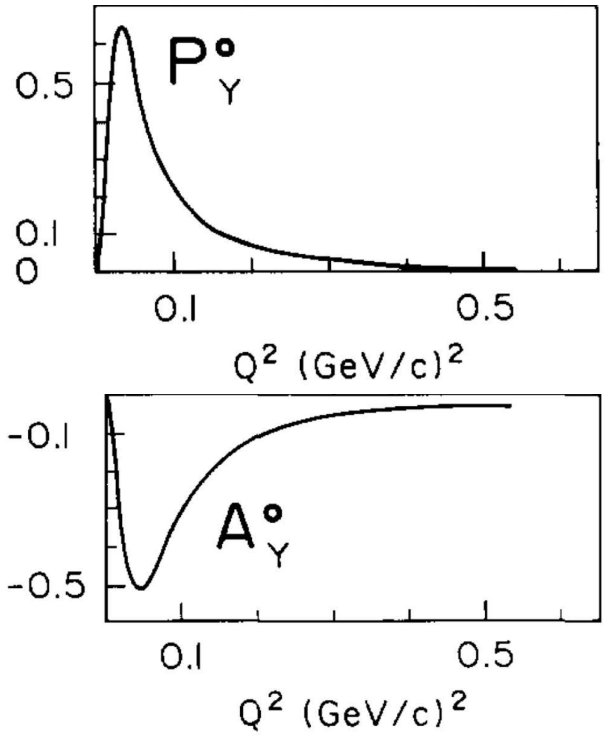

Fig. 2.7: Original Laget Calculations. This plot shows the results from the original Laget calculations form P_y^0 and A_y^0. Although Laget has since updated his calculations to include larger effects due to FSI and MEC, they are only calculated for individual Q^2 values and not for the range presented here. [7].

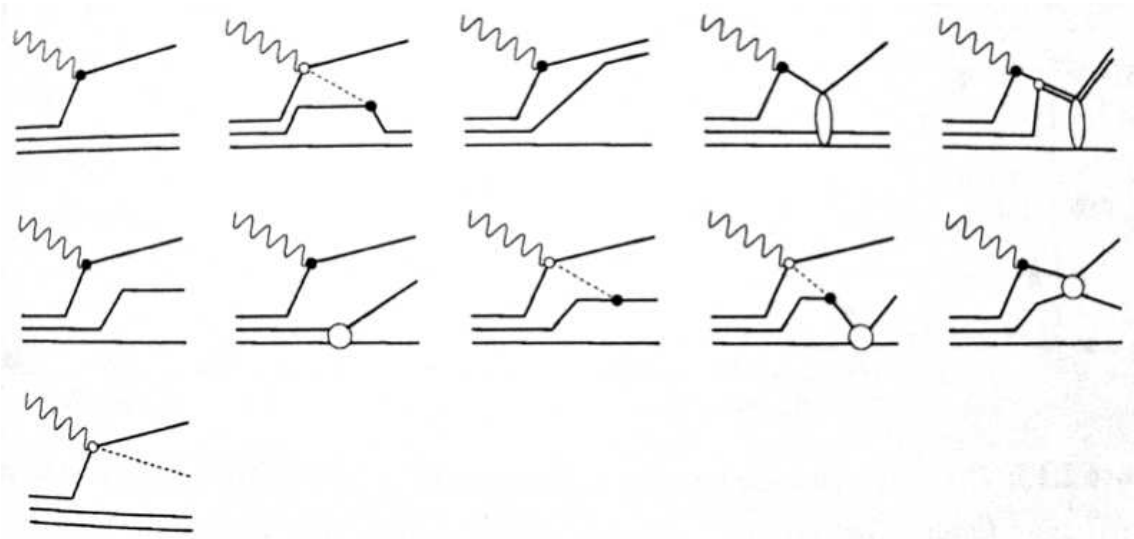

Fig. 2.8: Diagrams Chosen by Laget. The diagrams presented here are the perturbations of PWIA that Laget included in his analysis of A_y^0. The top row consists of diagrams of two-body break-up, the center row of three-body break-up, and the bottom diagram is for pion electroproduction. [8].

Although the magnitude of the effects of FSI and MEC are larger than was originally expected, qualitatively this understanding of A_y^0 still holds.

2.6 Faddeev Calculations

Faddeev calculations are full calculations of the three-body Schrödinger equation in non-relativistic kinematics. Processes such as MEC are absorbed into the nucleon-nucleon potential. They consist of a set of coupled integral equations that have unique solutions for three-body scattering. These calculations have been done by the Bochum group for A_y^0, $A_\parallel$, and $A_\perp$ at low Q^2.

Faddeev showed that rearranging the perturbation series of the scattering T-matrix will lead to unique solutions of the 3N Schrödinger equation. This system includes two-body and three-body interactions, all of which have a finite range beyond which the force acting on all three nucleons becomes negligible.

The three particles are labeled i, j, and $k = 1, 2, 3$ such that $i \neq j \neq k$ as shown in Figure 2.9 where j and k are interacting and i is a spectator. In these coordinates, the center of mass of the system is fixed by setting the total momentum, P, equal to zero. The momentum of the spectator particle, $\mathbf{q}_i$ is defined with respect to the center of mass of the interacting particles with momentum $\mathbf{p}_i$. The masses of the particles are defined as m_i. In momentum space, the independent variables are

$$\mathbf{P} = \sum_{i=0}^{3} \mathbf{k}_i \equiv 0, \quad \mathbf{p}_1 = \frac{\mathbf{k}_2 - \mathbf{k}_3}{2}, \quad \mathbf{q}_1 = \frac{2\mathbf{k}_1 - (\mathbf{k}_2 + \mathbf{k}_3)}{3} \tag{2.19}$$

where $\hbar = 1$, $m_1 = m_2 = m_3$, $M = 3m$, $\mu_p = m/2$ is the reduced mass of the interacting particles and $\mu_q = 2m/3$ is the reduced mass of the entire system. The

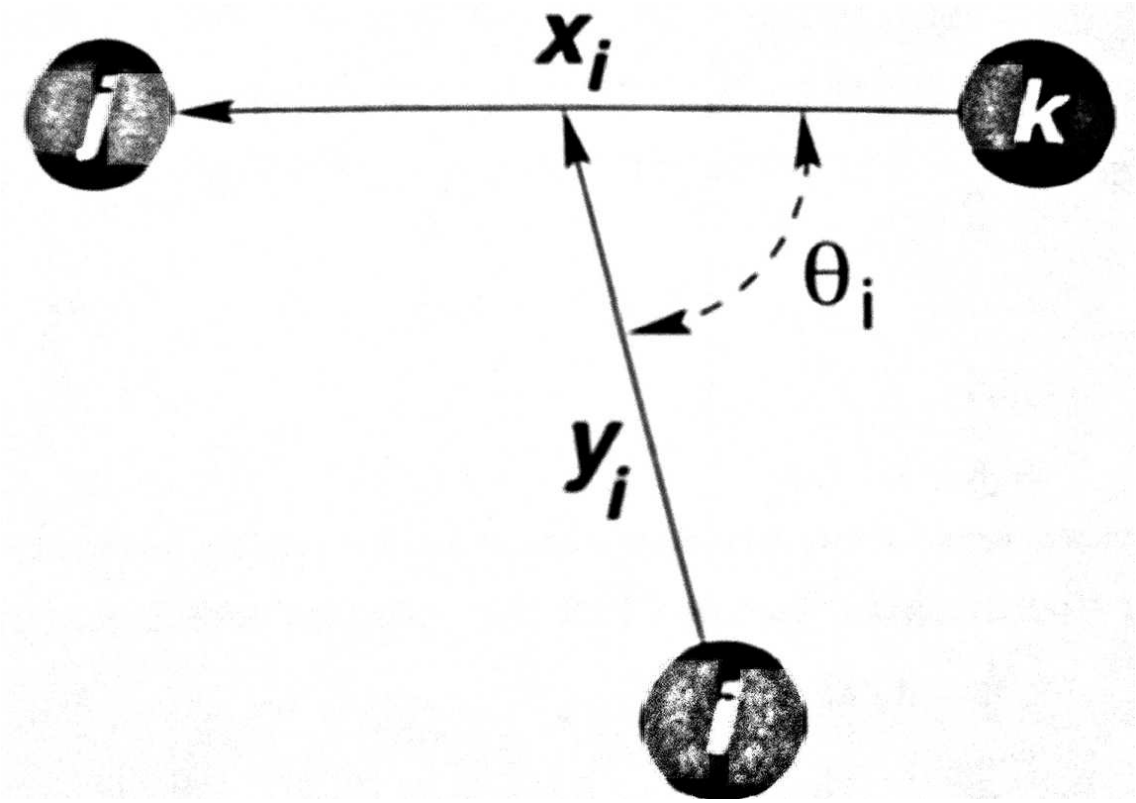

Fig. 2.9: Three-Body Coordinates. This cartoon identifies the three independent Jacobi coordinates for the three-body system where particles j and k interact and particle i is a spectator. The spacial relations, x_i and y_i, also correspond to the momentum $\mathbf{p}_i$ and $\mathbf{q}_i$, respectively.

non-relativistic Schrödinger equation for this system is defined as

$$(E - H)\,|\Psi\rangle = (E - H_0 - V)\,|\Psi\rangle = 0 \tag{2.20}$$

where

$$H_0 = \sum_{i=1}^{3} \frac{\mathbf{k}_i \cdot \mathbf{k}_i}{2m_i} = \frac{P^2}{2M} + \frac{p_i^2}{2\mu_p} + \frac{q_i^2}{2\mu_q} \quad , \text{ and} \tag{2.21}$$

$$V_0 = \sum_{i=1}^{3} V_i = V_0 + V_1 + V_2 + V_3 \quad . \tag{2.22}$$

The free Hamiltonian is described above by H_0, the interaction between the particles is defined as V which is the sum of three independent nucleon-nucleon potentials (V_i where $i = 1, 2, 3$) and one three-body potential, V_0. In order to keep the computation relatively simple, V_0 is usually neglected. This is the case in Equation 2.20. Although not described in detail here, it should be noted that the Coulomb potential is also included in the full Faddeev calculations by the Bochum group.

In order to solve the Schrödinger equation, Green's functions are introduced which take the form of

$$G(z) \equiv (z - H)^{-1} \;\text{ and }\; G_0(z) \equiv (z - H_0)^{-1} \tag{2.23}$$

where z is a variable with dimensions of energy. These functions are related by

$$\begin{aligned} G(z) &= G_0(z) + G_0(z) V G(z) \\ &= G_0 + G_0 V G_0 + G_0 V G_0 V G_0 + \cdots \end{aligned} \tag{2.24}$$

The transition operator, $T(z)$, is related to the potential V by the Lippman-Schwinger

equation such that

$$\begin{aligned} T(z) &= V + VG_0(z)T(z) \\ &= V + VG(z)V \quad . \end{aligned} \tag{2.25}$$

If the potential V from Equation 2.22 is substituted into Equation 2.25, then the equation can be expanded into an infinite series where the operator G_0 is the propagator of the non-interacting three-body system and the two-body interaction V_i is an intermediary connecting particles j and k. The corresponding Green's function to this expansion is defined as

$$\begin{aligned} G =& G_0 + G_0 \sum_i V_i G_0 + G_0 \sum_i V_i G_0 \sum_j V_j G_0 \\ &+ G_0 \sum_i V_i G_0 \sum_j V_j G_0 \sum_k V_k G_0 + \cdots \end{aligned} \tag{2.26}$$

which can be expressed graphically as presented in Figure 2.10.

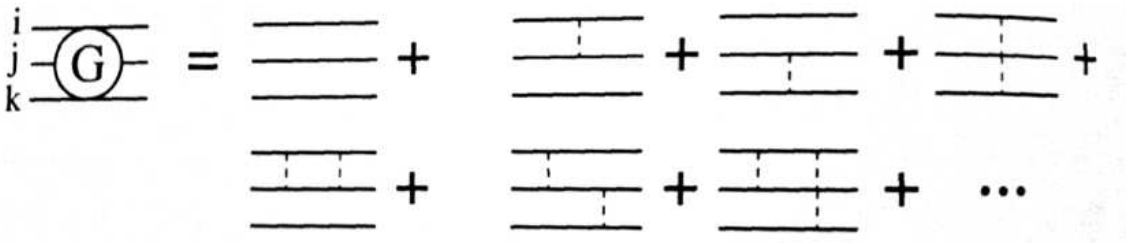

Fig. 2.10: Green's Function Expansion. This series of diagrams is the expansion of the Green's function operator, $G(z)$, in terms of the free propagator, G_0, and two-body interactions.

Within the expansion displayed in Figure 2.10 there are three infinite series of disconnected diagrams. One of these is displayed in Figure 2.11. The non-interacting particle has an unchanging momentum which causes a δ-function to remain in the momentum representation. The series of diagrams where one particle

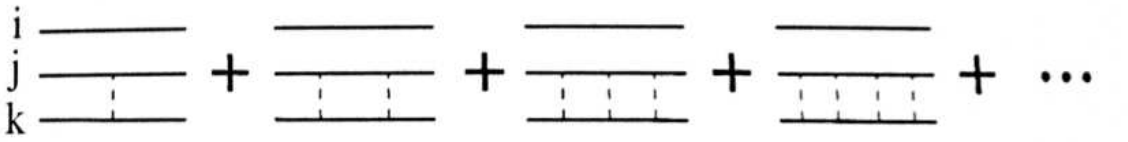

Fig. 2.11: Disconnected Diagrams. The infinite series displayed in Figure 2.10 contains three subsets which each contain and infinite number of disconnected diagrams where the spectator particle does not interact with the other two. This is an example of one of those series where i is the non-interacting particle.

is disconnected corresponds to the two-body T-matrix in 3N-space. The two-body transition operator, T_i, can similarly be defined as

$$T_i \equiv V_i + V_i G_0(z) T_i \quad . \tag{2.27}$$

From this, the channel Green's function can be defined as

$$G_i \equiv (z - H_0 - V_i)^{-1} \tag{2.28}$$

and is presented in diagrammatic form is Figure 2.12.

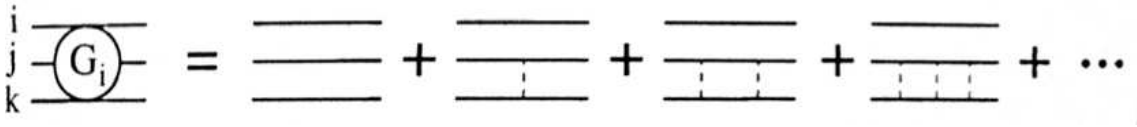

Fig. 2.12: Channel Operator Diagrams. The series displayed here corresponds to the infinite series of disconnected diagrams for the channel operator G_i.

Faddeev described the full operator as the composition of four pieces defined as

$$G(z) = G_0(z) + G^{(1)}(z) + G^{(2)}(z) + G^{(3)}(z) \tag{2.29}$$

where $G_0(z)$ is the free propagator and $G^{(i)}(z)$ are three Faddeev components. These components are displayed in diagrammatic form in Figure 2.13. Through the use of G_i, all subsets where only two particles interact are defined in one term.

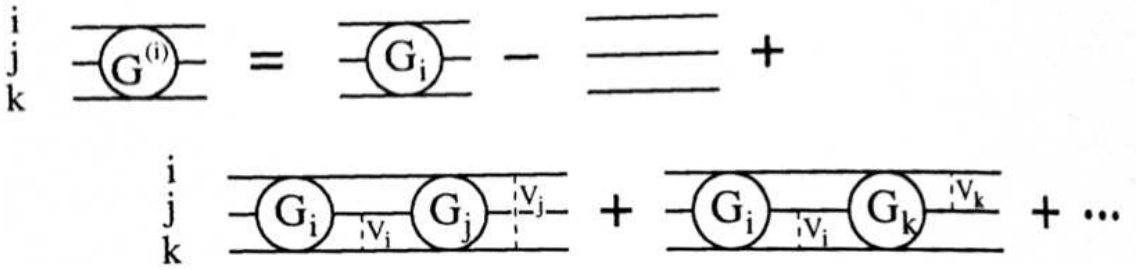

Fig. 2.13: Faddeev Component. The series displayed is an expansion of one of the Faddeev components $G^{(i)}(z)$ in terms of the channel Green's function G_i.

The final term in Figure 2.13 can be expanded out as represented in Figure 2.14. The Faddeev component $G^{(i)}$ always starts with an interaction between particles i and j and ends with an interaction between particles i and j or i and k. Permutations of this component where the diagrams differ only by which particles are interacting are defined as $G^{(j)}$ and $G^{(k)}$ which leads to the coupling described in Equation 2.29.

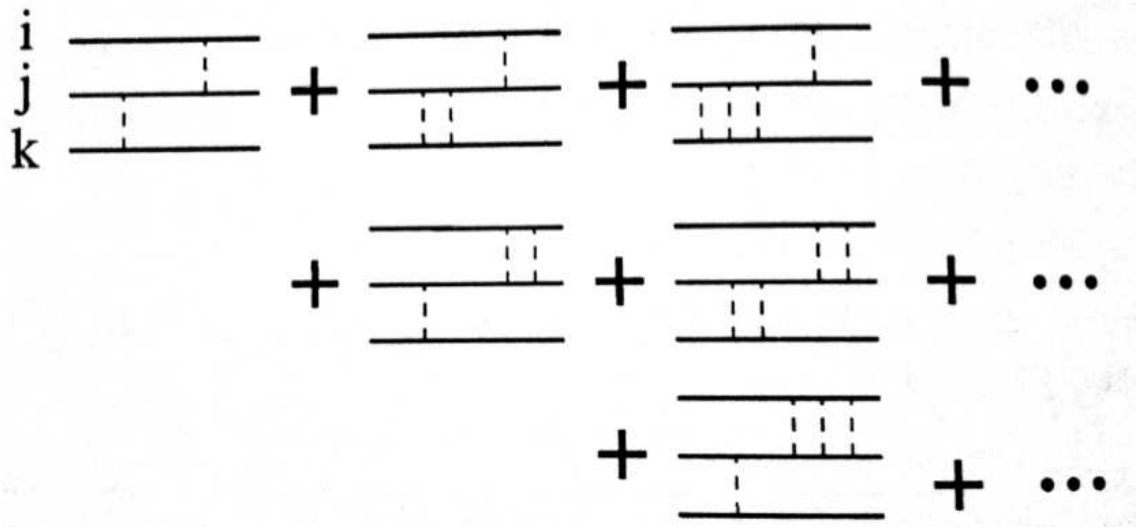

Fig. 2.14: Multiple Interaction Term Expansion. The final diagram in Figure 2.13 is expanded in detail here. The Faddeev component always starts with an interaction between particles i and j and ends with an interaction between particles i and j or i and k.

In order to solve the non-relativistic Schrödinger equation described in Equation 2.20, the wave function is decomposed into three Fadeev calculations. The wave

function is thus described by

$$|\Psi\rangle \equiv |\Phi_0\rangle + \sum_{i=1}^{3} |\psi_i\rangle^F \tag{2.30}$$

where

$$|\Phi_0\rangle = \lim_{\epsilon\to 0} i\epsilon G_0 |\Phi_0\rangle \quad \text{and} \quad |\psi_i\rangle^F = \lim_{\epsilon\to 0} i\epsilon G^{(i)} |\Phi_0\rangle \tag{2.31}$$

Each of the Faddeev components, $|\psi_i\rangle^F$ can be written as the decomposition of the full Green's function $G(z)$ and the solution $|\phi_i\rangle$ of the channel Hamiltonian $H_i = H_0 + V$ where $|\phi_i\rangle$ is the product of a bound state two-body wave function and a plane wave for a single free particle. The eignenvalue of $H_i |\phi_i\rangle$ is given by

$$H_i |\phi_i\rangle = \left(\epsilon_i + \frac{3}{4m} q_i^2\right) |\phi_i\rangle = E_{q_i} |\phi_i\rangle \tag{2.32}$$

where ϵ_i is the binding energy of the two-body system. It is required to solve the Faddeev equations for both the bound state and the continuum in order to describe electron scattering from a ^{3}He nucleus. The Faddeev equations can be described in diagrammatic form as shown in Figure 2.15 or in matrix notation as

$$\begin{bmatrix} |\psi_1\rangle^F \\ |\psi_2\rangle^F \\ |\psi_3\rangle^F \end{bmatrix} = \begin{bmatrix} |\Phi_0\rangle \\ 0 \\ 0 \end{bmatrix} + \begin{bmatrix} 0 & T_1(z) & T_1(z) \\ T_2(z) & 0 & T_2(z) \\ T_3(z) & T_3(z) & 0 \end{bmatrix} G_0(z) \begin{bmatrix} |\psi_1\rangle^F \\ |\psi_2\rangle^F \\ |\psi_3\rangle^F \end{bmatrix} \tag{2.33}$$

The full Faddeev calculations have been solved exactly by the Bochum group for low Q^2 where relativistic effects are not necessary. They are presented along with the experimental values measured for A_y^0 in this dissertation and include contributions from both FSI and MEC. In addition, calculations have been done for both the ^{3}He$(e, e'd)$ and ^{3}He$(e, e'p)$ channels which, when constrained to experimental data,

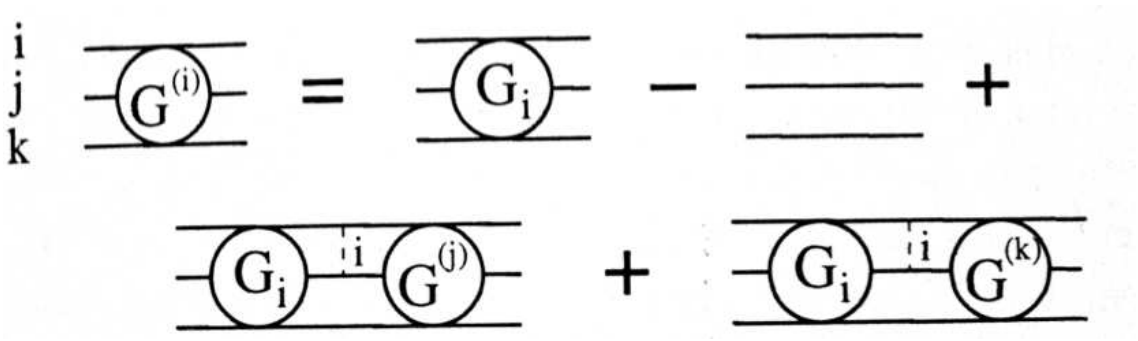

Fig. 2.15: Faddeev Equations. This set of diagrams is equivalent to the Faddeev equations given in Equation 2.33.

give information into the contributions of the S, S', and D states of ^{3}He.

Chapter 3

Setup of the Experiment

3.1 Overview of CEBAF and Hall A

The experiment presented in this dissertation used the Jefferson Laboratory's Continuous Electron Beam Accelerator Facility (CEBAF) and was performed in experimental Hall A. CEBAF is a superconducting radio frequency electron accelerator which was able to provide a beam with polarization greater than 80% and energies up to 6 GeV. An overhead picture of the lab can be seen in Figure 3.1. The accelerator is discussed in detail in Section 3.2.

Fig. 3.1: Aerial View of Jefferson Lab.

Hall A contained equipment which included two High Resolution Spectrometers (HRS), the Hall A Neutron Detector (HAND), and a polarized ^{3}He target

capable of being polarized in three orthogonal directions. A schematic of the equipment used in Hall A can be seen in Figure 3.2. The equipment in Hall A is discussed in detail in Section 3.3.

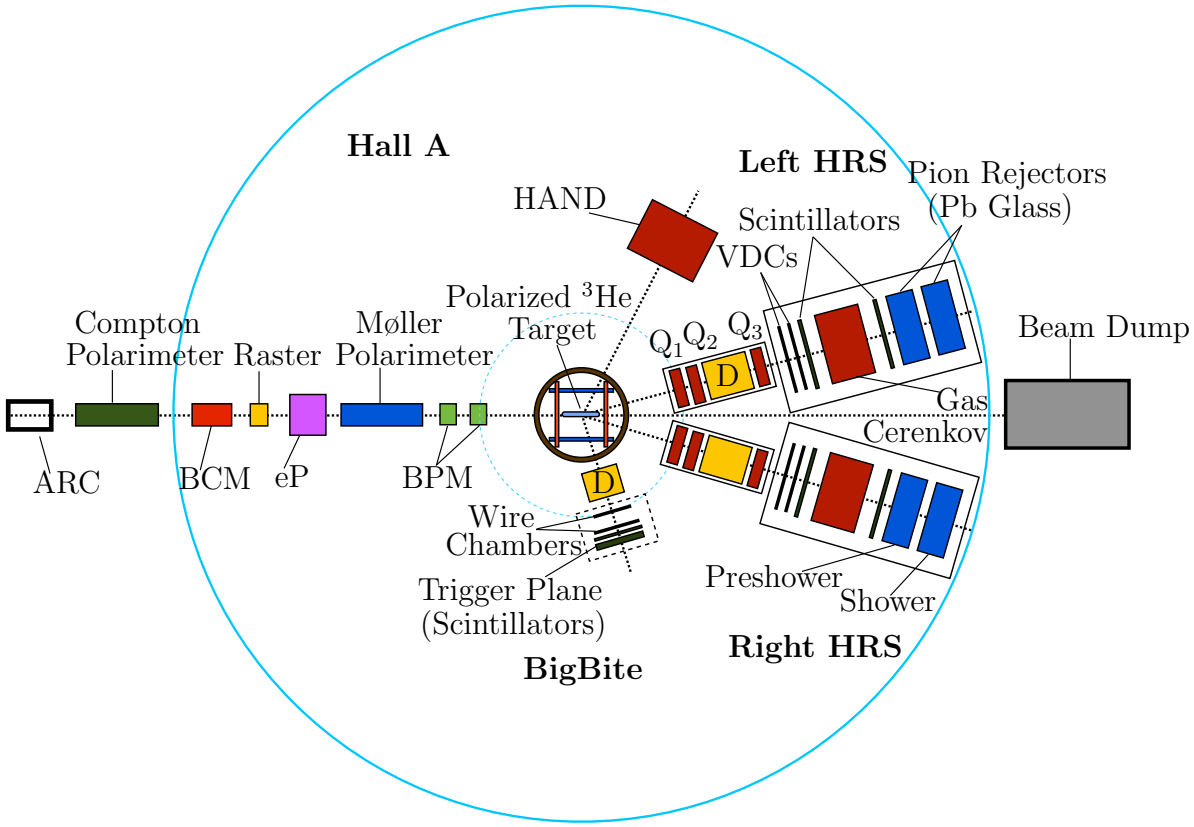

Fig. 3.2: Hall A Experimental Setup. This shows all of the Hall A equipment that was in place during this experiment. The beam line downstream from the target (towards the right in the schematic) corresponds to a 0° angle.

Due to an improved polarized ^{3}He target, this experiment was able to take measurements with the target polarized in each of the three orthogonal directions. This is the first time that an experiment has simultaneously measured the $^3\mathrm{He}(e, e'n)$ asymmetries with the polarization in three dimensions. Details of the kinematics used during this experiment are discussed in Section 3.4.

3.2 CEBAF and the Electron Beam

Jefferson Lab's CEBAF is able to produce an 80%-polarized, continuous-wave electron beam. The beam starts as a polarized electron source which enters the main accelerator through the injector. It is accelerated up to 6 GeV by two superconducting radio frequency (SRF) linear accelerators and two sets of recirculating arcs. The beam can be circulated up to five times with each pass increasing the energy by up to 1.2 GeV. The final beam is able to be simultaneously sent to the three different experimental halls by a beam switchyard. Each experimental hall can receive beam and different energies, so long as they are integer multiples of a single pass. The different components of CEBAF are described in detail below.

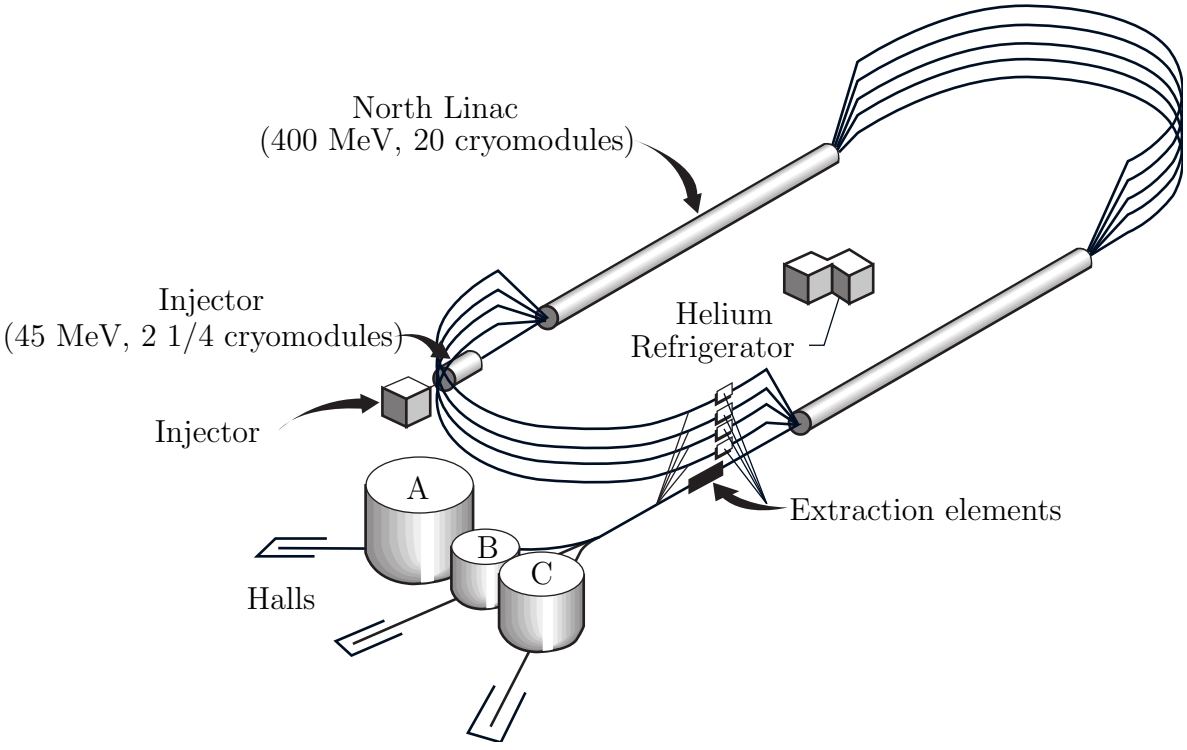

Fig. 3.3: CEBAF Layout. This shows the layout of the Continuous Electron Beam Accelerator Facility.

3.2.1 Injector

The polarized electron source is a GaAs cathode that is hit by a circularly polarized laser beam. A Pockels cell causes changes to occur in the laser polarization every 33.3 ms which in turn causes a flip in the helicity of the electrons every 33.3 ms. In order to reduce systematic effects dependent on the beam helicity, a half-wave plate can be inserted which reverses the beam's helicity.

These newly-polarized electrons are accelerated to 100 keV and injected into the main accelerator through two superconducting radio-frequency (SRF) cavities. These two SRF cavities are referred to as a quarter-cryomodule, since the main accelerator consists of cryomodules that each contain eight SRF cavities.

3.2.2 Linear Accelerators

The heart of CEBAF is the niobium SRF linear accelerators (LinAcs). There are two sets of these, one towards the north and one towards the south as shown in Figure 3.3. Each contains 20 cryomodules which in turn each contain 8 SRF cavities. Superfluid He is used to keep the niobium at a superconducting temperature of 2 K. In the LinAcs, electrons are accelerated up to 600 MeV before entering a recirculating arc which will allow them to be accelerated again. Due to the unique construction of Jefferson Lab, electrons may pass through the LinAcs up to five times.

3.2.3 Recirculating Arcs

The recirculating arcs consist of a dipole "spreading" magnet, followed by a series of dipole magnets which steer the electron beam into a 180° arc, and a final dipole "recombining" magnet. Each arc contains a beam pipe for electrons at

each pass energy. Lower energy electrons, which are easier to steer, are diverted to the higher arcs while higher energy electrons through the lower arcs. Each of the different energy beams are then re-combined at the end of the arc to be put through the LinAcs again.

3.2.4 Beam Switchyard

The beam switchyard is used to send beam to each of the lab's experimental halls. It consists of RF separators, septa, and dipole magnets which separate and divert the beam.

3.3 Hall A

This experiment was performed in Hall A of Jefferson Lab which is uniquely suited to measuring $^3\mathrm{He}(e,e'n)$ asymmetries due to its high resolution spectrometer (HRS), polarized ^{3}He target, and neutron detector. The Hall also contains the Big Bite spectrometer, as well as a second HRS that were used for the simultaneous measurements of the $^3\vec{\mathrm{He}}(\vec{e},e'p)$, $^3\vec{\mathrm{He}}(\vec{e},e'd)$, $^3\vec{\mathrm{He}}(\vec{e},e')$, and $^3\mathrm{He}^{\uparrow}(e,e')$ asymmetries and which are explored in detail by M. Mihovilovic[19], G. Jin[20], and Y.-W. Zhang[21]. Figure 3.4 shows the placement of the equipment used for the $^3\mathrm{He}(e,e'n)$ asymmetries in Hall A.

3.3.1 Beam Measurements

Several pieces of equipment were used in order to understand the incoming electron beam incident upon the target. A variety of parameters were measured, an overview of which can be seen in Table 3.1 and details of which are presented in the sections below.

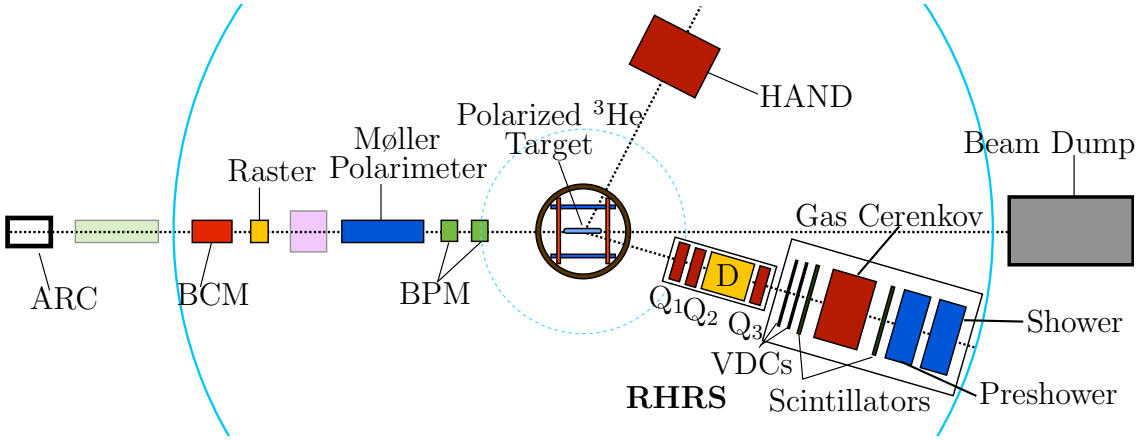

Fig. 3.4: Hall A Equipment used for ^{3}He$(e, e'n)$ Measurements

Parameter	Method	Accuracy	Comments
Energy	Arc	2×10^{-4}	Invasive
Energy	Arc	5×10^{-4}	Non-invasive
Energy Width	OTR	$\frac{\Delta E}{E} \approx 1 \times 10^{-5} (\sigma)$	Non-invasive
Current (≥ 1 μA)	2 RF Cavities	$\leq 5 \times 10^{-3}$	Non-invasive
Position (at target)	2 BPM/Harp	140 μm	x, y on line
Direction (at target)	2 BPM/Harp	30 μrad	θ, ϕ on line
Stability (at target)	Fast Feedback	$\leq$ 720 Hz motion	
Stability (at target)	Position	≤ 20 μm (σ)	
Stability (at target)	Energy	$\leq 1 \times 10^{-5}$ (σ)	
Polarization	Møller	$\frac{\Delta P}{P} \approx 2\%$	Invasive

Table 3.1: Methods to Determine Beam Parameters. This table contains an overview of the methods and equipment used to determine beam parameters. The Accuracy column is the width of an assumed Gaussian distribution. Techniques labeled "Invasive" require dedicated beam time and interrupt the main experiment.[22]

3.3.1.1 Arc

The energy of the beam is determined by measuring the deflection of the beam in the arc section of the beam-line and the field integral of eight dipole magnets. Nominally, the angle of the beam is 34.3°. A set of superharp wire scanners are used to determine the position of the incoming and outgoing beam and thus measure the angle. The integrated magnetic field of the eight quadruple magnets that the beam passes through in that bend is also measured. These are related to the beam momentum (and thus energy) by

$$p = k\frac{\int \vec{B} \cdot d\vec{l}}{\theta} \tag{3.1}$$

where $k = 0.299792 \frac{\text{GeV·rad}}{\text{T·m·c}}$ [22].

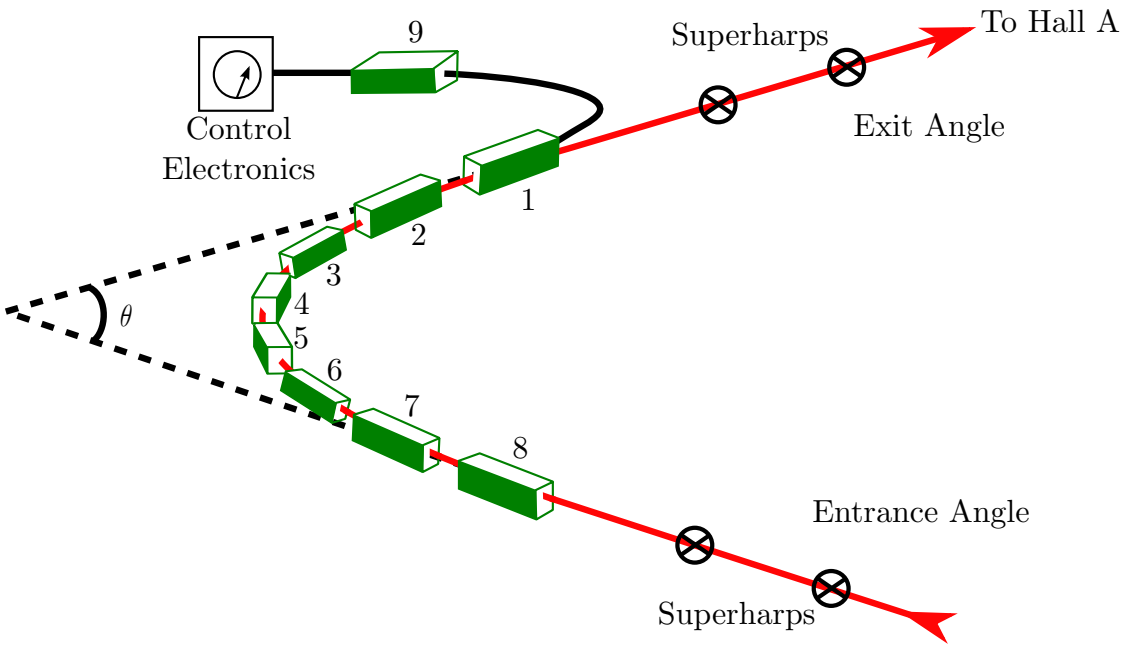

Fig. 3.5: Arc Layout. Displayed is the layout of the arc energy monitor which consists of 9 quadruple magnets, four superharp wire scanners, and control electronics.

3.3.1.2 Beam Current Monitors

Hall A's Beam Current Monitors (BCMs) consist of an Unser monitor and two RF cavities. They are located 25 m upstream of the target. They are calibrated against a cavity monitor and a Faraday Cup which are located at the injector of CEBAF. In order reduce noise and drift, the Unser monitor must have extensive magnetic shielding and the temperature must be stable. Due to drifts caused by having the beam running through the monitor over a time scale of minutes, it can't be used to continuously measure the beam current.

The RF cavities are stainless steel cylindrical high-Q waveguides tuned to the frequency of the beam (1.497 GHz) which provide output voltages that are proportional to the beam current. The output signals are doubled so that one provides a sampling and the other an integration. The sampling signal is recorded into the data stream approximately every 2-5 s. Each of the integration signals are sent into amplifiers of gains 1, 3, and 10 which extend the non-linear region at lower currents. Each of these integrated signals (three from each BCM) are recorded which allows for a measurement of the integrated charge during any given run[22].

3.3.1.3 Beam Raster

In order to prevent damage to the glass target cell, the beam was spread out through the use of quickly changing magnetic fields. This process is called rastering. Rastering also allows for a thinner glass wall on the target, which reduces background scattering. Typically, the raster size is a 2 mm $\times$ 2 mm square, as shown in Figure 3.6. The magnetic fields are provided by dipole magnets that are located 23 m upstream of the target.

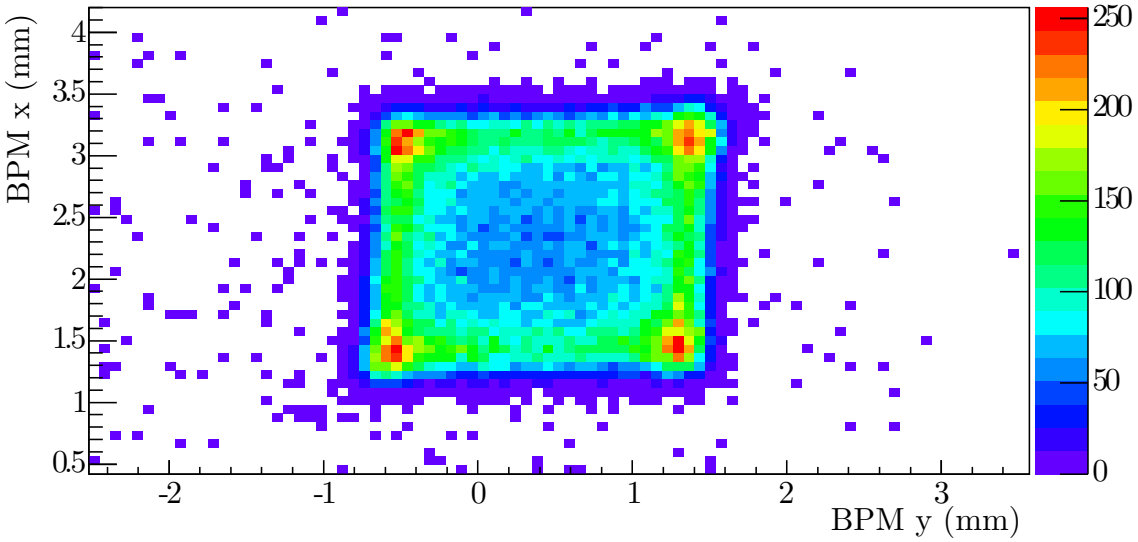

Fig. 3.6: Raster Example. Displayed is an example of the 2 mm × 2 mm raster used during the experiment. Data here is from Run 22487.

3.3.1.4 Beam Position Monitors

Two beam position monitors (BPMs) consisting of a 4-wire antenna array tuned to the fundamental RF frequency of the beam were used to determine the position and the direction of the electron beam on the target. They were placed 7.542 m and 1.286 m upstream of the target. The relative position of the beam is determined to within 100 μm for currents above 1 μA through the standard difference-over-sum technique[23]. The absolute position of the BPMs is calibrated through the use of superharp wire scanners located next to the BPMs. The averaged position over 0.3 seconds is logged into the EPICS datastream[22].

3.3.1.5 Møller Polarimeter

A Møller polarimeter was used to measure the polarization of the beam in Hall A. It measures a beam-target double-spin asymmetry from Møller scattering ($\vec{e^-} + \vec{e^-} \rightarrow e^- + e^-$) to extract the beam polarization. The polarimeter consists of a ferromagnetic foil target (which is magnetized in a magnetic field of about

24mT) as the source of the polarized electrons and a magnetic spectrometer. The spectrometer consists of three quadruple magnets, one dipole magnet, a steel collimator, and two arms of lead-glass calorimeters. The layout of the polarimeter is shown in Figure 3.7. The steel collimator is 6 cm thick and has a 2 cm radius hole which allows the scattered electrons through. The spectrometer detects scattered electrons in a kinematic range of $75^\circ < \theta_{CM} < 105^\circ$ and $-5^\circ < \phi_{CM} < 5^\circ$ where θ_{CM} is the azimuthal angle.[22] The Møller polarimeter is an invasive piece of equipment and requires dedicated beam time with runs taking approximately an hour. Measurements of the beam polarization can be found in Section 5.1.2.

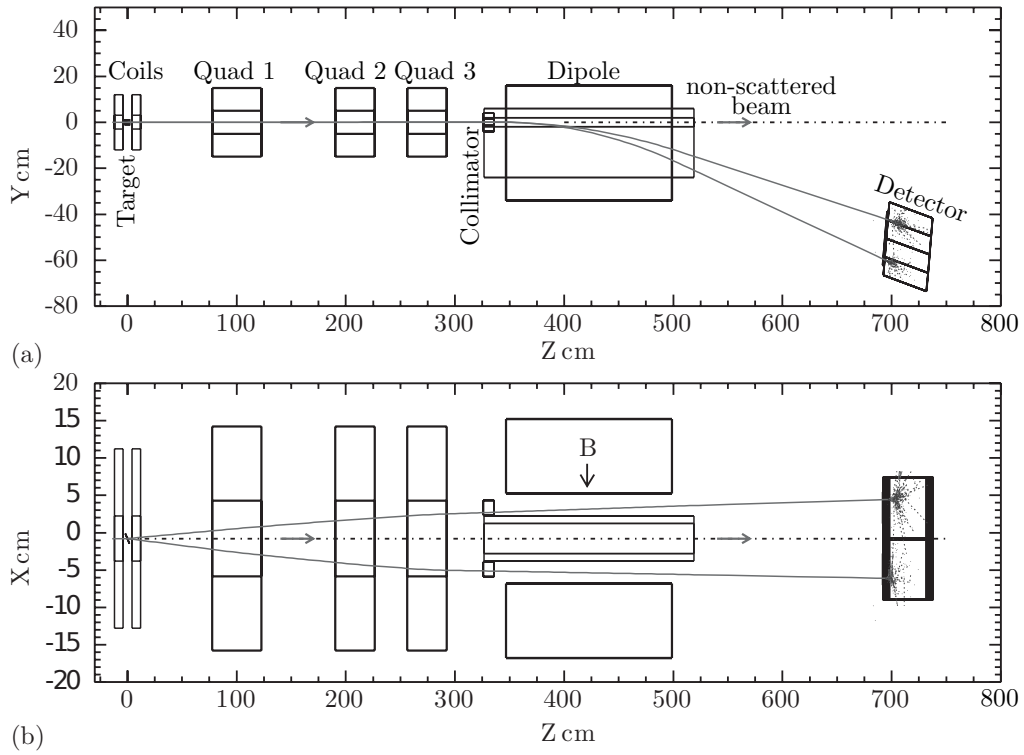

Fig. 3.7: Møller Polarimeter Layout. Displayed is the layout of the Møller polarimeter where (a) is a side view and (b) is a top view. The trajectories dispelled belong to a simulated event of Møller scattering at $\theta_{CM} = 80^\circ$ and $\phi_{CM} = 0^\circ$ at a beam energy of 4 GeV.[22]

3.3.2 Polarized ^{3}He Target

E05-102 and E08-005 would not have been possible if not for Hall A's polarized ^{3}He target system. Polarization of up to 60% was obtained through the use of a spin exchange and optical pumping (SEOP) cell. The target consists of glass cell which holds the He and alkali-metal vapor, a laser-based optical pumping to polarize the target, a series of Helmholtz coils to hold the polarization, an electron paramagnetic resonance (EPR) coil, and nuclear magnetic resonance (NMR) coils. The setup of the target system is shown in Figure 3.8. Target polarization of >50% was achieved for each of the three polarization directions. The different polarization directions are shown in Figure 3.9.

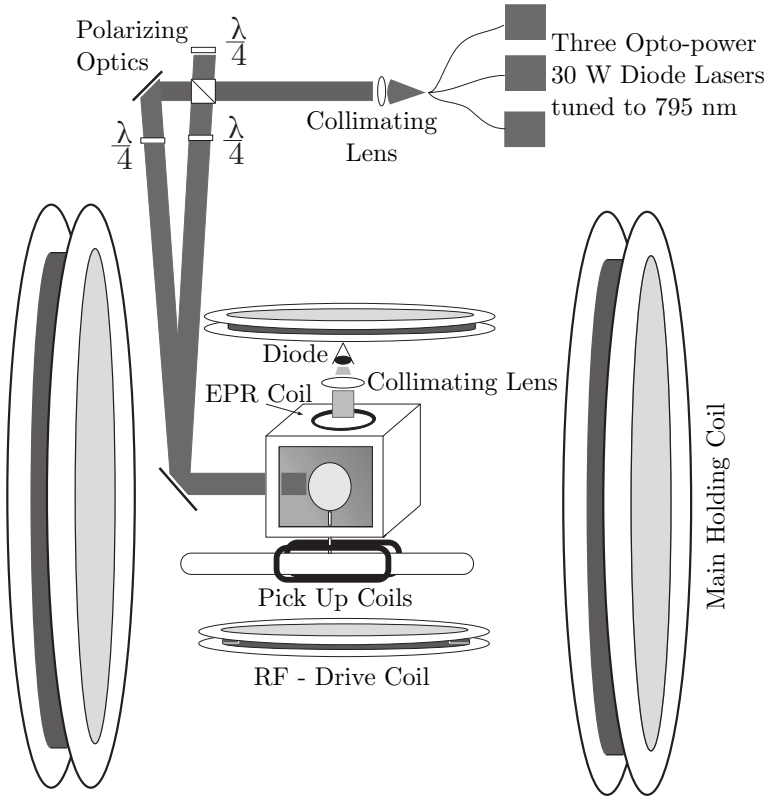

Fig. 3.8: Target System. This is a schematic of the target system. Not shown is a third set of Helmholtz holding coils which were placed orthogonal to each pair shown.

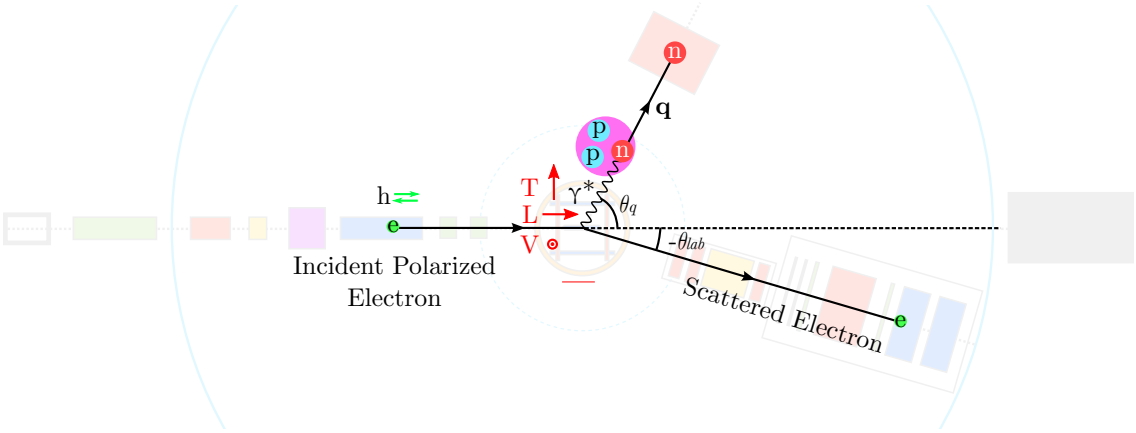

Fig. 3.9: Target Polarization Directions. The ^{3}He target used in this experiment was oriented in three orthogonal directions: transverse to both the beam and q-vector (Vertical, V), transverse to the beam and longitudinal with the q-vector (Transverse, T), and longitudinal with the scattered electron (Longitudinal, L).

3.3.2.1 Target Cell

The target cell is made up of a pumping chamber, a transfer tube, and a target chamber as shown in Figure 3.10. It contains ^{3}He pressurized to about 0.69 MPa. The pumping chamber is where polarization of the ^{3}He occurs through optically-pumped spin-exchange.The particular type of cell used was a RbK hybrid cell. Circularly polarized laser light excited the Rb atoms which collide and exchange spin with both ^{3}He and K atoms. The now-polarized K atoms will also collide with ^{3}He atoms and cause the ^{3}He to polarize. The second process helps to reduce the time needed for the total of the target to be polarized[22]. A diagram of these processes is shown in Figure 3.11. The target chamber is a 40 cm long tube where the beam passes through. Two cells were used for these experiments: "Dominic" when the target was polarized vertically, and "Moss" when the target was polarized longitudinally and transversely. The glass walls of each had a thickness of <1.7 mm and a window thickness of <0.16 mm.

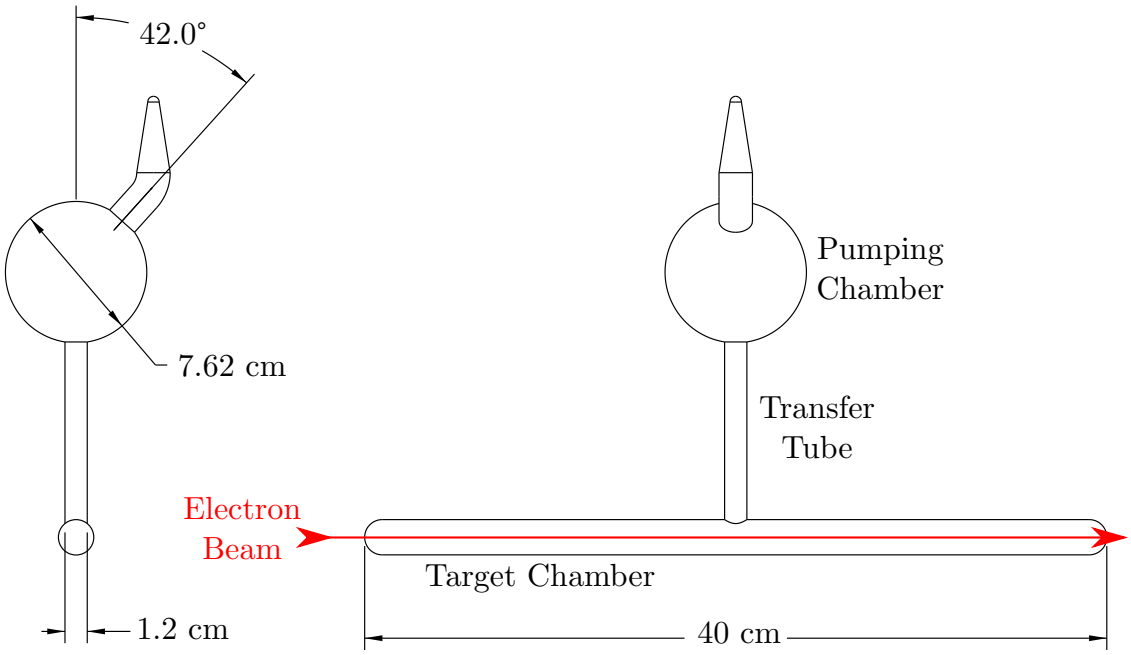

Fig. 3.10: Target Cell. This schematic of the target cell shows the pumping chamber, transfer tube, and target chamber. All measurements are design specifications and may have been adjusted slightly in production.

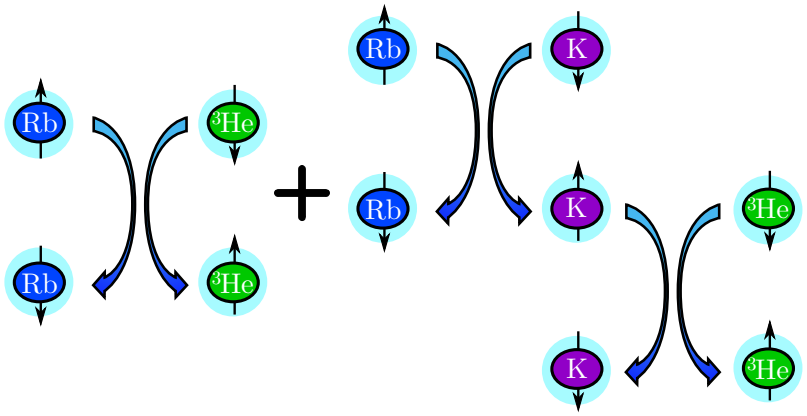

Fig. 3.11: Spin Exchange Processes. This cartoon shows the spin exchange processes of Rb, K, and ^{3}He.

3.3.2.2 Optical Pumping System

A laser system capable of producing approximately 50 W of light at 795 nm was used to induce polarization in the Rb mixture. It consisted of three 30 W diode lasers. The light was routed via fiber optics and polarizing optics to the pumping chamber of the target cell. The laser light was polarized through the use of a polarizing beam splitter, which polarized the beam linearly, followed by a quarter-wave plate which polarized the light circularly. The polarization of the light was able to be reversed through through the use of an insertable half-wave plate, which combined with reserving the direction of the holding field would reverse the direction of ^{3}He polarization[22].

3.3.2.3 NMR and EPR

Two systems were used to measure the polarization of the target: nuclear magnetic resonance (NMR) and electron paramagnetic resonance (EPR). The ^{3}He NMR signal was calibrated against that a water cell through the technique of adiabatic fast passage (AFP) to find the polarization. NMR signals were recorded every four hours throughout the experiment. They were cross checked with EPR measurements of Rb atoms to determine the polarization of the target. There were 15 EPR measurements taken over the entire run period.

3.3.3 High Resolution Spectrometer

Jefferson Lab's Hall A has two primary detectors called the Left and Right High Resolution Spectrometers (LHRS and RHRS, respectively). The ^{3}He$(e, e'n)$ channel used in the measurements in this thesis only used the RHRS. The detector consisted of three quadruple magnets, one dipole magnet, and a detector package.

The detector package for this experiment consisted of two multi-wire vertical drift chambers (VDCs), two trigger scintillators (S1 and S2), a gas **C**erenkov detector, and two planes of lead glass calorimeters (Preshower and Shower). The layout of each of these is shown in Figure 3.12.

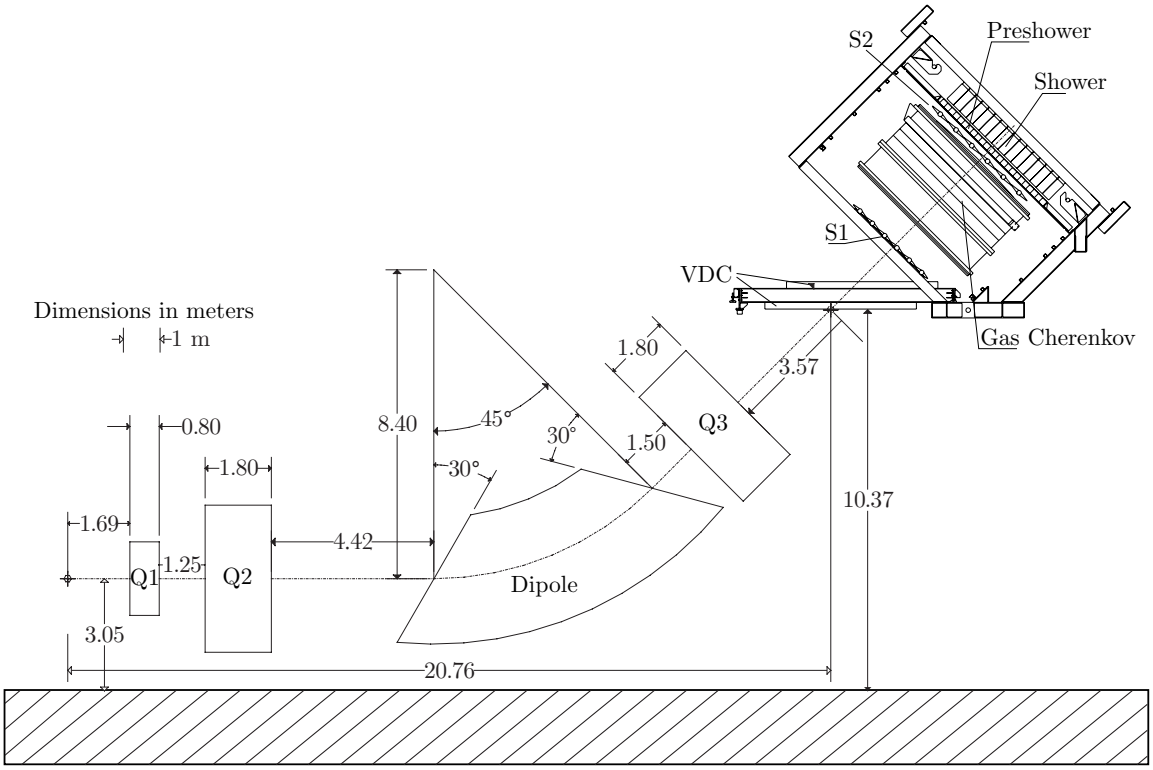

Fig. 3.12: RHRS Layout. This shows the placement of the detectors inside of the right High Resolution Spectrometer.

3.3.3.1 Vertical Drift Chambers

The RHRS has two planes of vertical drift chambers (VDCs) which measure the position and angle of incidence of recoiled electrons to within ± 125 μm. Each VDC consists of two orthogonal planes of wires held at a high voltage and immersed in a bath of gaseous argon and ethane. As charged particles travel through the gas, it becomes ionized and is attracted to the wire planes. Upon collision with the wires,

a signal pulse is generated which is recorded using multi-hit TDCs. Each VDC has a 2118 mm × 288 mm active area. The geometry of the VDCs is shown in Figure 3.13.

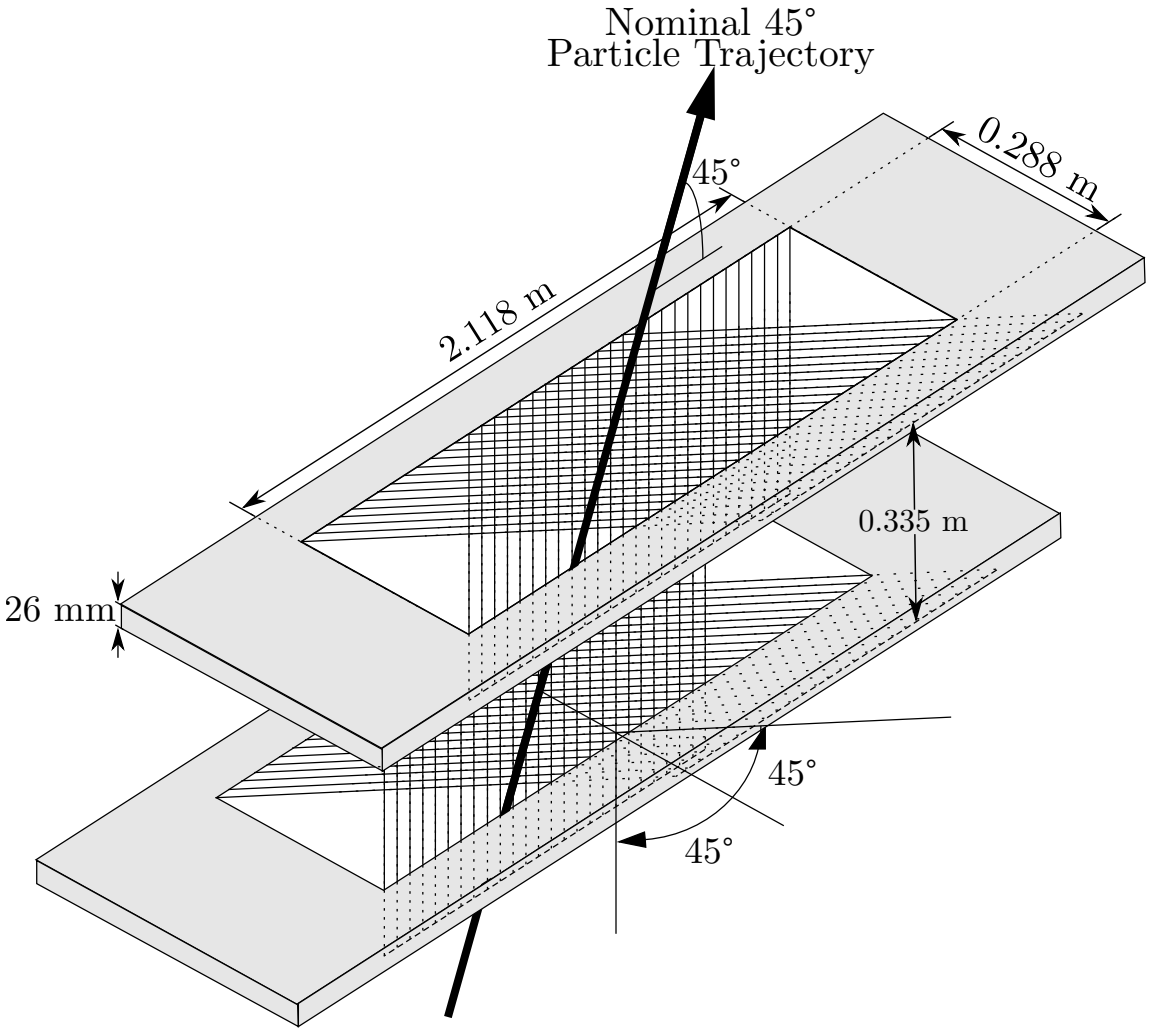

Fig. 3.13: VDC Relative Geometry. This schematic shows the relative angles and distances of the VDCs with respect to each other. Each VDC contains an upper (V) and lower (U) plane of wires that orthogonal to each other. The wire planes from their matching plane ($U_{top} \leftrightarrow U_{bottom}$, $V_{top} \leftrightarrow V_{bottom}$) by 0.335 m. This figure is adapted from [24] and is not to scale.

3.3.3.2 Trigger Scintillators

Two planes of thin plastic scintillators were used as triggers in the RHRS. Each plane has six overlapping, 5 mm-thick paddles. The planes are separated by 2 m and have a time resolution of 0.30 ns. Every individual paddle records a possible event when there is a coincidence between the two photomultiplier tubes (PMTs) on that paddle. If the event is picked up in both the front scintillator (S1) and the rear scintillator (S2), then the event is recorded[22]. Details of the trigger electronics is shown in Figure 3.14.

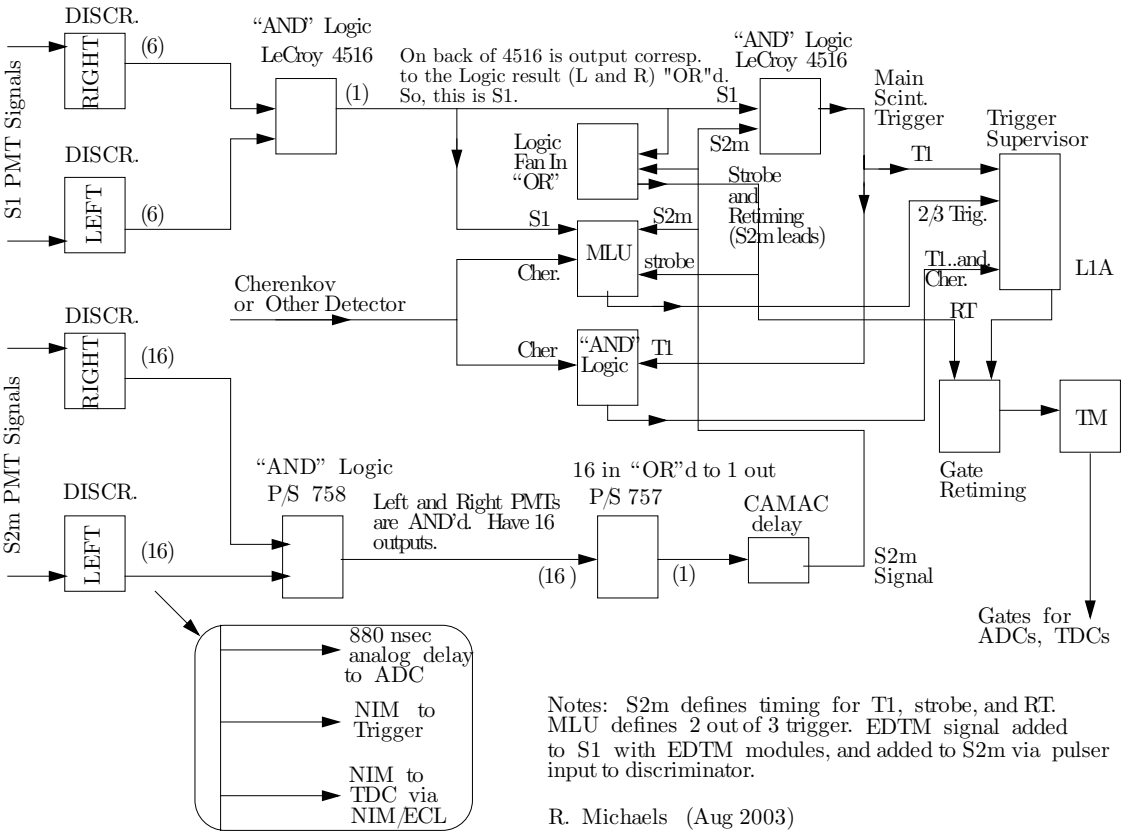

Fig. 3.14: HRS Trigger Scheme. This diagram maps out the trigger scheme for the RHRS spectrometer. Signals from the trigger scintillators enter on the left, and the output on the right is a gate that the ADCs and TDCs of the other equipment use.

3.3.3.3 Gas Cerenkov

A CO_2-filled gas **C**erenkov detector is used to separate pions from electrons. It is positioned between the S1 and S2 scintillator planes. It has a particle path of 130 cm and consists of 10 spherical mirrors of 80 cm focal length which are each focused on a PMT.

When high-speed particles travel through the gas, they are traveling faster than light can through the CO_2. As they progress through the CO_2, they give off luminous energy through a process akin to sonic booms, only for light. The radiated light, known as **C**erenkov radiation, is collected and recorded. Since electrons are lighter than pions, it is easier to accelerate them to velocities required for **C**erenkov radiation to occur. A cut made separating slower particles from faster ones, but cutting on a small channel of the **C**erenkov detector, easily distinguishes between pions and electrons as is discussed in detail in Section 4.1.2.

3.3.3.4 Electromagnetic Calorimeters

The RHRS contains two layers of electromagnetic calorimeters called the "preshower" and "shower" detectors. They are made out of lead glass blocks attached to photomultiplier tubes. Particles can be identified by how much energy they deposit in preshower compared to the shower. This allows a separation of electrons from hadrons. A schematic of the calorimeters is shown in Figure 3.15.

Name	# of Blocks	Cols	Rows	X (cm)	Y (cm)	Z (cm)
Preshower	48	2	24	10.0	35.0	10.0
Shower	75	5	15	15.0	15.0	32.5

Table 3.2: This table contains the number and dimensions of lead glass blocks used in the Preshower and Shower detectors. "X" denotes the dispersive plane, "Z" is along the average particle direction, and "Y" is parallel to the focal plane.

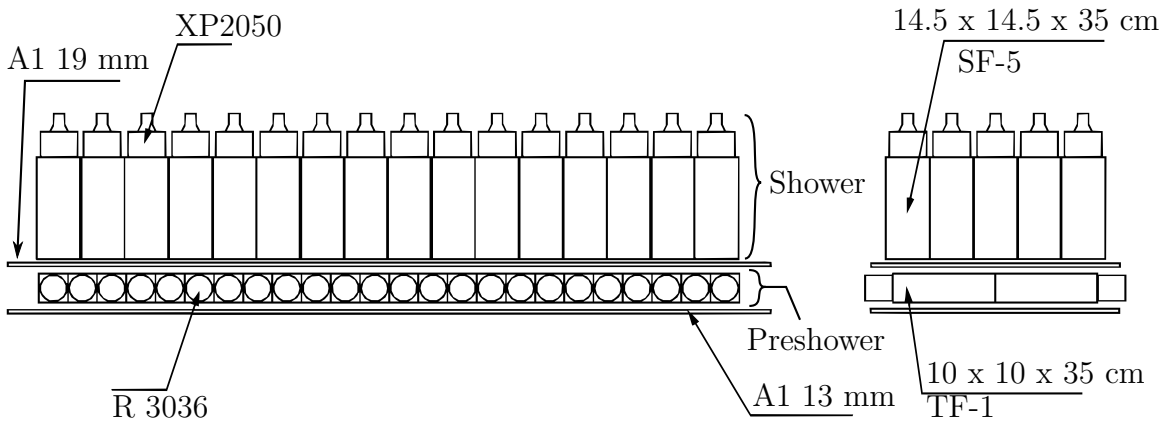

Fig. 3.15: Shower and Preshower Layout. This shows the schematics for the shower and pre shower lead glass blocks used in the RHRS.

3.3.4 Hall A Neutron Detector

The Hall A Neutron Detector (HAND) consists of an array of plastic scintillators connected to photomultiplier tubes (PMTs). Timing information is read out through Time-to-Digital Converters (TDCs) for each PMT. HAND is made of 88 main detecting bars arranged in four layers. The thickness of each bar in these layers is 10 cm, the length is 100 cm, and the height varies with the smaller bars placed in front of the larger bars. There is also a thinner veto layer that contains 64 bars with dimensions of 2 x 11 x 70 cm^3. The layout of these bars can be seen in Figure 3.16.

Since neutrons do not carry charge, they are not directly measured by the scintillator; however they sometimes will knock a proton out of H atoms in the plastic scintillating detectors. The scattered proton then radiates light in the scintillator which is detected. This process occurs over a distance of approximately 10 cm. Since protons and neutrons are similar in mass, protons scattered from ^{3}He will arrive at the detector at approximately the same time as neutrons. In order to separate neutrons from protons, a series of veto cuts are made in post-analysis which exclude

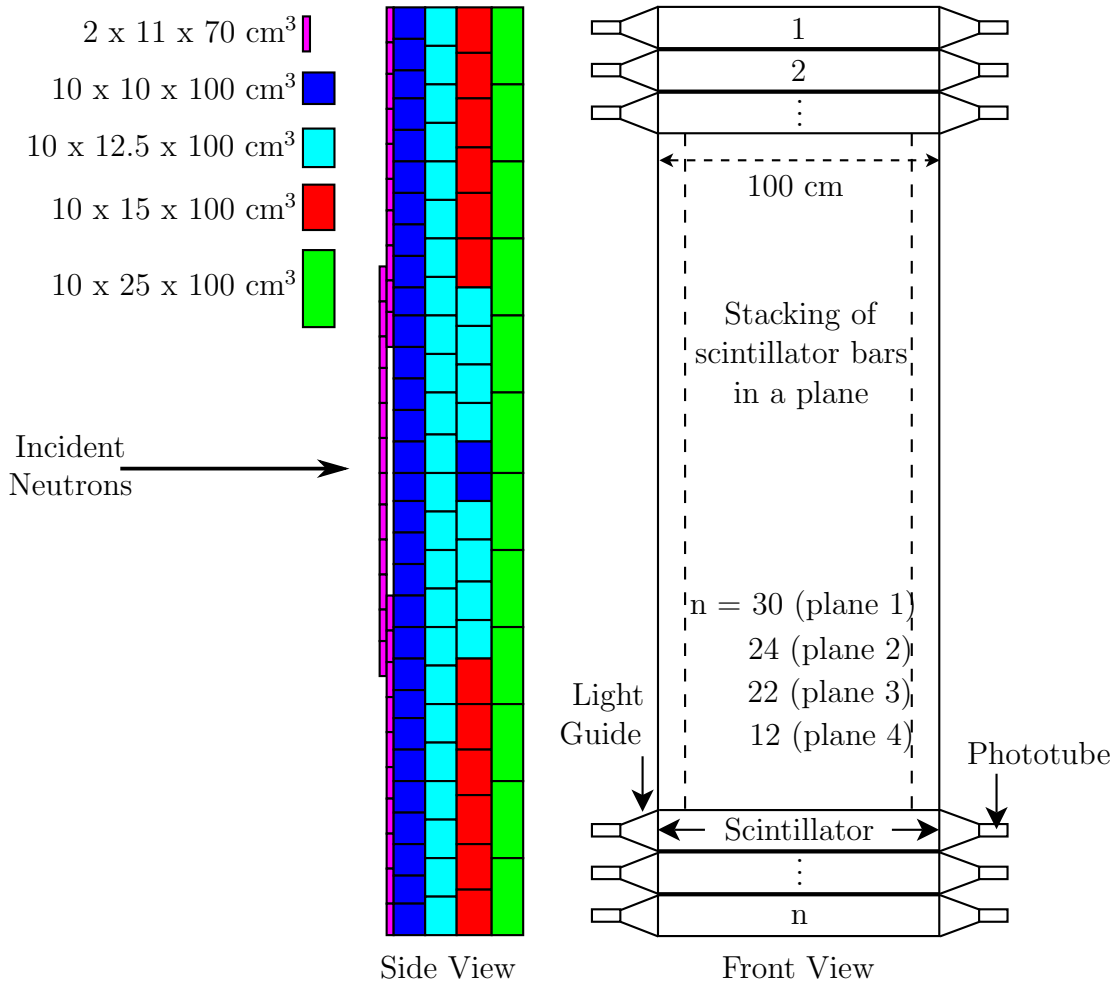

Fig. 3.16: HAND Layout. This shows the arrangement of the scintillator bars in the Hall A Neutron Detector.

events picked up by bars in front of any given bar within the timing window for both protons and neutrons. In particular, a proton will always deposit a signal in the 2 cm thick veto bars whereas a neutron will most likely pass through the thin veto counter without interacting. In addition, at higher scattering energies a 9.08 cm thick lead wall, made up of 4 cm of iron casing surrounding the 5.08 cm thick lead, was placed in front of HAND that helps to reduce the number of protons that make it to the detector.

3.4 Kinematics

In order to map out the quasi-elastic scattering region, the detectors mentioned in the previous sections were placed at different angles, energy settings, and target polarization directions. A listing of each of these kinematics settings is found in Table 3.3. A negative angle corresponds to a component which placed to the right of the beam line where a positive angle to one placed to the left of the beam line. A 0° angle corresponds to directly downstream of the target.

Target Pol.	E_0 (GeV)	RHRS (°)	RHRS P_0 (GeV)	HAND (°)
Vertical	1.245	-17.0	1.1759	71.0
Vertical	2.425	-17.0	2.1813	62.5
Vertical	3.605	-17.0	3.0855	54.0
Longitudinal	2.425	-16.0	2.2500	62.5
Longitudinal	2.425	-16.0	2.2250	62.5
Longitudinal	2.425	-18.0	2.1750	62.5
Longitudinal	2.425	-18.0	1.8650	62.5
Longitudinal	2.425	-18.0	0.7000	54.0
Longitudinal	2.425	-18.0	2.0250	54.0
Longitudinal	3.606	-17.0	3.0855	54.0
Transverse	2.425	-16.0	2.2250	62.5
Transverse	2.425	-18.0	2.1750	62.5
Transverse	2.425	-18.0	1.8500	62.5
Transverse	3.606	-17.0	3.0855	54.0

Table 3.3: This table contains the kinematics settings for the Quasi-Elastic family of experiments. Every line corresponds to a change in the kinematics during the experiments. This includes, respectively, the beam energy (E_0), the right HRS central angle, the right HRS central momentum (P_0), the Hall A Neutron Detector (HAND) central angle, and the target polarization direction. Please see Figure 1.3 for definitions of the polarization directions.

Chapter 4

Particle Identification

As mentioned in Chapter 3, for this experiment the right High Resolution Spectrometer (RHRS) was used to detect electrons scattered from polarized ^{3}He and the Hall A Neutron Detector (HAND) was used to detect knocked-out neutrons. This chapter will discuss the analysis that went in to identifying these particles.

4.1 Electron Identification

The RHRS was used to identify electrons that were quasi-elastically scattered from the ^{3}He nuclei. The HRS contains a gas **C**erekov detector and two electromagnetic calorimeters, called the preshower and shower, that were used to differentiate between pions and electrons. The VDCs provided tracking information that was used to isolate electrons aimed along a q-vector towards HAND. They were also used to isolate events scattered from ^{3}He from those scattered off of the glass wall of the target cell. Combinations of these detectors were used to find the quasi-elastic scattering peak and to separate it from the elastic scattering peak. Details of the electron cuts are discussed below.

4.1.1 HRS Optics

In order to separate particles for identification within the high resolution spectrometer, the optics must be calibrated. This was done using a sieve collimator and a multi-foil carbon target.

The multi-foil carbon target was used to trace particles back to the origin of their scattering. It was needed because the ^{3}He target consists of an extended, 40 cm-long chamber instead of a point target. In order to account for the long target, events were traced back to each of the carbon foils in the calibration of reconstruction matrix. The foil target was made of multiple point targets placed at intervals of approximately 6.67 cm. This is shown in Figure 4.1.

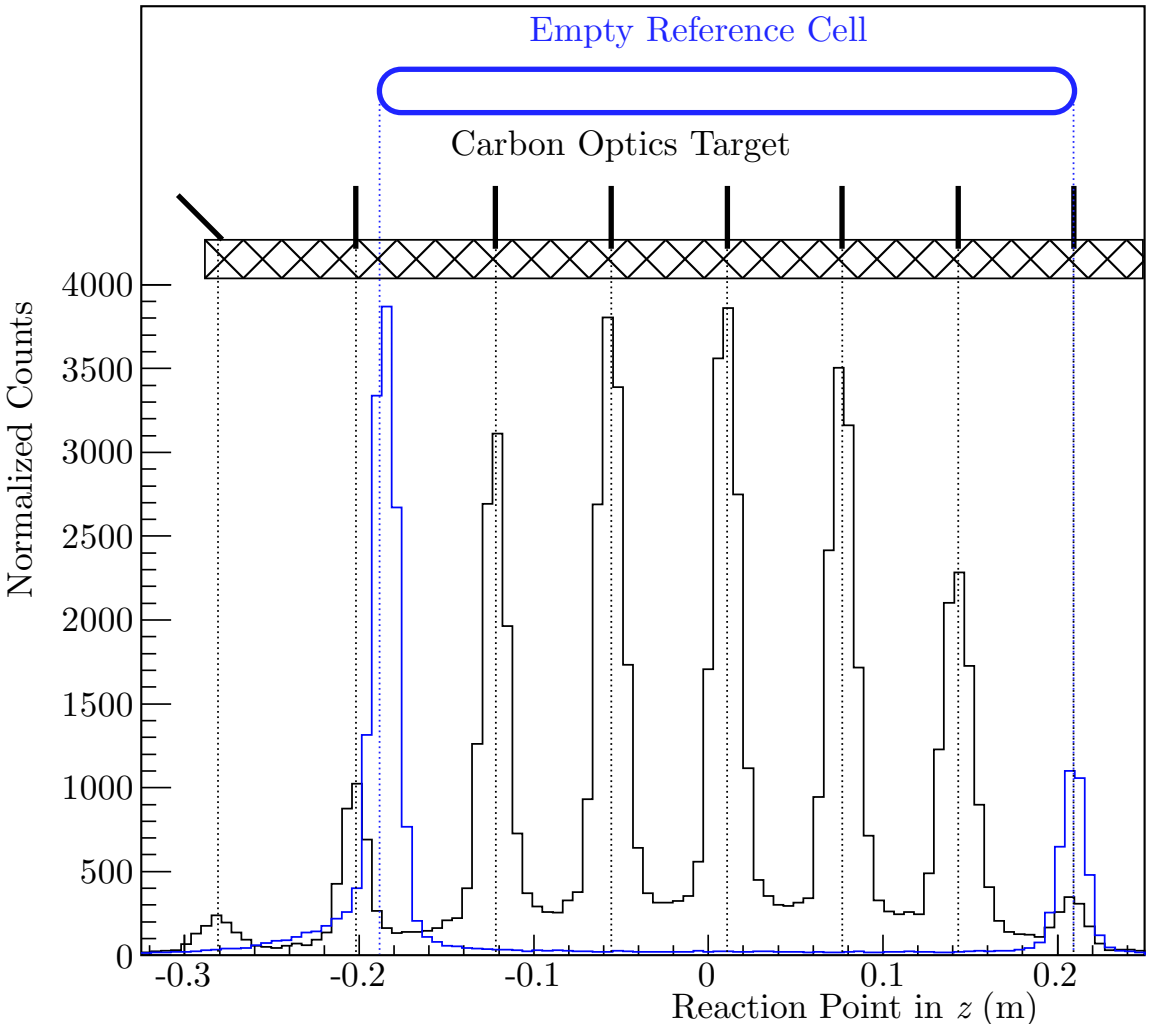

Fig. 4.1: RHRS Extended Target Optics. This plot shows the calibration of the 40cm target cell via the use of a carbon multi-foil target. Note that one of the carbon foils was misplaced by a few centimeters, which is displayed towards the left. There was also a small BeO foil shown slanted.

A stainless steel sieve was used to calibrate the trajectory of a particle (θ_{tg} and ϕ_{tg}). The sieve is a sheet of steel with a pattern of 49 holes (7 x 7) that have a radius of 1 mm and are spaced 25 mm apart vertically and 12.5 mm apart horizontally. Two of the holes have a radius of 2 mm and are placed asymmetrically in the pattern so that orientation is easily identified. A diagram of the sieve pattern is shown in Figure 4.2.

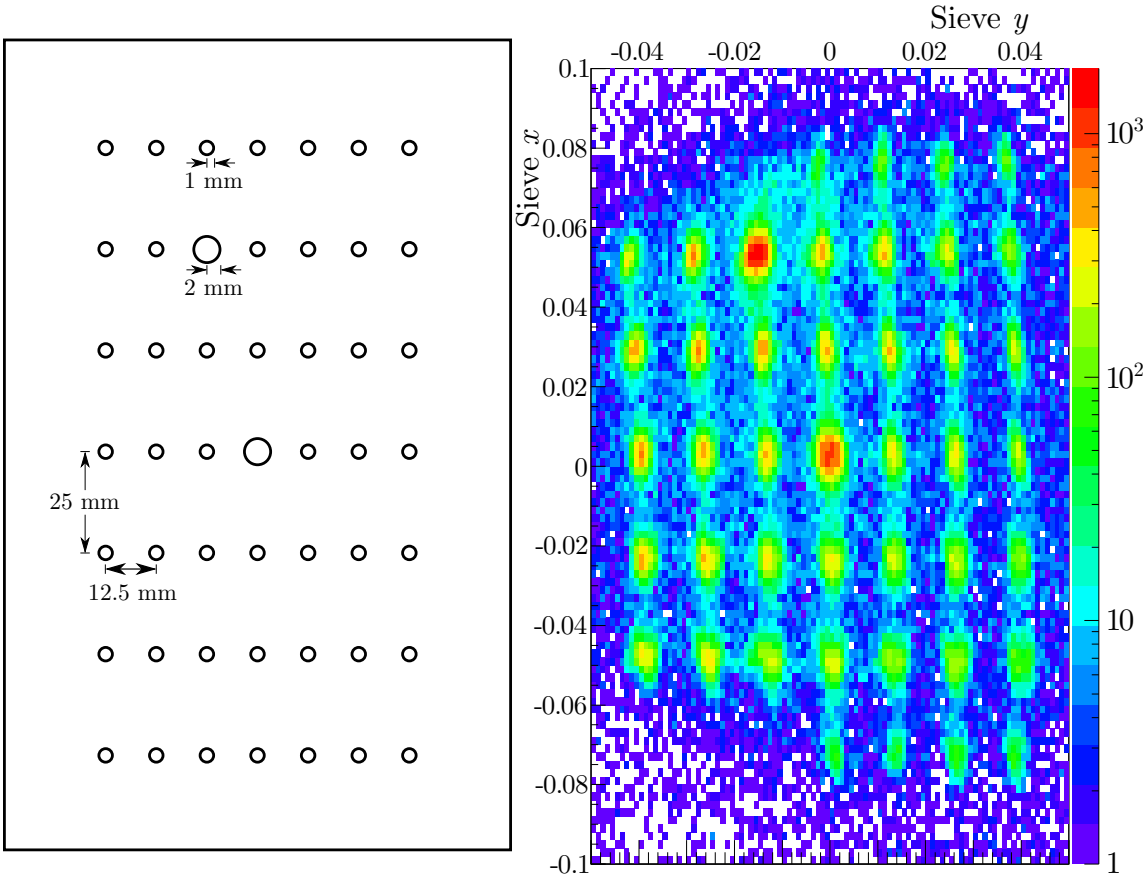

Fig. 4.2: Sieve Pattern. The schematic on the left shows the orientation of the sieve pattern used to calibrate the RHRS. The plot on the right shows data with the sieve plate in after calibration was completed.

By using both the sieve pattern and the multi-foil carbon target, events were able to be calibrated to two known positions. The calibration of the reaction point in z as well as for θ_{tg} and ϕ_{tg} was completed by Jin Ge [20].

4.1.2 Pion Contamination

in order to separate pions from electrons, the gas **C**erenkov, Preshower, and Shower detectors were used. Pions appear in the output of the **C**erenkov detector as a large, sharp peak around channel 0, where electrons appear as a much wider peak at channels above 100. This can be seen in Figure 4.3.

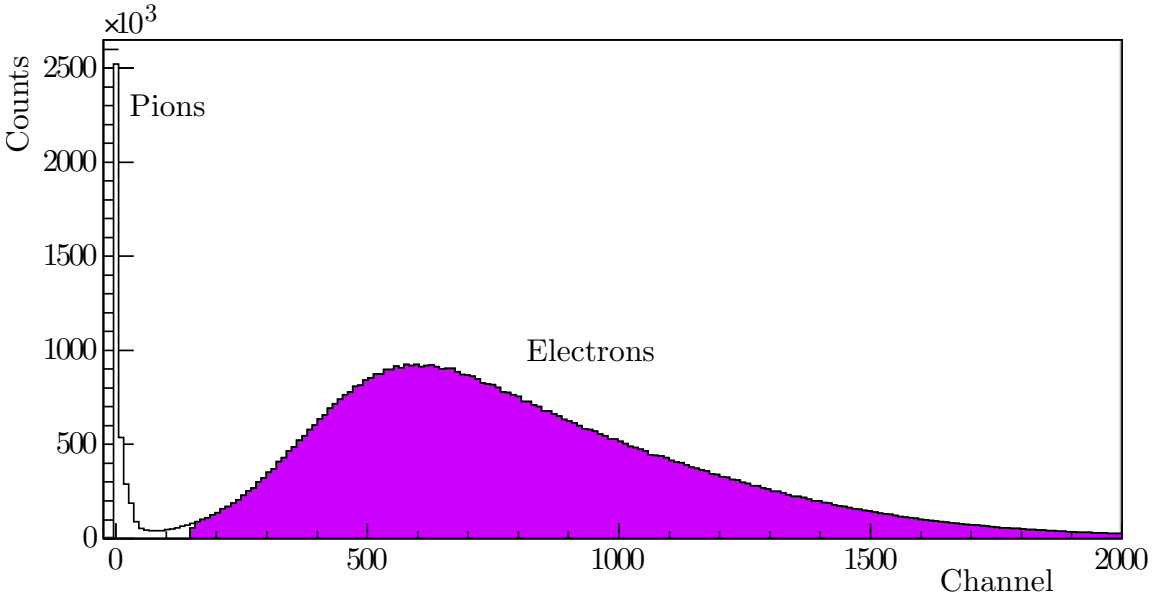

Fig. 4.3: **C**erenkov Pion Cut. The separation of pions from electrons was done through the use of a cut on the gas **C**erenkov detector.

In addition, the Preshower and Shower detectors were used as secondary measure to separate pions from electrons. There is a clear pion peak and electron peak which can be seen in Figure 4.4. A linear cut was made between the peaks and only those on the electron side were kept.

4.1.3 Glass Wall Contamination

Through the use of tracking variables, the point of scattering along the z-direction is able to be determined. From this, it becomes clear that there is a distinction between the ^{3}He scattered events and those events that are scattered off

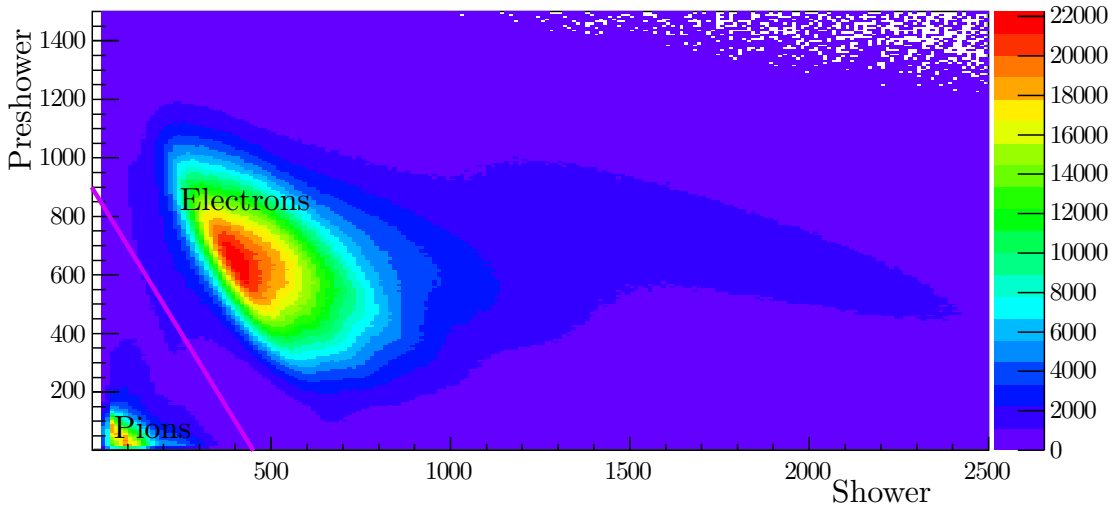

Fig. 4.4: Preshower-Shower Pion Cut. The separation of pions from electrons was done through the use of a cut on the lead glass calorimeters.

of the glass end walls of the target cell. In order to remove events scattered from the walls a cut was made 3.7 sigma away from the central value of the upstream wall peak and 3 sigma away from the downstream wall peak. The larger cut was made on the upstream side since the magnitude of the peak is much larger than for the downstream side, a trend that becomes more important as the beam energy is increase. The cuts on ^{3}He events can be seen in Figure 4.5.

4.1.4 Elastic and Quasi-Elastic Peaks

There are two energy peaks caused by different types of scattering off of ^{3}He: the elastic peak, where the whole ^{3}He nucleus is scattered by the incoming electron, and the quasi-elastic peak, where a single nucleon is scattered out of the ^{3}He by the electron. The contribution of elastic events decreases as the energy of the beam was increased, but it was especially important to take the elastic peak into account for the Q^2=0.1 (GeV/c)^2 data. The $x_{Bjorken}$ variable is ideal for differentiating between

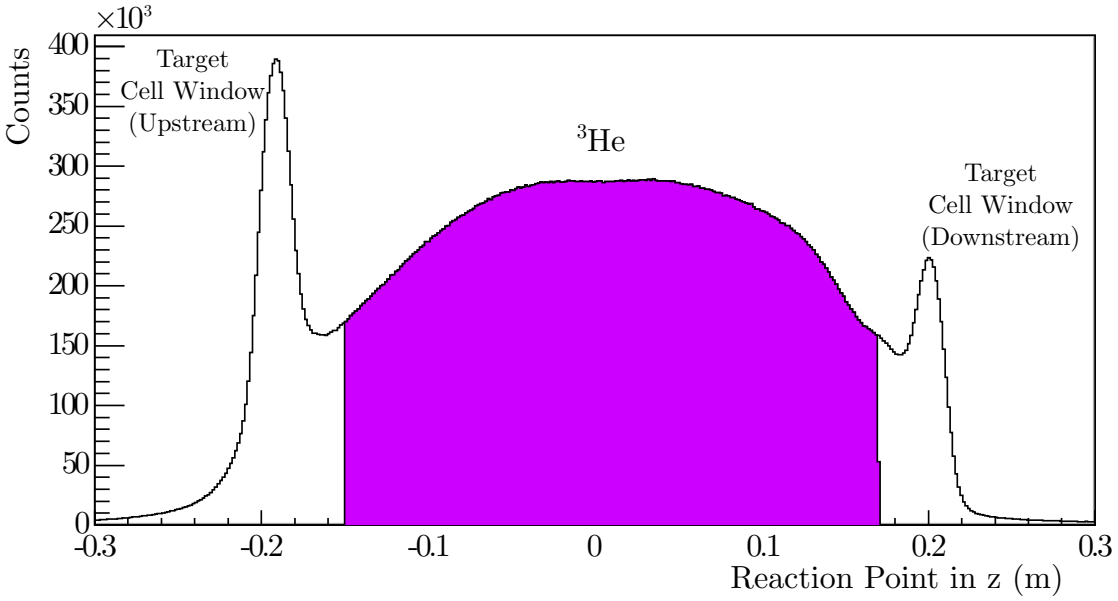

Fig. 4.5: Reaction Point in z Cut. Separation of ^{3}He events from glass wall events was achieved by making a cut on the reaction point in z.

these peaks. It is defined as

$$x_{Bjorken} = \frac{Q^2}{m\nu} \tag{4.1}$$

where Q^2 is the momentum transfer squared, m is the average mass of a nucleon, and ν is momentum transfer. Due to its relationship with the momentum transfer and mass, a naive interpretation of the variable is that is shows how many nucleons are expelled during a collision.

In order ensure that there was no contamination from the elastic peak, especially for the lowest Q^2 point, a fit was made on the elastic peak in Bjorken-x as shown in Figure 4.6. When the elastic peak was removed, as shown in Figure 4.9, it left behind only those events that were quasi-elastically scattered. This can be further seen in the nu plot shown in Figure 4.8.

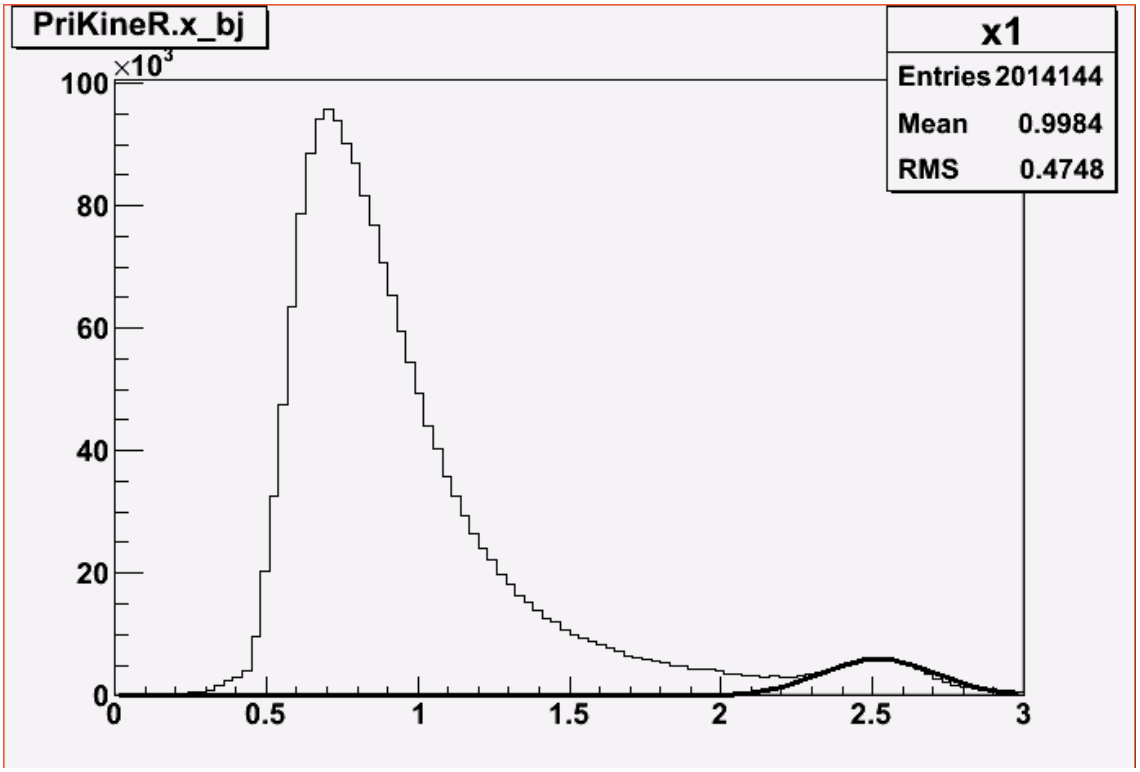

Fig. 4.6: Elastic Peak on Bjorken-x. This figure shows a fit on the elastic peak in Bjorken-x. As shown in Figure 4.9, a cut was made that eliminated elastic events from the dataset.

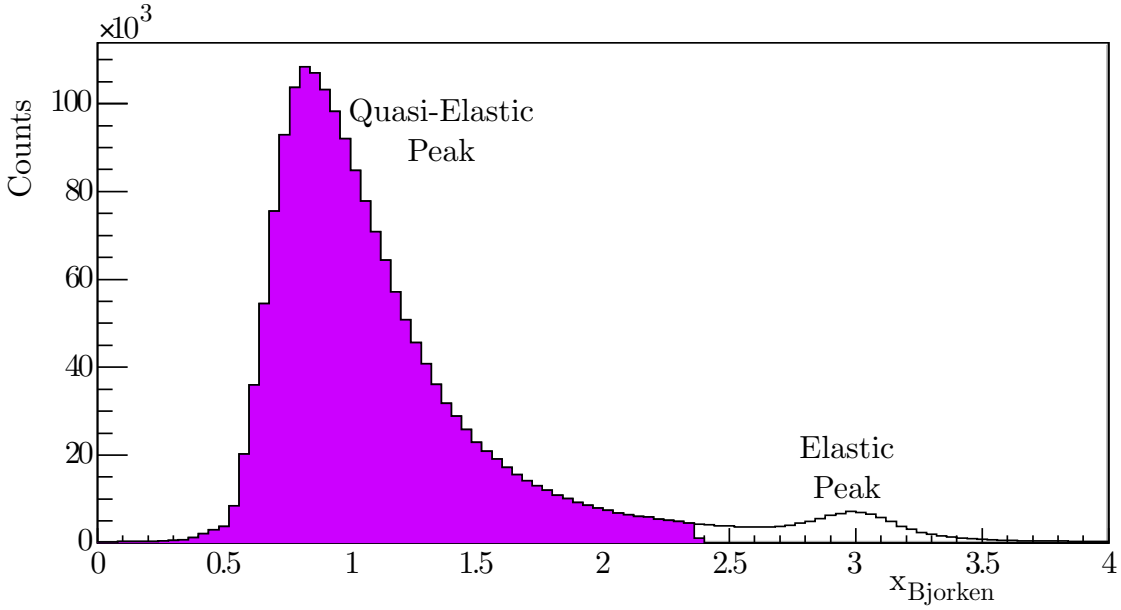

Fig. 4.7: Bjorken-x Cut. The separation of the quasi-elastic from the elastic peak was made by using a cut on Bjorken-x.

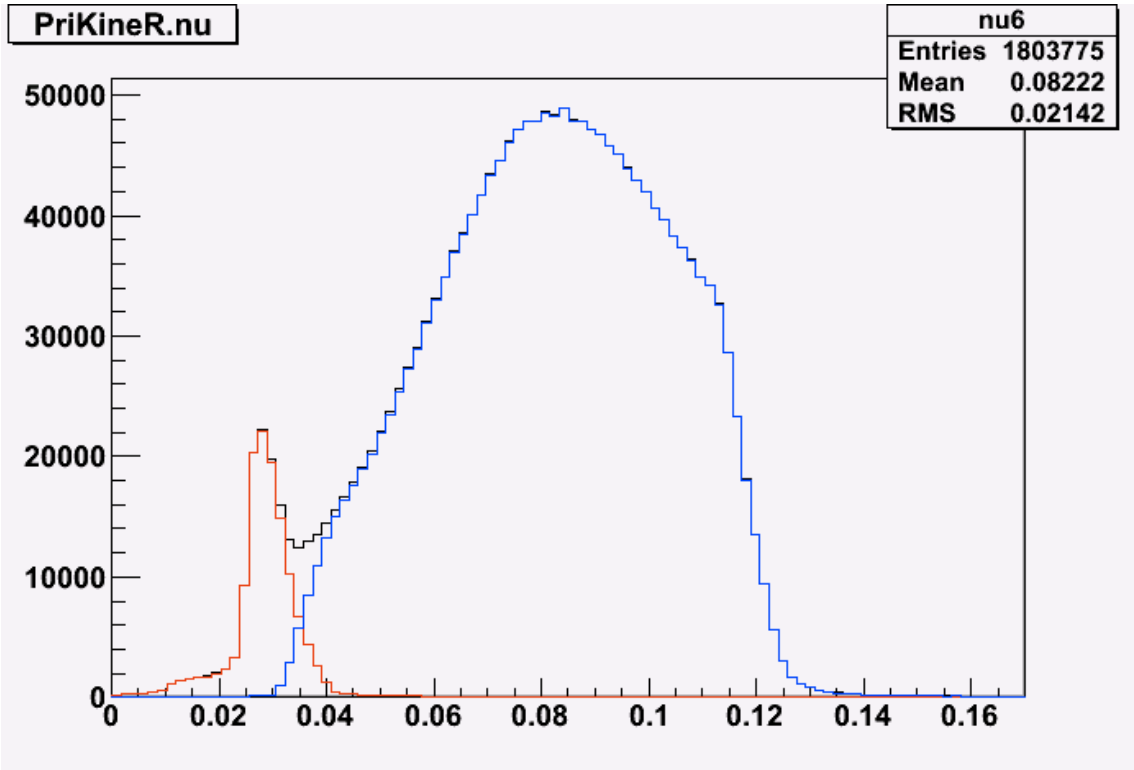

Fig. 4.8: Effect of Bjorken-x cut on dp. This figure shows which events were kept and which were discarded from dp when the cut on Bjorken-x was made. The red events were removed while the blue ones were included in the dataset. The black line shows the total events.

4.1.5 Events Along q-vector

The RHRS has an angular acceptance of approximately 7 msr. Scattered electrons were kept if they fit within this acceptance. This is allowed for an accurate measurement to be made of the correlated knocked-out neutrons in HAND.

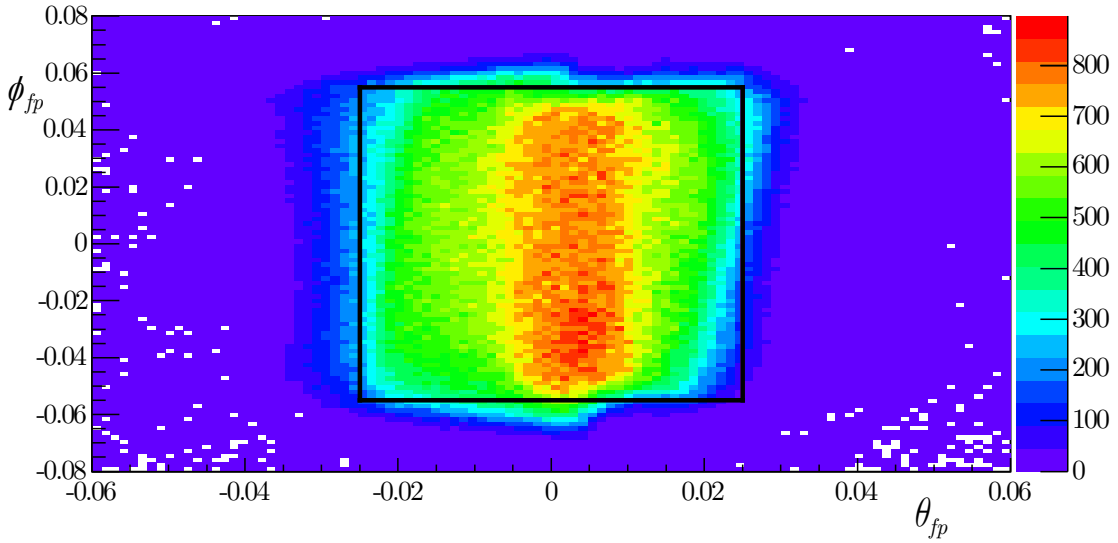

Fig. 4.9: $\theta : \phi$ Cut. Events along the q-vector were selected based on θ and ϕ in the focal plane Selected events are enclosed in the black square.

4.2 Neutron Identification

4.2.1 Neutron Selection via Veto bars

As discussed in Section 3.3.4, the scintillators that make up HAND cannot directly detect neutrons. Instead, they detect knocked-out protons. Another complication is that knocked-out protons, having approximately the same mass as neutrons, will reach HAND in the same timing window. In order to differentiate between the two, a series of "veto" bars were used. When a neutron enters HAND, it is not detected in a scintillator bar until it knocks out a proton. This means that if there is a signal located in one bar, but not in any of the bars in front of it, then the

signal comes from a neutron. If instead, there is a signal in a bar and signals in the bars in front of it, then it is a proton. Although protons and neutrons come in the same timing peak, the TDCs of HAND were used to discriminate between protons an neutrons. This was done by excluding events appearing in the timing window of the veto bars that corresponds to the timing of neutrons or protons. An example is shown in Figure 4.10.

4.2.2 Time of Flight

Through the use of veto bars, it is possible to separate protons from neutrons in the TDC timing peaks. However, there are a number of other background events that also need to be removed to select only neutrons. These background events come from processes such as ^{3}He(e, e'), dark noise in the PMTs, and other sources; and appear as a broad background in time. In order to separate them out, the time of flight (ToF) was used.

In the case of Q^2=0.13, this was accomplished by a simple exponential fit on the background. This allowed the neutron peak to be isolated and the number of events to in it to be counted. This is shown in Figure 4.11. The higher Q^2 points were slightly more complicated. The background for those points were linear, however there is a difference in the magnitude on either side of the neutron peak. In order to account for this, a linear fit was made under the neutron peak to bridge the gap between the constant background on either side. This is shown in Figures 4.12 and 4.13. The uncertainty due to background subtraction is discussed in more detail in Section 5.4.

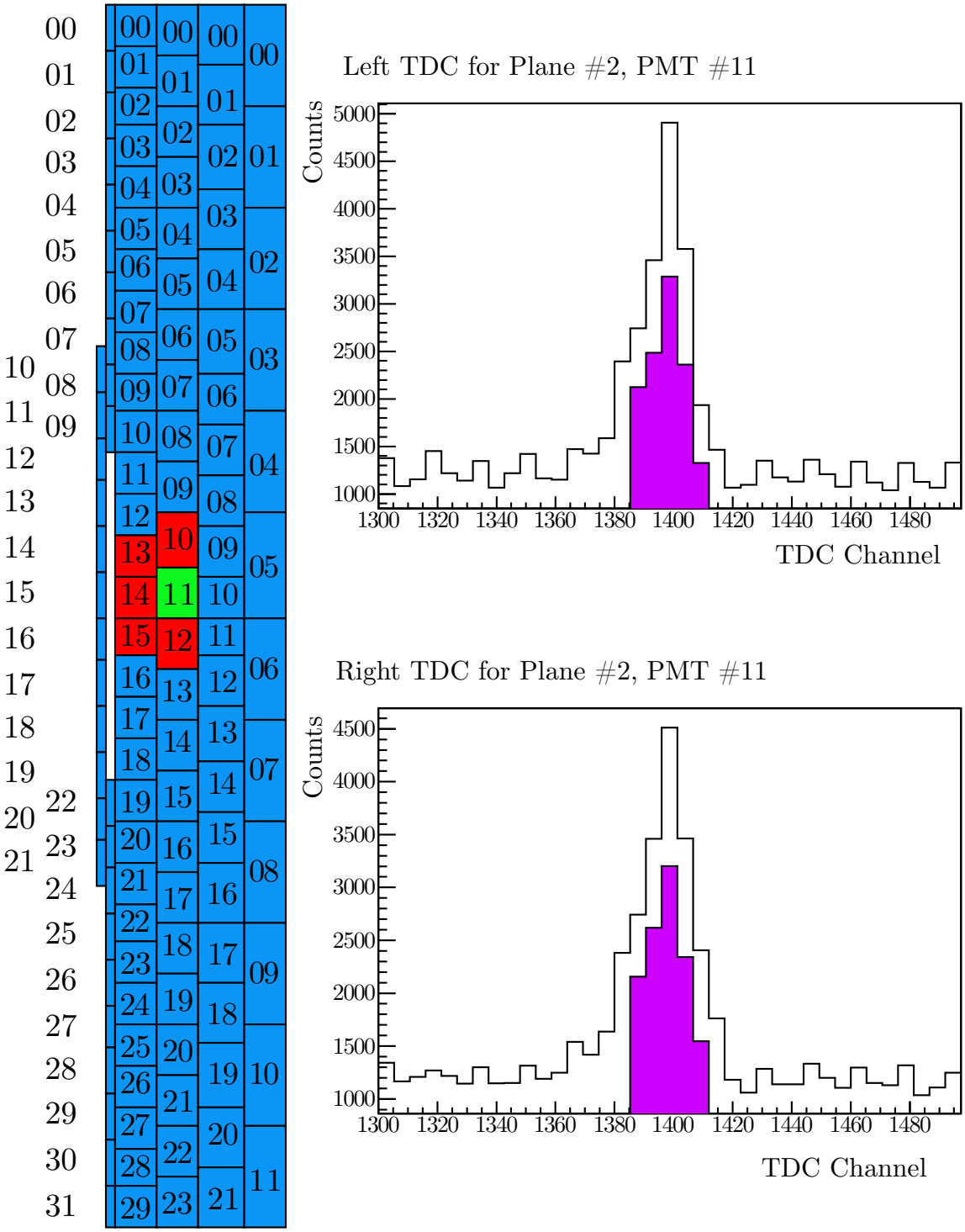

Fig. 4.10: HAND Veto Example. For each bar in HAND, the bars in front of, above, and below were identified as "veto" bars to isolate neutrons from protons. For example, Plane 2 Bar 11 uses Bars 13, 14, and 15 in the first plane and bars 10 and 12 in the second plane as veto bars. The larger, black peak shows the TDCs before the veto cuts are made and the smaller purple peaks show the TDC after the veto cut is made. The larger peak is protons and neutrons, where the smaller purple peak is only neutrons.

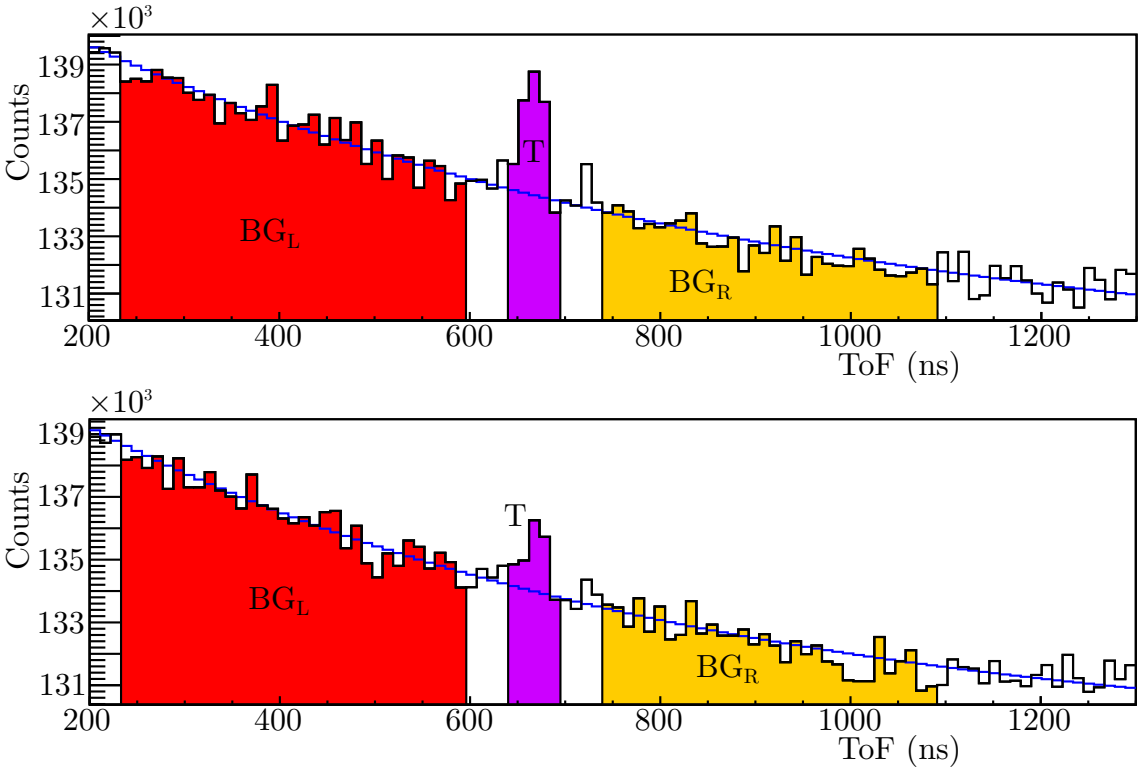

Fig. 4.11: ToF for Q^2=0.1. The upper plot is the ToF for target spin up events and the lower plot is the ToF for target spin down events. BG_L, BG_R, and T are used in the uncertainty analysis as described in Section 5.4. Events highlighted in purple above the blue fit line were considered "good" events.

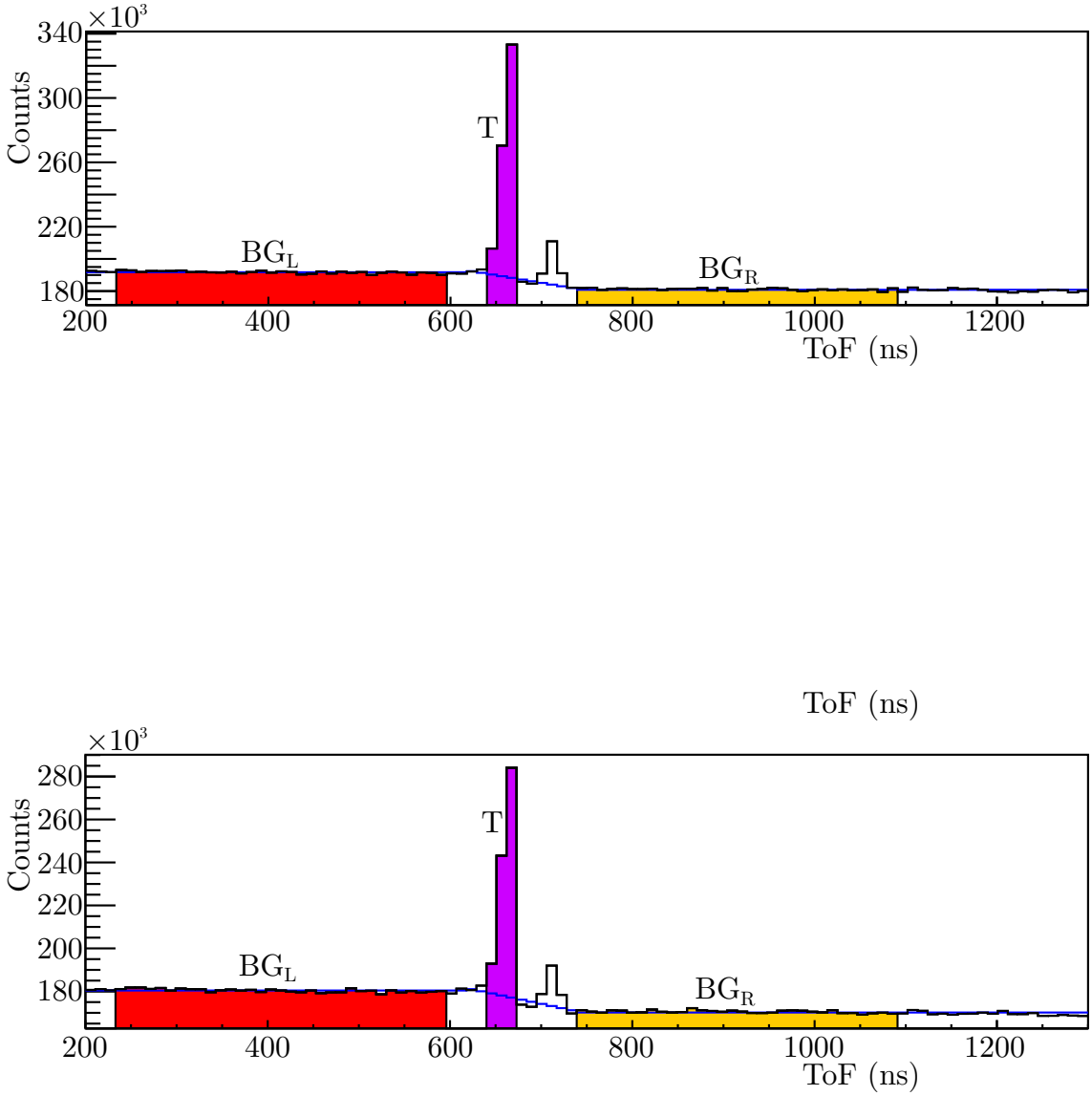

Fig. 4.12: ToF for Q^2=0.5. The upper plot is the ToF for target spin up events and the lower plot is the ToF for target spin down events. BG_L, BG_R, and T are used in the uncertainty analysis as described in Section 5.4. Events highlighted in purple above the blue fit line were considered "good" events.

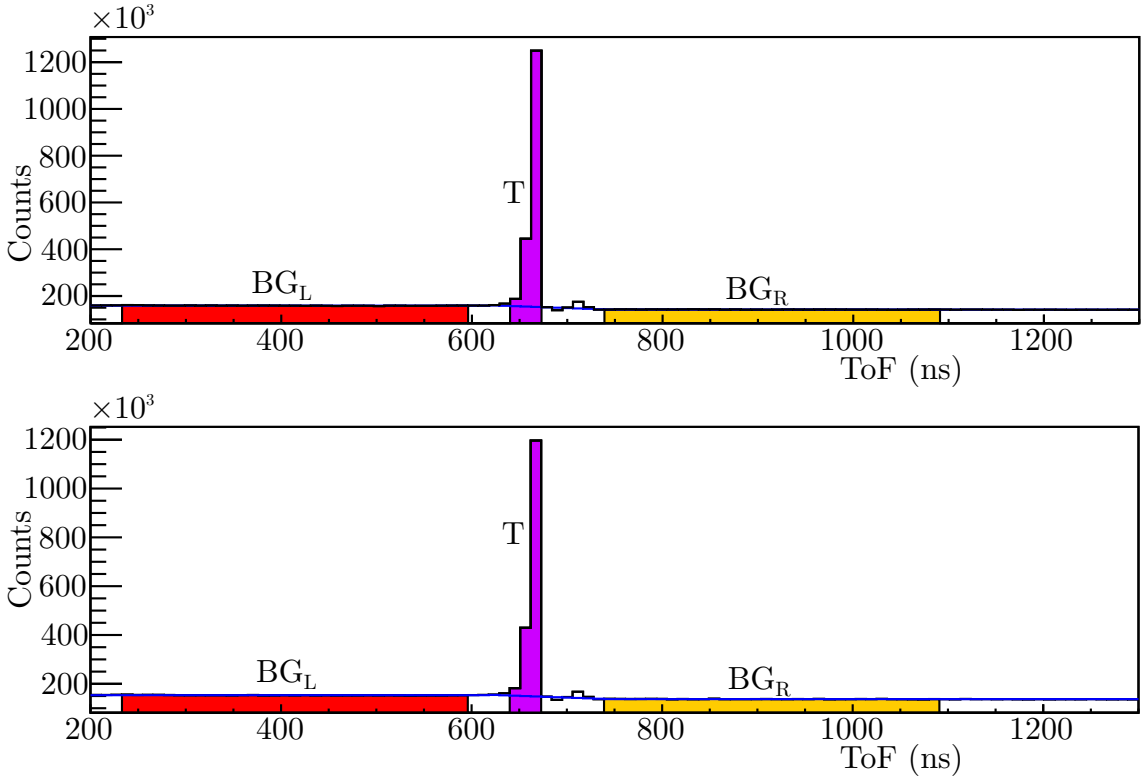

Fig. 4.13: ToF for Q^2=1.0. The upper plot is the ToF for target spin up events and the lower plot is the ToF for target spin down events. BG_L, BG_R, and T are used in the uncertainty analysis as described in Section 5.4. Events highlighted in purple above the blue fit line were considered "good" events.

Chapter 5

Dilutions and Uncertainties

5.1 Polarization of Target and Beam

5.1.1 Target Polarization

Target polarization was measured by two independent methods: nuclear magnetic resonance (NMR) at the target chamber and electron paramagnetic resonance (EPR) in the pumping chamber. For the A_y^0 experiment, there were five EPR measurements taken and NMR measurements were taken every 20 minutes after the spin was flipped. For the A_T experiment, there were 9 EPR measurements and for the A_L experiment there were 6 EPR measurements. NMR measurements were taken at intervals of approximately four hours for both A_T and A_L. Each of the EPR measurements are found in Figure 5.1. The EPR measurements allow for a measurement of a calibration constant that can be used with the NMR measurements to find the target polarization.

The description of the polarization used for a correction factor is

$$P_{tc} = \frac{d_{tc}}{d_{tc} + \Gamma_{tc}} P_p \tag{5.1}$$

where P_{tc} is the polarization in the target chamber, d_{tc} is the reduced diffusion constant, Γ_{tc} is the depolarization rate in the target chamber, and P_p is the polarization in the pumping chamber. The reduced diffusion constant for the target chamber is

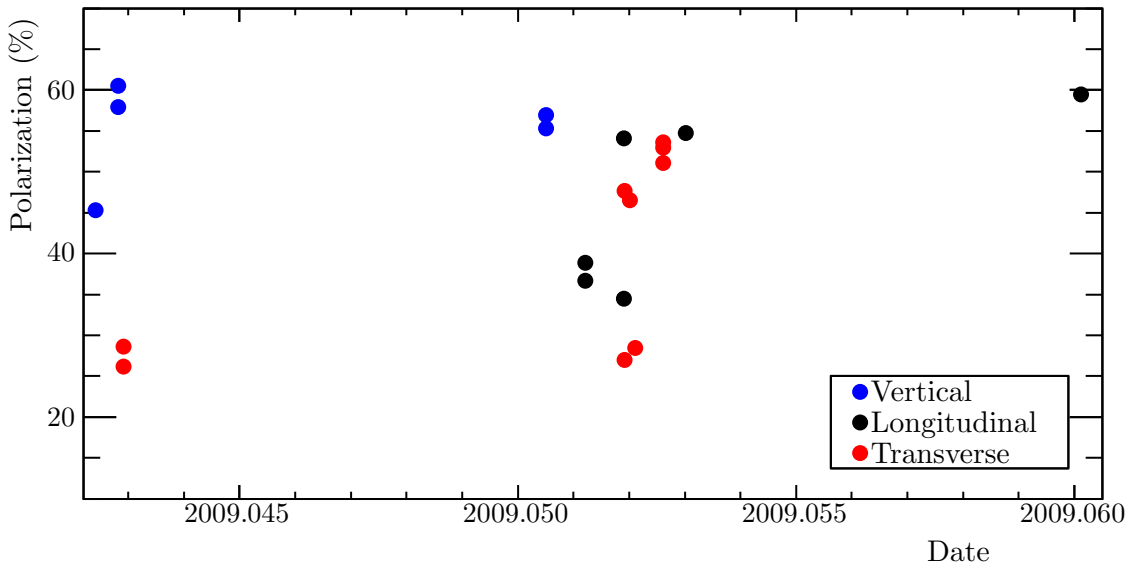

Fig. 5.1: EPR Measurements. This plot shows the EPR measurements that occurred for the A_y^0, A_T and A_L experiments.

defined as

$$d_{tc} = \frac{A_{tt} D_{tc}}{V_{tc} L_{tt}} K \tag{5.2}$$

where

$$D_{tc} = D_{T_0} \left(\frac{T_{tc}}{T_0} \right)^{(m-1)} \frac{n_0}{n_{tc}}, \tag{5.3}$$

$$K = \frac{(2-m)(t-1)}{t^{2-m}-1}, \tag{5.4}$$

$$t = T_{pc}/T_{tc}, \tag{5.5}$$

A_{tt} is the transfer tube cross section, V_{tc} is the volume of the target chamber, T is the temperature, n is the density, L_{tt} is the length of the transfer tube, and D_{tc} is the diffusion constant. The depolarization rate in the target chamber is defined as

$$\Gamma_{tc} = \Gamma^{He} + \Gamma_{tc}^{Wall} + \Gamma^{Beam} + \Gamma^{AFP} + \Gamma^{\Delta B} \tag{5.6}$$

where Γ^{He} is the nuclear dipole interaction, Γ^{Wall} is the relaxation of polarization

due to the glass walls, Γ^{Beam} is the depolarization due to the beam, Γ^{AFP} is the loss from the adiabatic fast passage, and $\Gamma^{\Delta B}$ is the relaxation of the magnetic field gradient. Taking all this into account, the beam polarization was measured and can be seen in Figures 5.2 and 5.3. This work was done by Yawei Zhang. The polarization dilution factors used in this experiment are shown in Table 5.2.

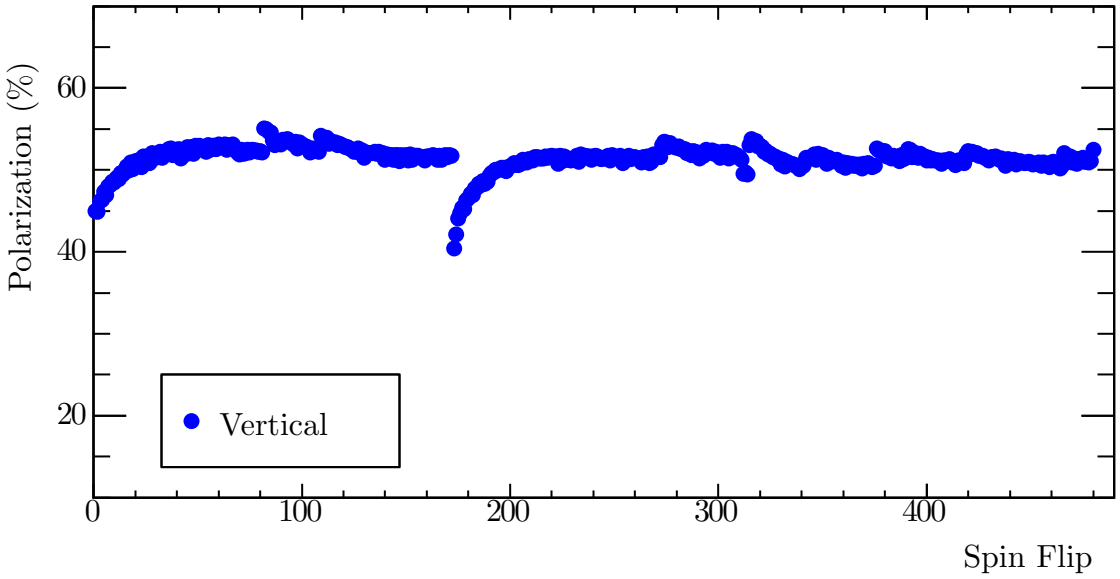

Fig. 5.2: Target Polarization Measurements for A_y^0. This plot shows the target polarization measurements that occurred for the A_y^0 experiment.

5.1.2 Beam Polarization

The beam polarization was measured with a Møller polarimeter. The Møller measurements are invasive and require beam time separate from production running. The polarimeter utilizes the fact that Møller scattering ($\vec{e^-} + \vec{e^-} \rightarrow e^- + e^-$) cross section depends on beam and target polarizations. A thin, magnetically-saturated ferromagnetic foil is used as a target. The saturation leads to an electron polarization of approximately 8% in the target. The foil can be rotated to $\pm 20^\circ$ with respect to the beam which causes the effective target polarization to be

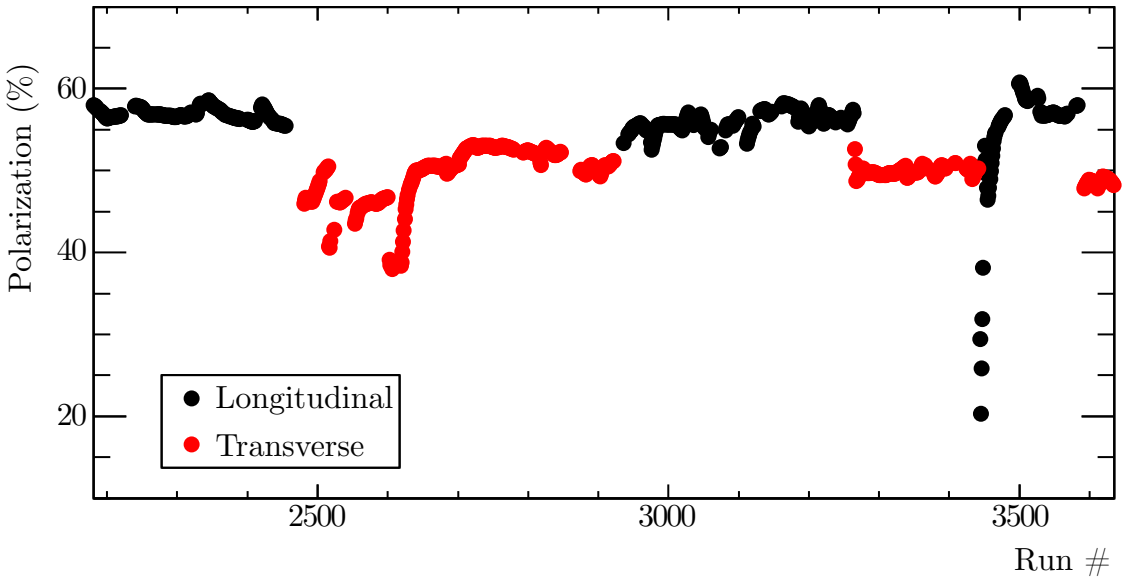

Fig. 5.3: Target Polarization Measurements for A_T and A_L. This plot shows the target polarization measurements that occurred for the A_T and A_L experiments.

Items		Rel. Pol. Error
Pumping Chamber	K-^{3}He EPR κ_0	2.8%
	Pumping Chamber Density	1.5%
	EPR Signal Fit	0.6%
	NMR Signal Fit	0.6%
Target Chamber	Diffusion Rate	1.2%
	Target Chamber Intrinsic Life-Time	1.4%
	Beam Depolarization	2.6%
	Spin Flip Loss	0.1%
Total		4.6%

Table 5.1: Target Polarization Systematic Uncertainty Budget. This table shows the uncertainties involved in obtaining the target polarization for the A_T and A_L experiments.

Experiment	Tgt. Pol. (%)	Stat. Err. (Abs. %)	Sys. Err. (Abs. %)
A_y^0	51.4	0.4	2.8
A_T	49.6	0.4	2.3
A_L	54.7	0.4	2.5

Table 5.2: Target Polarization Dilution. This table shows the values used for the dilution due to the target polarization for the A_y^0, A_T and A_L experiments.

$P_{target} = P_{foil} \cdot \cos\theta_{target}$. Since the target polarization is known, a beam-target double-spin asymmetry measurement is taken which allows the beam polarization to be determined by

$$P_Z^{beam} = \frac{N_+ - N_-}{N_+ + N_-} \cdot \frac{1}{P^{foil}} \cdot \cos\theta_{target} \cdot \langle A_{ZZ} \rangle \tag{5.7}$$

where $\langle A_{ZZ} \rangle$ is the average analyzing power. $\langle A_{ZZ} \rangle$ is dependent only on the center of mass angle scattering and was determined via a Monte Carlo calculation of the spectrometer acceptance. Five Møller measurements were taken over the course of the entire run period, which can be seen in Figure 5.4. Individually, each run has a statistical uncertainty of 0.2% and a systematic uncertainty of 2.0%. Taking the average and standard deviation, the polarization was $84.5 \pm 3.9\%$ which is used as a dilution factor for the A_T and A_L double-spin asymmetries. Since A_y^0 is a target single-spin asymmetry, the beam was treated as being unpolarized.

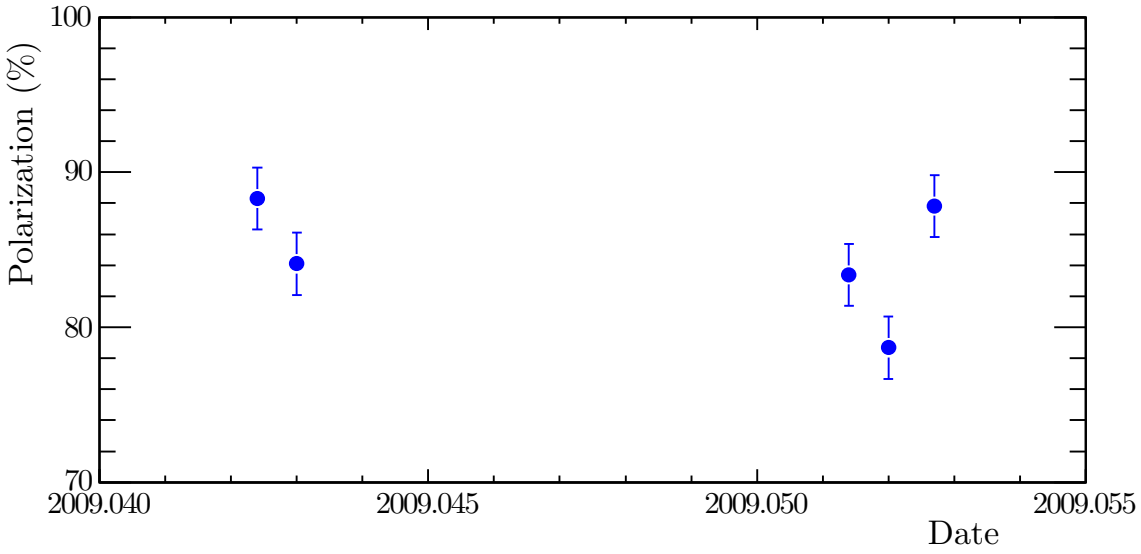

Fig. 5.4: Beam Polarization Measurements. This plot shows the Møller measurements taken to determine the beam polarization for the A_y^0, A_T and A_L experiments.

5.2 Proton Contamination

Since neutrons and protons have roughly the same mass, if an electron knocks out either one, it can be difficult to tell them apart based only on the timing information. Although veto cuts were applied to identify neutrons, as discussed in Section 4.2, protons will occasionally make it past those cuts. This can be due to a number of reasons. The largest contributor is charge-conversion, where the proton knocks out a neutron along the flight path toward HAND which is then detected by HAND. The significance of this problem increases with Q^2 as it becomes more likely that protons make it to the detector. At the highest Q^2 points, a lead wall was placed in front of the neutron detector to reduce the number of protons reaching the detector, however it also acts as a converter for protons to knockout neutrons.

5.2.1 Nucleons Along the q-vector

In order to estimate the number of protons that make it to HAND, we first need to get an estimate of the number of protons being emitted along the q-vector. For hydrogen data, this is simply the number of particles detected. For ^{3}He, however, it becomes a bit more complicated. If it is assumed that the ^{3}He nucleus is made up of two free protons and one free neutron, we can use the Rosenbluth equation to estimate the cross section.

$$\left(\frac{d\sigma}{d\Omega}\right) = \left(\frac{d\sigma}{d\Omega}\right)_{\text{Mott}} \left[\frac{G_E^2(Q^2) + \tau G_M^2(Q^2)}{1+\tau} + 2\tau G_M^2(Q^2)\tan^2\frac{\theta}{2}\right] \tag{5.8}$$

For the above equation, θ=the electron scattering angle, G_E=nucleon electric

form factor, G_M=nucleon magnetic form factor,

$$\left(\frac{d\sigma}{d\Omega}\right)_{\text{Mott}} = \left(\frac{E'}{E}\right)\left(\frac{4Z^2\alpha^2(\hbar c)^2E'^2}{|\vec{q}c|^4}\cos^2\frac{\theta}{2}\right) \text{ in the limit } \beta \to 1, \tag{5.9}$$

$$\tau = \left(\frac{Q^2}{4M^2c^2}\right), \tag{5.10}$$

$$E' = \left(\frac{E}{1+\frac{E}{Mc^2}(1-\cos\theta)}\right), \tag{5.11}$$

E=incoming electron energy, E'=outgoing electron energy, M=nucleon mass, Z=1, $|Q|^2$=$|\vec{q}|^2$=four-momentum transfer squared, β=the velocity of the electron divided by the speed of light, and α=the fine structure constant. The Kelly parametrization [25] was used to find the values of the form factors at various Q^2. Using the cross sections, the ratio of protons to neutrons at any value of Q^2 can be calculated by taking the ratio

$$r_{p:n} = \left(\frac{2\left(\frac{d\sigma}{d\Omega}\right)_p}{\left(\frac{d\sigma}{d\Omega}\right)_n}\right). \tag{5.12}$$

All of this was calculated for Q^2=0.1, 0.5, and 1.0 (GeV/c)^2 and can be found in Table 5.3.

Q^2 (GeV^2/c^2)	E (GeV)	θ (°)	$\frac{d\sigma}{d\Omega}\|_p$ (m^2)	$\frac{d\sigma}{d\Omega}\|_n$ (m^2)	$r_{p:n}$
0.1	1.245	17.0	7.19×10^{-34}	6.28×10^{-35}	22.91:1
0.5	2.425	17.0	3.03×10^{-35}	8.43×10^{-36}	7.196:1
1.0	1.245	17.0	5.26×10^{-34}	2.00×10^{-36}	5.252:1

Table 5.3: This table shows the Rosenbluth cross sections for each of the nucleons at various Q^2, electron energies (E), and scattered electron angles (θ). It also shows the estimated ratio of protons:neutrons if it is assumed that ^{3}He consists of three free nucleons.

If every scattered electron detected came from a nucleon, then we can calculate

how many of each particle was sent towards HAND along the q-vector by taking those scattered electrons that make it past the acceptance cuts (see Sections 4.1 and 4.2) and multiplying it by the ratio $r_{p:n}$ such that

$$N_e = N_p + N_n \tag{5.13}$$

$$N_p = r_{p:n} N_n \tag{5.14}$$

$$N_e = (1 + r_{p:n}) N_n \tag{5.15}$$

$$N_n = \frac{N_e}{r_{p:n} + 1} \tag{5.16}$$

where N_n=number of knocked-out neutrons, N_p=number of knocked-out protons, and N_e=number of scattered electrons. Results of this with the data taken are found in Table 5.4.

Experiment	Q^2 (GeV^2/c^2)	N_e	$r_{p:n}$	N_p	N_n
A_y^0	0.1	35,496,060	22.91 :1	3.401×10^7	1.485×10^6
	0.5	52,758,650	7.196 :1	4.632×10^7	6.437×10^6
	1.0	55,623,240	5.252 :1	4.673×10^7	8.897×10^6
A_T	0.5	51,550,460	7.196 :1	4.526×10^7	6.290×10^6
	1.0	13,416,160	5.252 :1	1.127×10^7	2.146×10^6
A_L	0.5	22,130,450	7.196 :1	1.943×10^7	2.700×10^6
	1.0	10,910,390	5.252 :1	0.9165×10^7	1.745×10^6

Table 5.4: Estimated Number of Nucleons Along q-vector. This table shows the estimated number of protons and neutrons that were scattered along the q-vector towards HAND.

5.2.2 Protons Detected by HAND

From Section 5.2.1, we know how many protons were headed towards HAND. This occurred in large part by the scattering of the knocked-out protons on the target

glass walls, the plastic around the target enclosure, the air between the target and HAND, and the lead wall during the times it was installed. However, only a fraction of these are actually detected. In order to calculate the proton dilution in ^{3}He, a calibration was done using ^{1}H. Using the hydrogen data, all of the particles detected in HAND are protons, so it can be used to find how many protons make it to HAND and how many are converted into neutrons along the way.

Three values are necessary to calculate how many protons are diluting the neutron data: the number of protons that make it past neutron cuts from the hydrogen data (P_n), the total number of protons headed along the q-vector from the hydrogen data (Tot_P), the charge accumulation of the hydrogen data (C_P), the estimated number of protons along the q-vector for ^{3}He data (N_p), and the charge accumulation of the ^{3}He data ($C_{^3He}$). For any given Q^2, the number of protons misidentified as neutrons is defined as

$$E_p = \frac{P_n}{Tot_P} \cdot N_p \cdot \frac{C_P}{C_{^3He}}. \tag{5.17}$$

From this, we can find the percentage of misidentified protons ($\%P$) by

$$\%P = \frac{E_p}{E_n} \tag{5.18}$$

where E_n is the number of ^{3}He scattered events that are identified as neutrons using the cuts described in Section 4.2. The calculated percentage of protons and neutrons is found in Table 5.5 where $\%N = 100 - \%P$. The percentage of neutrons in the ^{3}He data is used as the proton dilution factor.

Experiment	Q^2 (GeV^2/c^2)	$\%P$	$\%N$
A_y^0	0.1	7.025	92.97
	0.5	7.205	92.79
	1.0	0.9388	99.06
A_T	0.5	4.144	95.86
	1.0	2.153	97.85
A_L	0.5	9.033	90.97
	1.0	2.498	97.50

Table 5.5: Proton Contamination. This table shows the dilution factor of protons for all of the asymmetry measurements taken.

5.3 Nitrogen Contamination

The ^{3}He target becomes polarized due to spin-exchanges processes between Rb, K, and ^{3}He, as discussed in Section 3.3.2. Unfortunately, excited K atoms will also give off photons that can depolarize the ^{3}He within minutes. In order to combat this, a small amount of nitrogen was added to the target cell to absorb these photons. Contamination due to events scattered from this N_2 must be taken into account.

Dilution from N_2 was calculated using the pressure curve method. Using a reference cell filled with N_2 and comparing it to the production ^{3}He cell, a dilution can be found. The relationship between the two cells can be described as

$$Y_{N_2}^{prod} = k \cdot P_{N_2}^{prod}, \tag{5.19}$$

where $Y_{N_2}^{prod}$ is the charge and live-time normalized nitrogen yield of the ^{3}He production cell, $P_{N_2}^{prod}$ is the nitrogen pressure in the ^{3}He production cell, and

$$k = \frac{Y_{N_2}^{ref}}{P_{N_2}^{ref}}, \tag{5.20}$$

where $Y_{N_2}^{ref}$ is the charge and live-time normalized yield of a N_2-filled reference cell and $P_{N_2}^{ref}$ is the pressure in that cell. The value of k was determined by taking the slope of a linear fit of $Y_{N_2}^{ref}$ against $P_{N_2}^{ref}$ for each Q^2 value. An example of this fit is shown in Figure 5.5.

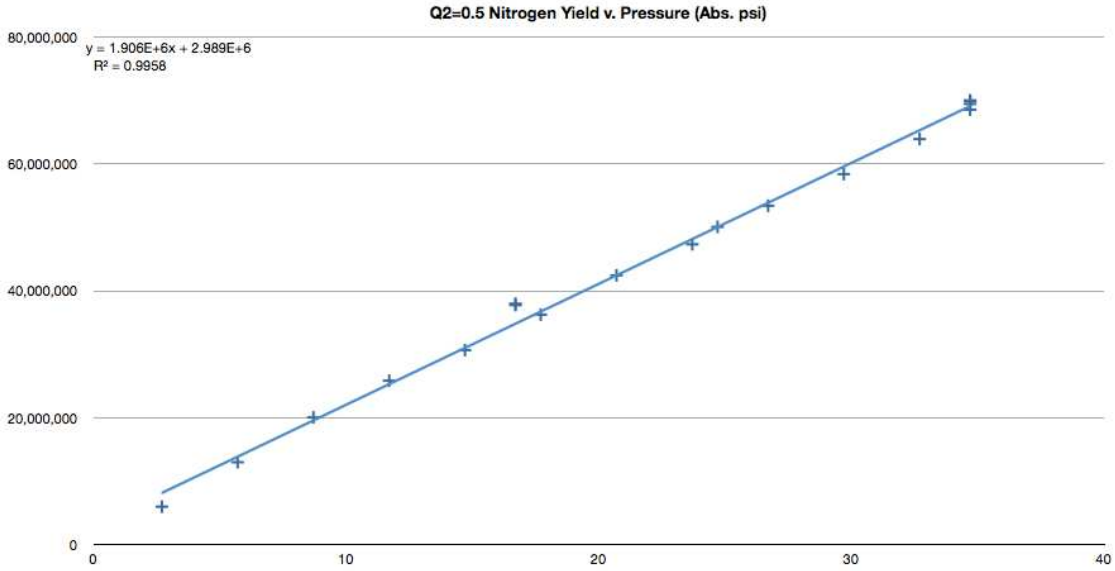

Fig. 5.5: Pressure Curve Fit Example. For each Q^2 value, a pressure curve was fit to determine k in the analysis of the nitrogen dilution factor. Presented is a pressure scan when Q^2=0.5 $(GeV/c)^2$.

The density of the ^{3}He production cells was measured in amagat, which is defined as

$$\eta = \left(\frac{p}{p_0}\right)\left(\frac{T_0}{T}\right) \text{amg}, \tag{5.21}$$

where η is the number density, p is the pressure of the cell, p_0 is 1 atm (or 14.7 psi), T is the temperature of the target cell, and T_0 is 273.15 K. The ^{3}He production cell for A_y^0 has a N_2 density of 0.0783 amg and the cell for both A_T and A_L has a N_2 density of 0.1132 amg. The ^3He production cell was held at a temperature of 46 C for A_y^0 and 45 C for A_T and A_L. This leads to $P_{N_2}^{prod} = 1.345$ psi for A_y^0, 1.938 psi for A_T and A_L. This analysis leads to the dilution values shown in Table 5.6.

Asymmetry Type	Q^2	N_2 Dilution Factor	Dilution Uncertainty
A_y^0	0.13	0.9468	0.0077
	0.46	0.9788	0.0029
	0.95	0.9721	0.0120
A_T	0.51	0.9454	0.0075
	0.95	0.9390	0.0262
A_L	0.51	0.9711	0.0040
	0.95	0.9380	0.0267

Table 5.6: N_2 Dilution Factors. This table shows the dilution factors due to nitrogen contamination that were used for each of the asymmetries at each energy.

5.4 Uncertainty Analysis

Since this dissertation examines two different types of asymmetry, target single-spin asymmetry in the case of A_y^0 and target-beam double-spin asymmetry in the case of A_L and A_T, the uncertainty analysis is handled differently for each. The single-spin asymmetry uncertainty analysis is expanded upon in Section 5.4.1 while the double-spin asymmetry's is in Section 5.4.2.

5.4.1 A_y^0 Uncertainty Analysis

The measured target single-spin asymmetry, A_y^0, is defined as

$$A_y^0 = \frac{1}{|P_y|}\left(\frac{Y_\uparrow - Y_\downarrow}{Y_\uparrow + Y_\downarrow}\right). \tag{5.22}$$

where

$$Y_{\uparrow(\downarrow)} = \frac{S_{\uparrow(\downarrow)}}{C_{\uparrow(\downarrow)} \cdot LT_{\uparrow(\downarrow)}}, \tag{5.23}$$

$$S_{\uparrow(\downarrow)} = T_{\uparrow(\downarrow)} - B_{\uparrow(\downarrow)} = \#\text{ of Signal Events}_{\uparrow(\downarrow)}, \tag{5.24}$$

$$T_{\uparrow(\downarrow)} = \text{Total }\#\text{ of Events Under Peak}_{\uparrow(\downarrow)}, \tag{5.25}$$

and

$$B_{\uparrow(\downarrow)} = \text{Background Fit}_{\uparrow(\downarrow)}. \tag{5.26}$$

If a new variable, r, is defined as

$$r = \frac{Y_{\uparrow}}{Y_{\downarrow}}, \tag{5.27}$$

then

$$A_y^0 = \frac{1}{|P_y|}\left(\frac{r-1}{r+1}\right). \tag{5.28}$$

Propagating the errors in P_y and r in quadrature, we find

$$\delta r = r\left[\left(\frac{\delta Y_{\uparrow}}{Y_{\uparrow}}\right)^2 + \left(\frac{\delta Y_{\downarrow}}{Y_{\downarrow}}\right)^2\right]^{\frac{1}{2}} \tag{5.29}$$

and

$$\delta A_y^0 = \left(\frac{A_y^2 \delta P_y^2}{P_y^2} + \frac{1}{P_y^2}\frac{4}{(r+1)^4}\delta r^2\right)^{\frac{1}{2}}. \tag{5.30}$$

If we replace r with the yields, we find

$$\delta A_y^0 = \left(\frac{A_y^2 \delta P_y^2}{P_y^2} + \frac{1}{P_y^2}\frac{4}{\left(\frac{Y_{\uparrow}}{Y_{\downarrow}}+1\right)^4}\cdot\left(\frac{Y_{\uparrow}}{Y_{\downarrow}}\right)^2\cdot\left[\left(\frac{\delta Y_{\uparrow}}{Y_{\uparrow}}\right)^2 + \left(\frac{\delta Y_{\downarrow}}{Y_{\downarrow}}\right)^2\right]\right)^{\frac{1}{2}} \tag{5.31}$$

or, more simply,

$$\delta A_y^0 = \left(\epsilon_{P_T}^2 + \epsilon_S^2\right)^{\frac{1}{2}} \tag{5.32}$$

where ϵ_{P_T} and ϵ_S are defined as in Table 5.7.

In order to use Eq. 5.31, we need to look at the error in the yields ($Y_{\uparrow(\downarrow)}$, defined in Eq. 5.23). Since the error on the charge and live-time are negligible, this leads to

$$\delta Y = \frac{\delta S}{C \cdot LT} \tag{5.33}$$

Uncertainty Type	Equation
Statistical (ϵ_S)	$\frac{1}{P_y} \cdot \frac{2}{\left(\frac{Y_\uparrow}{Y_\downarrow}+1\right)^2} \cdot \left(\frac{Y_\uparrow}{Y_\downarrow}\right) \cdot \left[\left(\frac{\delta Y_\uparrow}{Y_\uparrow}\right)^2 + \left(\frac{\delta Y_\downarrow}{Y_\downarrow}\right)^2\right]^{\frac{1}{2}}$
Target Polarization (ϵ_{P_T})	$\frac{A_y^0 \delta P_y}{P_y}$
Total (δA_y^0)	$\sqrt{\epsilon_{P_T}^2 + \epsilon_S^2}$

Table 5.7: A_y^0 Uncertainties. This table shows the equations used to calculate the uncertainties for A_y^0.

where

$$\delta S = \sqrt{\delta T^2 + \delta B^2}. \tag{5.34}$$

Since T deals with the statistical fluctuations of the signal and background,

$$\delta T = \sqrt{T}. \tag{5.35}$$

Things are more complicated with the error in the background fit. Since the time-

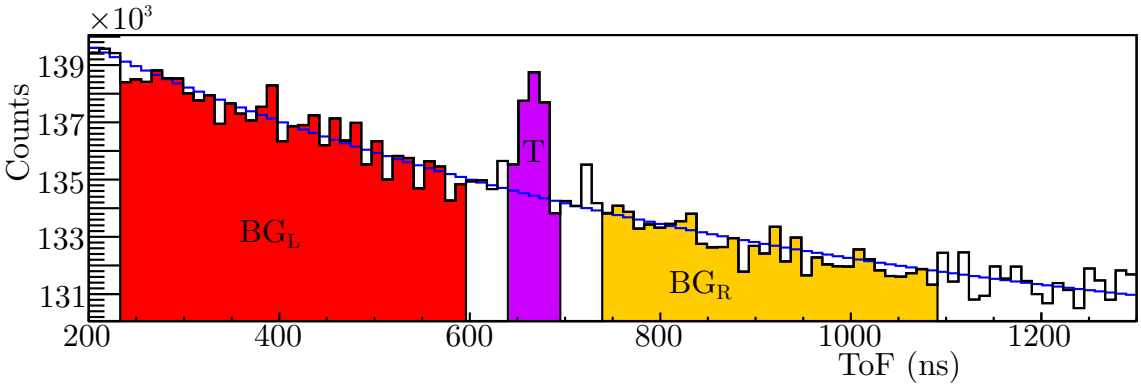

Fig. 5.6: ToF Background Example. For each ToF plot, the background was fit to the left and right of the peak. In order to estimate the error from background contributions, three sections were used. BG_L and BG_R consist of the number of events within the same number of bins on the left and right side of the peak. T consists of the total number of events under the peak which includes both the signal and background. Signal events are those events in T that are above the blue fit line.

of-flight background was measured over a large range, a fit was made for each Q^2 as defined in Section 4.2.2. A equal range of bins ($R_{BG}/2$) was integrated on the background left of the signal (BG_L) and right of the signal (BG_R). An example of this is shown in Figure 5.6 and is shown for each Q^2 for A_y^0 in Figures 4.11 through 4.13. In order to find δB, the fractional error was multiplied by the range of bins used to define the signal (R_S),

$$\delta B = \left(\frac{\sqrt{BG_L + BG_R}}{BG_L + BG_R}\right) \cdot \left(\frac{R_S}{R_{BG}}\right). \tag{5.36}$$

Taken all together, we get

$$\delta Y = \frac{1}{C \cdot LT} \cdot \sqrt{\left(\sqrt{T}\right)^2 + \left[\left(\frac{\sqrt{BG_L + BG_R}}{BG_L + BG_R}\right) \cdot \left(\frac{R_S}{R_{BG}}\right)\right]^2} \tag{5.37}$$

which can then be used in Eq. 5.31 to complete the full error analysis. The total uncertainty budget is shown in Table 5.8.

Q^2	Uncertainty Type	Amount
0.1	Statistical (ϵ_S)	0.12617
0.1	Target Polarization (ϵ_T)	0.03042
0.1	Total (δA_y^0)	0.12979
0.5	Statistical (ϵ_S)	0.00121
0.5	Target Polarization (ϵ_T)	0.01087
0.5	Total (δA_y^0)	0.01093
1.0	Statistical (ϵ_S)	0.001321
1.0	Target Polarization (ϵ_T)	0.000298
1.0	Total (δA_y^0)	0.001354

Table 5.8: A_y^0 Uncertainties. This table shows the magnitude of the uncertainties for A_y^0.

5.4.2 A_L and A_T Uncertainty Analysis

The measured target single-spin asymmetry, A_L, is defined as

$$A_{x(z)} = \frac{1}{|P_T \cdot P_B|} \left(\frac{Y_\uparrow - Y_\downarrow}{Y_\uparrow + Y_\downarrow} \right). \tag{5.38}$$

where P_T is the target polarization, P_B is the beam polarization, and Y, S, T, and B are defined as in Section 5.4.1. Following similar to logic to Section 5.4.1, we get

$$\delta A_{x(z)} = \left(\epsilon_{P_B}^2 + \epsilon_{P_T}^2 + \epsilon_S^2 \right)^{\frac{1}{2}} \tag{5.39}$$

where ϵ_{P_B}, ϵ_{P_T}, and ϵ_S are defined as in Table 5.9. The background fluctuations are included in the statistical uncertainty as in Section 5.4.1 and in particular as in Eq. 5.37. The uncertainty from polarization for A_T and A_L is shown in Table 5.10. The full uncertainties, which include terms based on the asymmetries, are shown in Sections 6.3 and 6.4.

Uncertainty Type	Equation
Statistical (ϵ_S)	$\frac{1}{P_T P_B} \cdot \frac{2}{\left(\frac{Y_\uparrow}{Y_\downarrow}+1\right)^2} \cdot \left(\frac{Y_\uparrow}{Y_\downarrow}\right) \cdot \left[\left(\frac{\delta Y_\uparrow}{Y_\uparrow}\right)^2 + \left(\frac{\delta Y_\downarrow}{Y_\downarrow}\right)^2 \right]^{\frac{1}{2}}$
Target Polarization (ϵ_{P_T})	$\frac{A \delta P_T}{P_T}$
Beam Polarization (ϵ_{P_B})	$\frac{A \delta P_B}{P_B}$
Total (δA)	$\sqrt{\epsilon_{P_B}^2 + \epsilon_{P_T}^2 + \epsilon_S^2}$

Table 5.9: A_L and A_T Uncertainties. This table shows the equations used to calculate the uncertainties for A_L and A_T.

Experiment	Uncertainty Type	Amount (Abs. %)
A_T	Target Polarization (δP_T)	2.33
	Beam Polarization (δP_B)	3.9
A_L	Target Polarization (δP_T)	2.53
	Beam Polarization (δP_B)	3.9

Table 5.10: Uncertainties in A_T and A_L. This table shows the magnitude of the uncertainties in the beam and target polarization for A_T and A_L.

Chapter 6

Results and Discussion

6.1 Asymmetry Measurements

Three different asymmetries were measured for this dissertation. Of them, there are two types: target single-spin asymmetries and beam-target double-spin asymmetries. Although both use the same mathematic form for the asymmetries,

$$A = \frac{1}{P}\frac{Y_\uparrow - Y_\downarrow}{Y_\uparrow + Y_\downarrow}, \tag{6.1}$$

the variables are subtly different. In the case of the single-spin asymmetries (A_y^0),

$$Y_{\uparrow(\downarrow)} = \frac{N_{T\uparrow(\downarrow)}}{C_{T\uparrow(\downarrow)} LT_{T\uparrow(\downarrow)}}, \tag{6.2}$$

where P = target polarization, $N_{T\uparrow(\downarrow)}$ = the number of neutrons counted with the target spin oriented up (down), $C_{T\uparrow(\downarrow)}$ = the charge accumulated with the target spin up (down), and $LT_{T\uparrow(\downarrow)}$ = the live-time with the target spin up (down).

In the case of the double-spin asymmetries (A_T and A_L),

$$Y_{\uparrow(\downarrow)} = \frac{N_{B\uparrow(\downarrow)}}{C_{B\uparrow(\downarrow)} LT_{B\uparrow(\downarrow)}}, \tag{6.3}$$

where P = target polarization times the beam polarization, $N_{B\uparrow(\downarrow)}$ = the number of neutrons counted with the beam helicity oriented up (down), $C_{B\uparrow(\downarrow)}$ = the charge accumulated with the beam helicity up (down), and $LT_{B\uparrow(\downarrow)}$ = the live-time with

the beam helicity up (down).

6.2 Vertical ^{3}He$(e, e'n)$ Asymmetries

Taking into account the error analysis and dilution factors from Chapter 5, as well as the particle identification for identifying only neutrons that were quasi-elastically from vertically polarized ^{3}He as discussed in Chapter 4, Equation 6.1 was used to find the target single-spin asymmetry. The results are presented in Tables 6.1 and 6.2. They are plotted against ν in Figures 6.1 through 6.3 and are plotted against Q^2 along with the world data and current theory estimates in Figure 6.4.

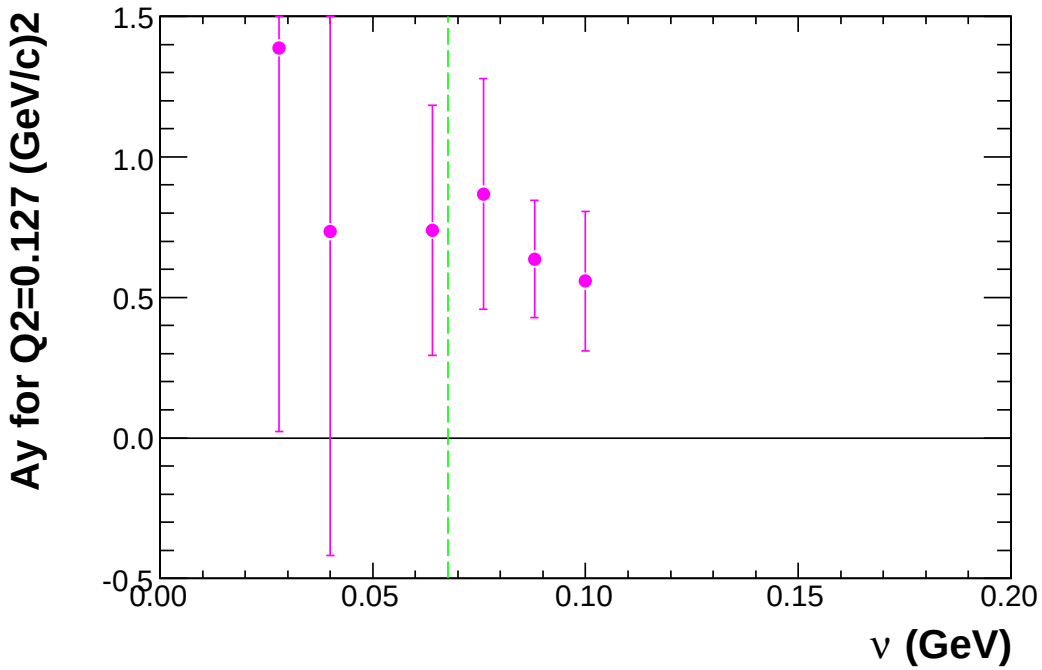

Fig. 6.1: A_y^0 Measurements for Q^2 = 0.127 (GeV/c)^2. This plot shows the current measurements for A_y^0 when Q^2 = 0.5 (GeV/c)^2. The green dashed line shows the central value of the quasi-elastic peak.

As discussed in Chapter 1, A_y^0 is useful for extracting information on the final-state interactions (FSI) and meson-exchange currents (MEC) from neutrons knocked

Q^2	ν	A_y^0	Stat. Error	Sys. Error
0.127	0.028	1.3142	1.3625	0.1449
0.127	0.040	0.6948	1.1505	0.0849
0.127	0.064	0.6992	0.4428	0.0394
0.127	0.076	0.8220	0.4079	0.0343
0.127	0.088	0.6026	0.2063	0.0260
0.127	0.100	0.5284	0.2463	0.0299
0.456	0.138	0.3228	0.0398	0.0163
0.456	0.163	0.1810	0.0111	0.0091
0.456	0.188	0.2021	0.0061	0.0102
0.456	0.213	0.2504	0.0038	0.0127
0.456	0.238	0.2114	0.0027	0.0107
0.456	0.263	0.2074	0.0024	0.0105
0.456	0.288	0.1869	0.0024	0.0094
0.456	0.313	0.1853	0.0027	0.0094
0.456	0.338	0.2211	0.0061	0.0112
0.953	0.360	-0.0109	0.0346	0.0006
0.953	0.400	0.0069	0.0092	0.0004
0.953	0.440	0.0059	0.0049	0.0003
0.953	0.480	0.0039	0.0034	0.0002
0.953	0.520	0.0072	0.0028	0.0004
0.953	0.560	0.0005	0.0027	0.0000
0.953	0.600	0.0087	0.0029	0.0005
0.953	0.640	0.0087	0.0040	0.0005

Table 6.1: A_y^0 Measurements vs. ν. These are the values for A_y^0 that were measured in this experiment against ν.

Q^2	A_y^0	Stat. Error	Sys. Error
0.13	0.72686	0.11466	0.08731
0.46	0.20234	0.00102	0.00189
0.98	0.00518	0.000686	0.000076

Table 6.2: A_y^0 Measurements. These are the values for A_y^0 that were measured in this experiment.

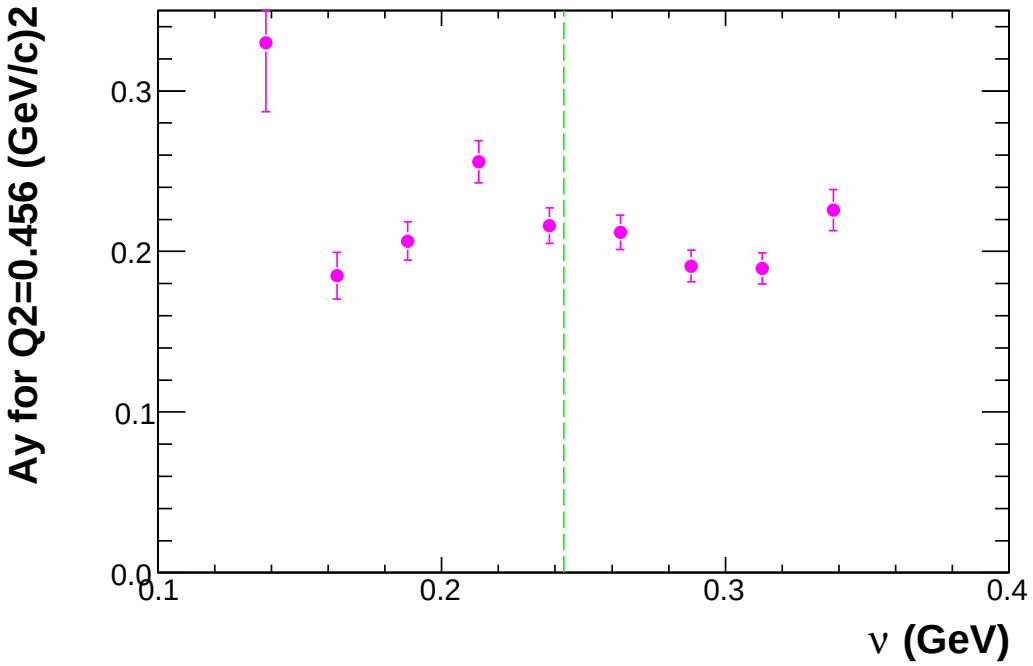

Fig. 6.2: A_y^0 Measurements for $Q^2 = 0.456$ (GeV/c)^2. This plot shows the current measurements for A_y^0 when $Q^2 = 0.456$ (GeV/c)^2. The green dashed line shows the central value of the quasi-elastic peak.

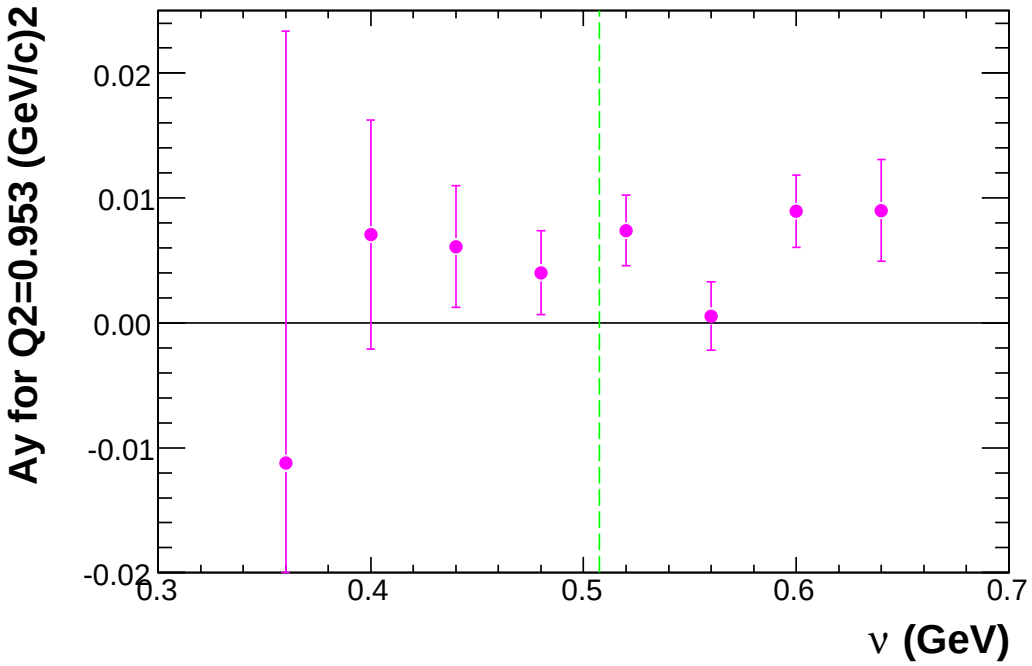

Fig. 6.3: A_y^0 Measurements for $Q^2 = 0.953$ (GeV/c)^2. This plot shows the current measurements for A_y^0 when $Q^2 = 0.953$ (GeV/c)^2. The green dashed line shows the central value of the quasi-elastic peak.

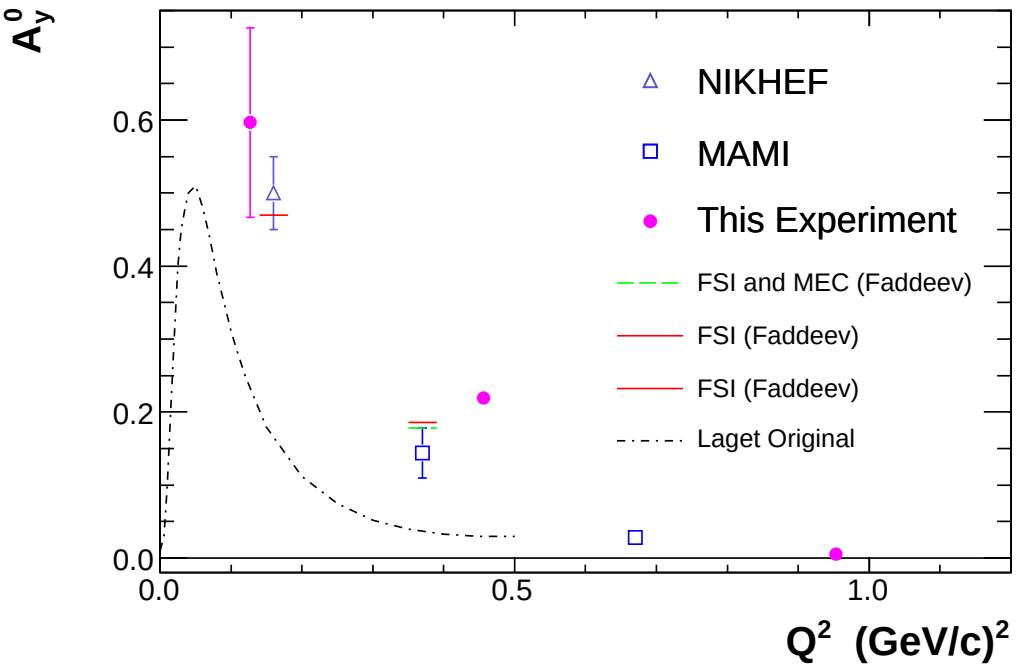

Fig. 6.4: A_y^0 World Data. This plot shows the current measurements on top of the world data for A_y^0. The points at 0.46 and 0.98 $(\mathrm{GeV}/c)^2$ have error bars smaller than the size of the data point. The error range for these points can be found in Table 6.2.

out of polarized ^{3}He. The original Laget calculation, which was done using PWIA with contributions from FSI and MEC, indicates that FSI and MEC were expected to contribute to A_y^0 largely at low Q^2 and drop off at higher Q^2. Although the magnitude of these contributions was vastly underestimated, the qualitative understanding agrees with the data presented. Full Faddeev calculations provided by the Bochum group came much closer to predicting A_y^0 values to both the historical and current data, although still appear to underestimate FSI contributions around Q^2 of 0.5 $(\mathrm{GeV}/c)^2$. This measurement is also unique in that it contains data at the high Q^2 value of 0.98 $(\mathrm{GeV}/c)^2$ where no measurement has gone before. A_y^0 is only around 0.5% in this region which indicates that any higher than this that FSI can be considered negligible and PWIA holds.

6.3 Transverse ^{3}He$(e, e'n)$ Asymmetries

Taking into account the error analysis and dilution factors from Chapter 5, as well as the particle identification for identifying only neutrons that were quasi-elastically from transversely polarized ^{3}He as discussed in Chapter 4, Equation 6.1 was used to find the target-beam double-spin asymmetry. The results are presented in Table 6.3 and plotted in Figures 6.5 and 6.6.

Although theoretical calculations are available from Misak and the Bochum group to compare with the experimental values measured for A_T, they have not yet been been calculated at the kinematics presented in this dissertation. However, these measurements will provide an important test on these calculations when available. It is important to note that measurements for both Q^2 values are non-zero and negative. For Q^2 of 0.5 $(\mathrm{GeV}/c)^2$, the asymmetry fluctuates around -0.15. For Q^2 of 1.0 $(\mathrm{GeV}/c)^2$, the asymmetry is much smaller but remains non-zero and fluctuates

Q^2	nu (GeV)	A_T	Stat. Error	Sys. Error
0.5	0.175	-0.2738	0.1766	0.0072
0.5	0.205	-0.0868	0.0365	0.0023
0.5	0.235	-0.1151	0.0162	0.0030
0.5	0.265	-0.1918	0.0094	0.0050
0.5	0.295	-0.1876	0.0064	0.0049
0.5	0.325	-0.1686	0.0057	0.0044
0.5	0.355	-0.1391	0.0066	0.0036
1	0.360	-0.0002	0.0318	0.0000
1	0.400	-0.0363	0.0084	0.0010
1	0.440	-0.0157	0.0044	0.0004
1	0.480	-0.0399	0.0030	0.0010
1	0.520	-0.0311	0.0025	0.0008
1	0.560	-0.0276	0.0024	0.0007
1	0.600	-0.0267	0.0026	0.0007
1	0.640	-0.0290	0.0036	0.0008

Table 6.3: A_T Measurements. These are the values for A_T that were measured in this experiment.

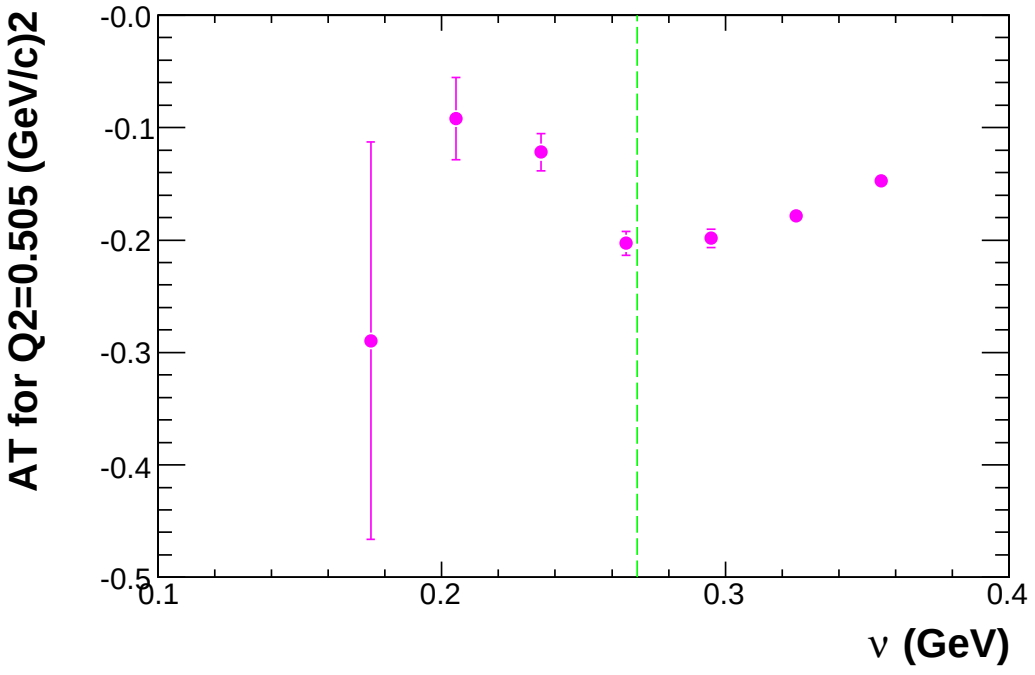

Fig. 6.5: A_T Measurements for $Q^2 = 0.5$ (GeV/c)^2. This plot shows the current measurements for A_T when $Q^2 = 0.5$ (GeV/c)^2. The green dashed line shows the central value of the quasi-elastic peak.

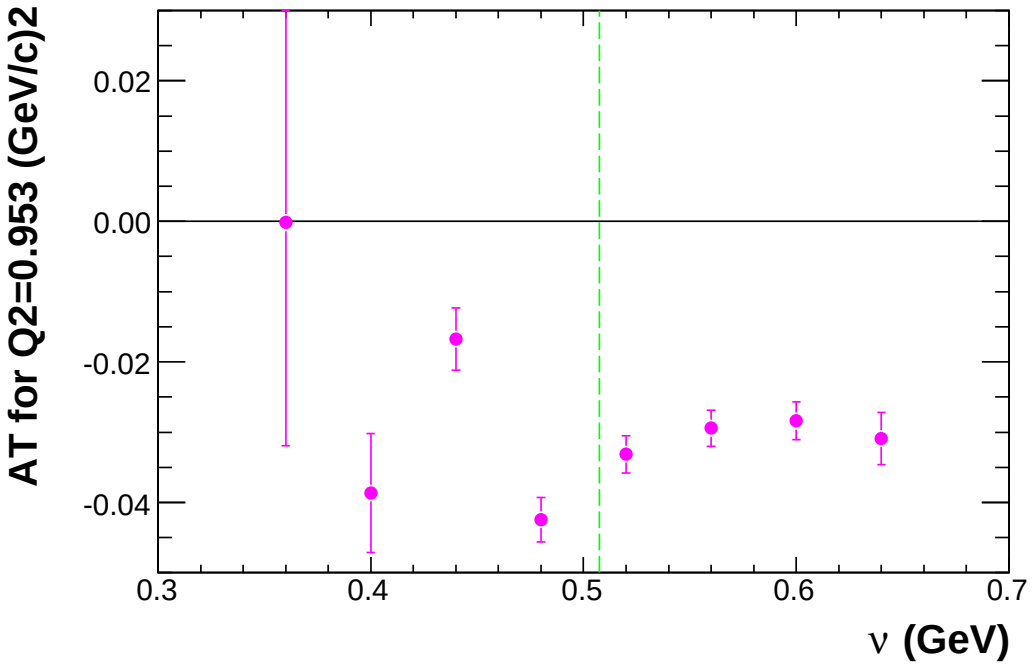

Fig. 6.6: A_T Measurements for $Q^2 = 1$ (GeV/c)^2. This plot shows the current measurements for A_T when $Q^2 = 1$ (GeV/c)^2. The green dashed line shows the central value of the quasi-elastic peak.

around -0.03.

6.4 Longitudinal ^{3}He$(e, e'n)$ Asymmetries

Taking into account the error analysis and dilution factors from Chapter 5, as well as the particle identification for identifying only neutrons that were quasi-elastically from longitudinally polarized ^{3}He as discussed in Chapter 4, Equation 6.1 was used to find the target-beam double-spin asymmetry. The results are presented in Table 6.4 and plotted in Figures 6.7 and 6.8.

Q^2	nu (GeV)	A_L	Stat. Error	Sys. Error
0.5	0.145	-0.7804	0.1003	0.0224
0.5	0.175	0.1160	0.0217	0.0033
0.5	0.205	-0.0824	0.0108	0.0024
0.5	0.235	-0.0530	0.0060	0.0015
0.5	0.265	-0.0191	0.0041	0.0005
0.5	0.295	-0.0828	0.0037	0.0024
0.5	0.325	-0.0664	0.0042	0.0019
1	0.400	-0.0105	0.0068	0.0003
1	0.440	0.0003	0.0036	0.0000
1	0.480	-0.0084	0.0024	0.0002
1	0.520	0.0059	0.0020	0.0002
1	0.560	0.0049	0.0020	0.0001
1	0.600	-0.0236	0.0021	0.0007
1	0.640	-0.0152	0.0029	0.0004
1	0.360	-0.0549	0.0254	0.0016

Table 6.4: A_L Measurements. These are the values for A_L that were measured in this experiment.

Similarly to A_T, although theoretical calculations are available from Misak and the Bochum group to compare with the experimental values measured for A_L, they have not yet been been calculated at the kinematics presented in this dissertation. However, these measurements will provide an important test on these calculations when available. It is important to note that measurements for both Q^2 values are

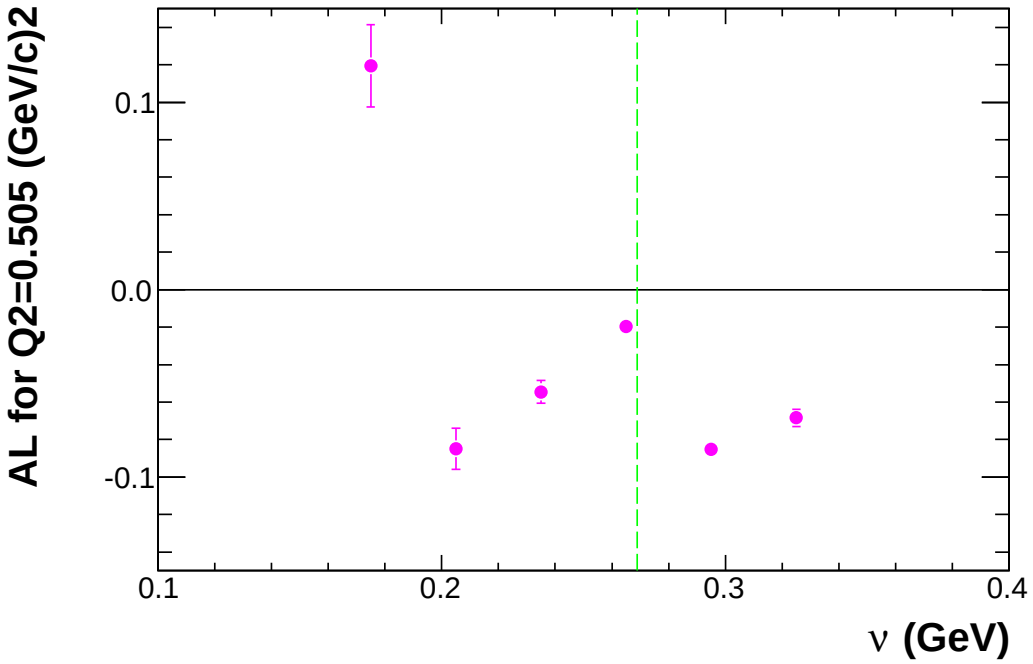

Fig. 6.7: A_L Measurements for $Q^2 = 0.5$ (GeV/c)^2. This plot shows the current measurements for A_L when $Q^2 = 0.5$ (GeV/c)^2. The green dashed line shows the central value of the quasi-elastic peak.

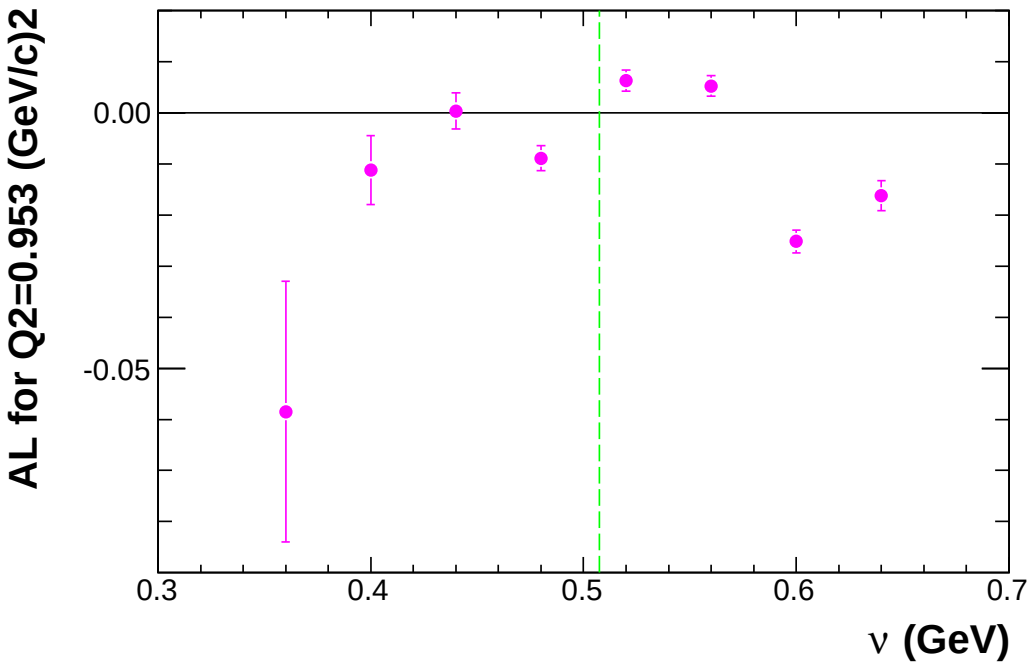

Fig. 6.8: A_L Measurements for $Q^2 = 1$ (GeV/c)^2. This plot shows the current measurements for A_L when $Q^2 = 1$ (GeV/c)^2. The green dashed line shows the central value of the quasi-elastic peak.

non-zero and change sign with ν. For Q^2 of 0.5 $(GeV/c)^2$, the asymmetry at low ν is both large and positive which indicates contributions from the elastic peak. As ν increases, the quasi-elastic region is reached where A_L becomes negative and fluctuates around -0.05. For Q^2 of 1.0 $(GeV/c)^2$, the asymmetry is much smaller but also changes sign. The quasi-elastic region is positive and fluctuates around 0.005. At higher ν the asymmetry becomes negative and fluctuates around -0.035 which is most likely due to an excited state of the neutron causing the spin to flip sign.

6.5 Summary

For this dissertation, polarized $^3He(e, e'n)$ asymmetries were measured with the beam polarized in three orthogonal directions.The target single-spin asymmetry was measured with the target polarized vertically (A_y^0) while target-beam double-spin asymmetries were measured with the target polarized transversely (A_T) and longitudinally (A_L). For A_y^0, this experiment provides the most precise measurements to date at Q^2=0.48 and extends up to 0.98 $(GeV/c)^2$. This experiment also provides the first measurements of A_T and A_L performed in this reaction and this is also the first time that all three measurements have been done in the same experiment. The A_y^0 measurements are in general agreement with earlier measurements from NIKHEF and MAMI. Comparisons with early theory calculations show qualitative agreement, however all theoretical calculations currently underestimate the measurement as one goes to higher Q^2. The non-zero results indicate FSI and MEC contributions that are under-predicted by current theoretical calculations.

Although theoretical calculations are available for both the A_T and A_L measurements presented here, they have not yet been done at the kinematics presented. However, these new measurements will provide important tests of those theory cal-

culations once they are performed.

In summary, these results help us to better understand the ^{3}He$(e, e'n)$ reaction, especially regarding the importance of FSI and MEC. This understanding is important for using the reaction to measure G_E^n and for understanding the wave function of ^{3}He better in general.

Bibliography

[1] C. Herberg *et al.*, Eur.Phys.J. **A5**, 131 (1999).

[2] M. Ostrick *et al.*, Phys.Rev.Lett. **83**, 276 (1999).

[3] M. Meyerhoff *et al.*, Phys.Lett. **B327**, 201 (1994).

[4] J. Becker *et al.*, Eur.Phys.J. **A6**, 329 (1999).

[5] D. Rohe *et al.*, Phys.Rev.Lett. **83**, 4257 (1999).

[6] J. Golak *et al.*, Phys.Rev. **C63**, 034006 (2001).

[7] J. Laget, Phys.Lett. **B273**, 367 (1991).

[8] H. R. Poolman, Ph.D. thesis, Vrije Universiteit, 1999.

[9] J. Bermuth *et al.*, Phys.Lett. **B564**, 199 (2003).

[10] I. Sick, (1992).

[11] T. Donnelly and A. Raskin, Annals Phys. **169**, 247 (1986).

[12] A. Raskin and T. Donnelly, Annals Phys. **191**, 78 (1989).

[13] J. Caballero, T. Donnelly, and G. Poulis, Nucl.Phys. **A555**, 709 (1993).

[14] H. Naus and J. Koch, Phys.Rev. **C39**, 1907 (1989).

[15] H. Naus, S. Pollock, J. Koch, and U. Oelfke, Nucl.Phys. **A509**, 717 (1990).

[16] T. De Forest, Nucl.Phys. **A392**, 232 (1983).

[17] S. Frullani and J. Mougey, Adv.Nucl.Phys. **14**, 1 (1984).

[18] R.-W. Schulze and P. Sauer, Phys.Rev. **C48**, 38 (1993).

[19] M. Mihovilocic, Ph.D. thesis, Jozef Stefan Institute, 2012.

[20] G. Jin, Ph.D. thesis, University of Virginia, 2011.

[21] Y.-W. Zhang, Ph.D. thesis, Rutger's University, (in progress).

[22] J. Alcorn *et al.*, Nucl.Instrum.Meth. **A522**, 294 (2004).

[23] W. Barry *et al.*, Technical Report No. CEBAF-PR-90-009, JLab (unpublished).

[24] *Hall A General Operations Manual*, 2011.

[25] J. Kelly, Phys.Rev. **C70**, 068202 (2004).

Appendix A

Quasi-Elastic Family (E05-102, E05-015, E08-005) Collaboration List

The Quasi-Elastic Family of Experiments (E05-102, E05-015, E08-005) collaborators (in alphabatical order) along with their respective home institutions are listed below (83 people from 31 different institutions).

K. Allada[1], B. Anderson[2], J. R. M. Annand[3], T. Averett[4], W. Boeglin[5], P. Bradshaw[4], A. Camsonne[1], M. Canan[6], G. Cates[9], C. Chen[7], J. P. Chen[1], E. Chudakov[1], R. De Leo[8], X. Deng[9], A. Deur[1], C. Dutta[10], L. El Fassi[11], D. Flay[12], S. Frullani[13], F. Garibaldi[13], H. Gao[14], S. Gilad[15], R. Gilman[11], O. Glamazdin[34], S. Golge[6], J. Gomez[1], O. Hansen[1], D. Higinbotham[1], T. Holmstrom[28], J. Huang[15], H. Ibrahim[32], C. W. de Jager[1], E. Jensen[16], X. Jiang[17], G. Jin[9], M. Jones[1], H. Kang[18], J. Katich[4], H. P. Khanal[5], P. King[19], W. Korsch[10], J. LeRose[1], R. Lindgren[9], E. Long[2], H.-J. Lu[20], W. Luo[21], P. Markowitz[5], M. Meziane[4], R. Michaels[1], M. Mihovilovic[22], B. Moffit[1], P. Monaghan[7], N. Muangma[15], S. Nanda[1], B. E. Norum[9], K. Pan[15], D. Parno[23], E. Piasetzky[24], M. Posik[12], V. Punjabi[30], A. J. R. Puckett[17], X. Qian[14], Y. Qiang[1], X. Qui[21], S. Riordan[9], A. Saha[1], B. Sawatzky[1], M. Shabestari[9], A. Shahinyan[26], B. Shoenrock[25], S. Sirca[27], J. St.

John[28], R. Subedi[29], V. Sulkosky[15], W. A. Tobias[9], W. Tireman[25], G. M. Urciuoli[13], D. Wang[9], K. Wang[9], Y. Wang[33], J. Watson[1], B. Wojtsekhoski[1], Z. Ye[7], X. Zhan[15], Y.-W. Zhang[11], Y. Zhang[21], X. Zheng[9], B. Zhao[4], L. Zhu[7]

(The Jefferson Laboratory E05-102, E05-015, E08-005, and Hall A Collaborations)

[1]Thomas Jefferson National Accelerator Facility, Newport News, VA 23606, USA

[2]Kent State University, Kent, OH, 44242, USA

[3]Glasgow University, Glasgow, G12 8QQ, Scotland, United Kingdom

[4]The College of William and Mary, Williamsburg, VA, 23187, USA

[5]Florida International University, Miami, FL, 33181, USA

[6]Old Dominion University, Norfolk, VA, 23508, USA

[7]Hampton University , Hampton, VA, 23669, USA

[8]Universite di Bari, Bari, 70121 Italy

[9]University of Virginia, Charlottesville, VA, 22908, USA

[10]University of Kentucky, Lexington, KY, 40506, USA

[11]Rutgers University, New Brunswick, NJ, 08901, USA

[12]Temple University, Philadelphia, PA, 19122, USA

[13]Istituto Nazionale Di Fisica Nucleare, INFN/Sanita, Roma, Italy

[14]Duke University, Durham, NC, 27708, USA

[15]Massachusetts Institute of Technology, Cambridge, MA, 02139, USA

[16]Christopher Newport University, Newport News, VA, 23606, USA

[17]Los Alamos National Laboratory, Los Alamos, NM, 87545, USA

[18]Seoul National University, Seoul, Korea

[19]Ohio University, Athens, OH, 45701, USA

[20]Huangshan University, People's Republic of China

[21]Lanzhou University, Lanzhou, Gansu, 730000, People's Republic of China

[22]Jozef Stefan Institute, Ljubljana 1000, Slovenia

[23]Carnegie Mellon University, Pittsburgh, PA, 15213, USA

[24]Tel Aviv University, Tel Aviv 69978, Israel

[25]Northern Michigan University, Marquette, MI, 49855, USA

[26]Yerevan Physics Institute, Yerevan, Armenia

[27]University of Ljubljana, Ljubljana, 1000, Slovenia

[28]Longwood College, Farmville, VA, 23909, USA

[29]George Washington University, Washington, D.C., 20052, USA

[30]Norfolk State University, Norfolk, VA, 23504, USA

[31]Randolph Macon College, Ashland, VA, 23005, USA

[32]Cairo University, Cairo, Giza 12613, Egypt

[33]University of Illinois at Urbana-Champaign, Urbana, IL, 61801, USA

[34]Kharkov Institute of Physics and Technology, Kharkov 61108, Ukraine

Appendix B

Veto Bars used for HAND

As discussed in Section 4.2.1, particle identification of neutrons in the Hall A Neutron Detector required the use of "veto" bars in order to separate neutrons from protons. This cannot be done through timing information alone, as the time-of-flight peaks overlap. Tables B.1 through B.4 show, in detail, which bars were used as vetoes for any given "good" bar.

TDC		Veto 1		Veto 2		Veto 3		Veto 4		Veto 5		Veto 6	
Pl	Bar	Pl	Bar	Pl	Bar	Pl	Bar	Pl	Bar	Pl	Bar	Pl	Bar
1	0	0	0	0	1	1	1						
1	1	0	0	0	1	1	0	1	2				
1	2	0	1	0	2	1	1	1	3				
1	3	0	2	0	3	1	2	1	4				
1	4	0	3	0	4	1	3	1	5				
1	5	0	4	0	5	1	4	1	6				
1	6	0	5	0	6	1	5	1	7				
1	7	0	6	0	7	1	6	1	8				
1	8	0	7	0	8	0	10	1	7	1	9		
1	9	0	8	0	9	0	10	0	11	1	8	1	10
1	10	0	9	0	11	0	12	1	9	1	11		
1	11	0	9	0	12	0	13	1	10	1	12		
1	12	0	13	0	14	1	11	1	13				
1	13	0	13	0	14	0	15	1	12	1	14		
1	14	0	14	0	15	0	16	1	13	1	15		
1	15	0	15	0	16	0	17	1	14	1	16		
1	16	0	16	0	17	0	18	1	15	1	17		
1	17	0	17	0	18	0	19	1	16	1	18		
1	18	0	18	0	19	0	20	0	22	1	17	1	19
1	19	0	19	0	20	0	22	1	18	1	20		
1	20	0	20	0	21	0	22	0	23	1	19	1	21
1	21	0	21	0	23	0	24	1	20	1	22		
1	22	0	24	0	25	1	21	1	23				
1	23	0	25	0	26	1	22	1	24				
1	24	0	26	0	27	1	23	1	25				
1	25	0	27	0	28	1	24	1	26				
1	26	0	27	0	28	0	29	1	25	1	27		
1	27	0	28	0	29	0	30	1	26	1	28		
1	28	0	29	0	30	0	31	1	27	1	29		
1	29	0	30	0	31	1	28						

Table B.1: This table shows, for any given scintillator bar of HAND in the first plane, which surrounding bars were used in the veto cut. Each is labeled by Plane (Pl) and Bar number. The maximum number of vetoes for any given bar is six, however most of the bars have less than six. This is why there are blank spaces.

TDC		Veto 1		Veto 2		Veto 3		Veto 4		Veto 5		Veto 6	
Pl	Bar	Pl	Bar	Pl	Bar	Pl	Bar	Pl	Bar	Pl	Bar	Pl	Bar
2	0	1	0	1	1	2	1						
2	1	1	1	1	2	2	0	2	2				
2	2	1	2	1	3	2	1	2	3				
2	3	1	3	1	4	1	5	2	2	2	4		
2	4	1	4	1	5	1	6	2	3	2	5		
2	5	1	6	1	7	2	4	2	6				
2	6	1	7	1	8	2	5	2	7				
2	7	1	8	1	9	1	10	2	6	2	8		
2	8	1	9	1	10	1	11	2	7	2	9		
2	9	1	11	1	12	2	8	2	10				
2	10	1	12	1	13	2	9	2	11	1	11	1	14
2	11	1	13	1	14	1	15	2	10	2	12		
2	12	1	14	1	15	1	16	2	11	2	13		
2	13	1	16	1	17	2	12	2	14	2	14		
2	14	1	17	1	18	2	13	2	15	2	15		
2	15	1	18	1	19	1	20	2	14	2	16		
2	16	1	19	1	20	1	21	2	15	2	17		
2	17	1	21	1	22	2	16	2	18	2	18		
2	18	1	22	1	23	2	17	2	19				
2	19	1	23	1	24	1	25	2	18	2	20		
2	20	1	24	1	25	1	26	2	19	2	21		
2	21	1	26	1	27	2	20	2	22				
2	22	1	27	1	28	2	21	2	23				
2	23	1	28	1	29	2	22						

Table B.2: This table shows, for any given scintillator bar of HAND in the second plane, which surrounding bars were used in the veto cut. Each is labeled by Plane (Pl) and Bar number. The maximum number of vetoes for any given bar is six, however most of the bars have less than six. This is why there are blank spaces.

TDC		Veto 1		Veto 2		Veto 3		Veto 4		Veto 5	
Pl	Bar	Pl	Bar	Pl	Bar	Pl	Bar	Pl	Bar	Pl	Bar
3	0	2	0	2	1	3	1				
3	1	2	1	2	2	3	0	3	2		
3	2	2	2	2	3	3	1	3	3		
3	3	2	3	2	4	3	2	3	4		
3	4	2	4	2	5	2	6	3	3	3	5
3	5	2	5	2	6	2	7	3	4	3	6
3	6	2	7	2	8	3	5	3	7		
3	7	2	8	2	9	3	6	3	8		
3	8	2	9	2	10	3	7	3	9		
3	9	2	10	2	11	3	8	3	10		
3	10	2	11	2	12	3	9	3	11		
3	11	2	11	2	12	3	10	3	12		
3	12	2	12	2	13	2	14	3	11	3	13
3	13	2	13	2	14	3	12	3	14		
3	14	2	14	2	15	3	13	3	15		
3	15	2	15	2	16	3	14	3	16		
3	16	2	16	2	17	2	18	3	15	3	17
3	17	2	17	2	18	2	19	3	16	3	18
3	18	2	19	2	20	3	17	3	19		
3	19	2	20	2	21	3	18	3	20		
3	20	2	21	2	22	3	19	3	21		
3	21	2	22	2	23	3	20				

Table B.3: This table shows, for any given scintillator bar of HAND in the third plane, which surrounding bars were used in the veto cut. Each is labeled by Plane (Pl) and Bar number. The maximum number of vetoes for any given bar is six, however most of the bars have less than six. This is why there are blank spaces.

TDC		Veto 1		Veto 2		Veto 3		Veto 4		Veto 5		Veto 6	
Pl	Bar	Pl	Bar	Pl	Bar	Pl	Bar	Pl	Bar	Pl	Bar	Pl	Bar
4	0	3	0	3	1	3	1	4	1				
4	1	3	1	3	2	3	3	4	0	4	2		
4	2	3	3	3	4	3	5	4	1	4	3		
4	3	3	4	3	5	3	6	4	2	4	4		
4	4	3	6	3	7	3	8	4	3	4	5		
4	5	3	8	3	9	3	10	3	11	4	4	4	6
4	6	3	10	3	11	3	12	3	13	4	5	4	7
4	7	3	13	3	14	3	15	4	6	4	8		
4	8	3	15	3	16	3	17	4	7	4	9		
4	9	3	16	3	17	3	18	4	8	4	10		
4	10	3	18	3	19	3	20	4	9	4	11		
4	11	3	20	3	21	3	21	4	10				

Table B.4: This table shows, for any given scintillator bar of HAND in the fourth plane, which surrounding bars were used in the veto cut. Each is labeled by Plane (Pl) and Bar number. The maximum number of vetoes for any given bar is six, however most of the bars have less than six. This is why there are blank spaces.